Insights into the mechanism of substrate/product antiport by CaiT

Dissertation

zur Erlangung des Doktorgrades

der Naturwissenschaften

vorgelegt beim Fachbereich Biochemie, Chemie und Pharmazie

der Johann Wolfgang Goethe - Universität

in Frankfurt am Main

von

Sissy Kalayil

aus Kerala/India

Frankfurt am Main, 2015

This work was carried out in the Department of Structural Biology at the Max-Planck Institute of Biophysics in Frankfurt am Main and accepted as a dissertation in the Department of Biochemistry, Chemistry and Pharmacy from the Johann Wolfgang Goethe University of Frankfurt.

Dean: Prof. Dr. Michael Karas

1. Advisor: Prof. Dr. Volker Dötsch

2. Advisor: Prof. Dr. Werner Kühlbrandt

Date of disputation: 16.12.2015

Table of contents

Abbreviations

Å	Angstrom
AdiC	Arginine/ agmatine transporter
APC	Amino acids, polyamines and organic cation transporters
ApcT	Proton coupled amino acid transporter
BCA	Bicinchonic acid
BCCT	Betaine/carnitine/choline transporter
BetP	Betaine permease
CaiT	Carnitine transporter
CHS	Cholesteryl hemisuccinate
CL	Cardiolipin
CMC	Critical micelle concentration
Cymal-5	5-Cyclohexyl-1-pentyl-*!-D*-maltoside
Da	Dalton
DDM	*n*-Dodecyl-b-*D*-maltoside
DM	*n*-decyl-b-*D*-maltoside
dNTP	Deoxyribonucleotide triphosphate
E. coli	*Escherichia coli*
EcCaiT	*E. coli* CaiT
EMRE	Essential mcu regulator
EPL	*E. coli* polar lipid
g	Acceleration of gravity
g-BB or γ-BB	γ-butyrobetaine
HEPES	2-(4-(2-hydroxyethyl)-1-piperazinyl)-ethansulfonacid
IEX	Ion exchange chromatography
IMAC	Immobilozed metal ion chromatography
IPTG	Isopropyl-b-*D*-thiogalactopyranoside
kDa	Kilo dalton
LB	Luria Bertani
LeuT	Alanine transporter
lpr	Lipid protein ratio
MCU	Mitochondrial calcium regulator
MhP1	Benzyl hydantoin transporter
MICU1	Mitochondrial calcium uptake 1
MICU2	Mitochondrial calcium uptake 1
MFS	Major facilitator superfamily
NCS	Non-crystallographic symmetry
NSS	Neurotransmitter sodium symporter
PAGE	Polyacrylamide gel electrophoresis
PCR	Polymerase chain reaction

PM	Plasma membrane
PDB	Protein database
PmCaiT	Proteus mirabilis CaiT
SEC	Size exclusion chromatography
SLS	Swiss Light Source
SSS	Sodium solute symporters
TCEP	Tris (2-carboxyethyl)phosphine
TM	Transmembrane
TSS	Transformation and storage solution
WT	Wild type
w/v	Weight/ volume
PCR	Polymerase chain reaction

Amino acid	One letter code	Three letter code
alanine	A	Ala
cysteine	C	Cys
aspartic acid	D	Asp
glutamic acid	E	Glu
phenylalanine	F	Phe
glycine	G	Gly
histidine	H	His
isoleucine	I	Ile
lysine	K	Lys
leucine	L	Lru
methionin	M	Met
Asparagine	N	Asn
Proline	P	Pro
Glutamine	Q	Gln
Arginine	R	Arg
Serine	S	Ser
Threonine	T	Thr
Valine	V	Val
Tryptophan	W	Trp
Tyrosine	Y	Tyr

List of Figures

List of Tables

Abstract

During my thesis work, I mainly worked on characterizing two different membrane proteins, a bacterial secondary transporter and a human mitochondrial calcium channel. The first part of my thesis involves the structural and biochemical characterization of an L-carnitine/ γ-butyrobetaine antiporter called CaiT. CaiT or carnitine transporter belongs to the Betaine-carnitine-choline transporter (BCCT) family. Unlike other members of this family, CaiT is not involved in regulating osmotic stress in bacteria. Another unique feature of CaiT is that it is independent of an ion gradient for its function. These features make CaiT unique in the BCCT family. Crystal structures of CaiT from *Escherichia coli* and *Proteus mirabilis* (Schulze *et al*, 2010) (Tang *et al*, 2010) revealed an inverted five-transmembrane-helix repeat fold also known as the LeuT fold similar to that seen in the amino acid/Na^+ symporter LeuT. CaiT was crystallized in an inward facing conformation with the central substrate-binding site accessible to the cytoplasm.

While most transporters with a LeuT fold has a highly conserved Na2 site, where a sodium ion binds and dissociates during substrate transport, the corresponding Na2 site in CaiT is replaced by a positively charged amino acid (arginine 262). It was part of my research to understand the Na^+ independence of CaiT and to crystallize CaiT in the remaining conformations to comprehend better the mechanism of substrate/ product antiport in CaiT.

Studies using mutations of arginine 262 (R262) at the Na2 site, into glutamate or alanine showed that the mutant CaiT is Na^+-dependent. The transport activity of R262 mutants increased by almost 30–40% in the presence of a membrane potential thus indicating substrate/Na^+ cotransport. Structural and biochemical characterization revealed that R262 plays a crucial role in substrate binding by stabilizing the partly unwound TM1' helix. Modeling CaiT from *P. mirabilis* in the outward-open and closed states on the corresponding structures of the related symporter BetP reveals alternating orientations of the buried R262 side chain, which

mimic sodium binding and unbinding in the Na^+-coupled substrate symporters.

We propose that a similar mechanism is operative in other Na^+/H^+-independent transporters, in which a positively charged amino acid replaces the cotransported cation. The oscillation of the R262 side chain in CaiT indicates how a positive charge triggers the change between outward-open and inward-open conformations as a unifying critical step in LeuT-type transporters.

This model of R262 oscillation could further be confirmed by obtaining the crystal structure of CaiT in an outward-open state. Since the inward open conformation appeared to be the more energetically stable state, it was necessary to fiddle with the protein structure to shift the equilibrium more to an outward-open state. Several new crystallizing conditions, mutations and construct design were performed to achieve this. While most of the mutants, totaling 10 different structures seemingly had an inward open state just like the wildtype protein; there were subtle differences that made them unique. These differences were concentrated mostly at the central substrate-binding site involving residues from TM6' (tryptophan 323, tyrosine 327, methionine 331). Additionally the orientation of the substrate, L-carnitine or γ-butyrobetaine, in some of the substrate-bound structures was unique. It could be concluded that the central substrate-binding site is highly dynamic and the cumulative effect of various orientations of the substrate within this site could confer strict substrate specificity. Moreover W323 adopted various orientations irrespective of the presence or absence of a bound substrate at the central substrate-binding site or at the periplasmic site, contrary to what had been predicted before (Schulze *et al*, 2010). Although one of the mutant structures, Y115Q, displayed a partially outside open state, the activity of this mutant remains to be tested, to confirm the physiological occurrence of this conformation.

The second part of my thesis involves the characterization of a human mitochondrial calcium channel (MCU). This protein is believed to be the part of a much bigger complex of approximately 450 kDa called the MCU complex and constitutes the actual pore of the complex. Most of the studies on this complex have been

performed in HEK cell lines and evidence for direct interaction between the components of this complex are lacking. This study involves one of the first attempts to purify MCU in large quantities suitable for structural studies. Moreover purification of the correctly folded protein could aid in characterizing the protein *in vitro*, both biochemically and structurally. Two different isoforms of the human MCU could be successfully overexpressed in *E. coli*. Both isoforms have a mitochondrial targeting sequence (mts) at the N-terminus, a soluble domain with a coiled coil region followed by two transmembrane helices. At the C-terminus there is another soluble domain containing a coiled coil region.

Although several constructs including just the soluble domain and Δmts could be expressed, more interest was on Δmts as it could provide more wholesome information of how the uniporter functions. Due to the detection of degradation products on an SDS gel after affinity purification, the construct design was optimized using a combination of secondary structure prediction and lc-ms spec (liquid chromatography-mass spectrometry) analysis of the degraded bands. Up to 2 milligrams of the optimized Δmts construct, which now appeared stable, could be purified from one-liter culture medium. However the protein after solubilization and affinity purification in Fos-12 and/or DDM appeared mostly aggregated during size exclusion chromatography. As a result extensive crystallization trials with the protein were not successful. Since the aggregation seemed to be dependent on the concentration of the protein, the purification conditions can be optimized to obtain better soluble protein. Additionally, another membrane component of the whole complex, namely EMRE, is hypothesized to directly interact with MCU in humans. The co-expression of EMRE and MCU could thus lead to a more stable protein that could be more amenable to purification and crystallization.

Zusammenfassung

Während meiner Doktorarbeit habe ich an zwei unterschiedlichen Membranproteinen gearbeitet. Das erste Protein ist ein bakterieller Sekundärtransporter, das zweite ein mitrochondrialer Kanal aus dem Menschen.
Der erste Teil der Arbeit beinhaltet die strukturelle und biochemische Charakterisierung des L-Carnitin/ γ-Butyrobetain Antiporters CaiT. CaiT wird in die Betain-Carnitin-Cholin Transporterfamilie (BCCT) eingeordnet. Im Unterschied zu den anderen Familienmitgliedern ist CaiT nicht an der Regulation osmotischen Stresses in Bakterien involviert. Eine weitere CaiT-spezifisches Eigenschaft ist dessen ionengradienten-unabhängige Funktionsweise. Diese beiden Eigenschaften machen CaiT einzigartig innerhalb der BCCT-Familie. Die Kristallstrukturen von CaiT aus *Escherichia coli* und *Proteus mirabilis* (Schulze *et al*, 2010) (Tang *et al*, 2010) zeigten eine Proteinanordnung, bei der zwei Bündel aus fünf Transmembranhelizes die Membran relativ zueinander umgekehrte durchspannen. Diese Art der Helizesanordnung wurde als *inverted five-transmembrane-helix* Faltung oder LeuT-Faltung bezeichnet, da der Alanintransporter LeuT als erster diese Faltungsart aufwies. Die beiden gelösten CaiT-Strukturen zeigen die Proteine in einer nach innen geöffneten Konformation bei der die zentrale Substratbindungsstelle vom Zytoplama zugänglich ist.

Während die meisten der gelösten Transporter mit LeuT-Faltung eine hoch-konservierte Na2-Stelle aufweisen, durch die ein Natriumion im Verlauf des Substrattransports binden und dissoziieren kann, ist diese Stelle in CaiT durch eine positiv geladene Aminosäure, Arginin 262, ersetzt. Es war Teil meiner Forschung die Na^+-Unabhängigkeit von CaiT zu untersuchen und das Protein in einer der verbleibenden Konformationen zu kristallisieren um ein besseres Verständnis des Substrat/ Produkt Antiportmechanismus in CaiT zu erhalten.

Untersuchungen an CaiT-Proteinen, bei denen das Arginin 262 (R262) mutiert wurde, zeigen einen Na^+-abhängigen Substrattransport. Die Transportaktivität von R262 Mutanten erhöht sich um nahezu 30-40% bei anlegen eines Membranpotentials, was auf einen Substrat/Na^+ Co-Transport hindeutet. Die strukturelle und biochemische Charakterisierung ergab, dass R262 eine bedeutende Rolle in der Substratbindung einnimmt, da es den für die Bindung wichtigen entwundenen Teil der TM1' Helix stabilisiert. Modelbildungsversuche von CaiT aus *P. mirabilis* in der nach außen geöffneten und der geschlossenen Konformation ergaben alternative Orientierungen der R262 Seitenkette, die denen von Natriumbindung und -freisetzung in Na^+-abhängigen Substratsymportern nachgeahmt sein könnten. Um die CaiT Modelle mit der nach außen geöffneten bzw. geschlossenen Konformation zu erstellen wurden Strukturen des verwandten BCC transporters BetP aus *C. glutamicum* in den jeweiligen Konformationen als Grundmodel benutzt.

Nach diesen neuen Erkenntnissen vermuten wir, dass sich auch in anderen Na^+/H^+-unabhängigen Transportern ein ähnlicher Mechanismus entwickelt hat, in dem eine positiv geladene Aminosäureseitenkette das co-transporterierte Kation ersetzt. Das Oszillalieren der R262 Seitenkette während eines Transportzykluses in CaiT deutet darauf hin, wie eine positive Ladung, als vereinendes Element der LeuT-ähnlichen Transporter, die Konformationsänderungen zwischen außen-offen und innen-offen als kritischen Schritt induziert.

Das R262 Oszillationsmodel konnte in dieser Studie weitergehend durch eine CaiT Kristallstruktur in der nach außen offenen Konformation bestätigt werden. Da die nach innen offene Konformation ein energetisch begünstigter Zustand zu sein scheint, war es notwendig das Protein so zu verändern, dass eine Konformationsänderung durch Verschiebung des Energieequilibriums begünstigt wurde. Verschiedene neue Kristallisationsbedingungen, Mutationen und Konstrukte wurden benutzt um dies zu erreichen. Während die meisten der 10 verschiedenen Strukturen überwiegend die nach innen geöffnete Konformation zu haben schienen, waren doch in jeder Struktur kleine Unterschiede zu erkennen. Diese Unterschiede konzentrieren sich weitgehend auf die Substratbindungsstelle, einschließlich der

Aminosäurereste der TM6' (Tryptophan 323, Tyrosin 327, Methionin 331). Darüber hinaus zeigt auch das Substrat, L-Carnitin oder γ-Butyrobetain, in mehreren Strukturen eine unterschiedliche Bindungsweise. Daraus schließen wir, dass die zentrale Substratbindungsstelle sehr dynamisch ist und der bindungsverstärkende Effekt der verschiedenen Orientierungen des Substrats innerhalb der Bindungsstelle erklärt die hohe Substratspezifität. Weiterhin nimmt auch das W323 sowohl in An- oder Abwesenheit eines Substrates in der zentralen Bindungsstelle als auch in der periplasmatischen Bindungstelle unterschiedliche Orientierungen an, was im Widerspruch steht zu dem was zuvor postuliert wurde (Schulze *et al*, 2010). Obwohl eine der erstellten Mutanten, Y115Q, in der Struktur einen nach außen teilweise offene Zustand einnimmt, ist nicht klar, ob diese Mutante immernoch in der Lage ist, Substrat zu transportieren. Es bleibt daher zu testen, ob dieser in der Struktur festgehaltene Zustand einen physiologisch relevanten Zwischenschritt im Transportzyklus darstellt.

Der zweite Teil meiner Doktorarbeit beinnhaltet die Charakterisierung des menschlichen mitochondrialen Calciumkanal (MCU). Dieses Protein ist vermutlich Teil eines sehr viel größeren Komplexes, der insgesamt eine molekulare Masse von etwa 450 kDa umfasst und als MCU Komplex bezeichnet wird. In dem MCU Komplex ist MCU vermutlich der Teil, der die eigentliche Pore durch die Membran formt. Die meisten der bisher zu diesem Komplex durchgeführten Versuche erfolgten in HEK Zellen, jedoch konnten bisher keine direkten Interaktionen der Einzelkomponenten des Komplexes nachgewiesen werden. Die vorliegende Studie zeigt die ersten Versuche zur heterologen Expression und Reinigung von MCU in, auch für strukturelle Untersuchungen, ausreichenden Mengen. Dabei konnten zwei verschiedene Isoformen des menschlichen MCU im Expressionshost *E. coli* überexprimiert werden. Beide Isoformen enthalten am N-Terminus die mitochondriale Zielsequenz (mts, engl.: *mitochondrial targeting sequence*), eine darauffolgende lösliche *coiled coil* Domäne sowie zwei Transmembranhelizes. Der C-Terminus besteht aus einer weiteren *coiled coil* Region.

Da das MCU Gesamtprotein während der Reinigung zur Degradation neigte, wurden Konstrukte hergestellt, die auf einer Kombination von Sekundärstrukturvorhersagen und Flüssigchromatography-Massenspektrometrie (LC-MS, engl.: *liquid chromatography-mass spectrometry*) Untersuchungen von SDS-Gelbanden der degradierten Proteinfragmente basieren. Nach dieser Konstruktoptimierung konnten bis zu 2 Milligramm stabiles MCU von einem Liter Expressionskultur gereinigt werden. Jedoch zeigt sich, dass nach Solubilisierung des Proteins und Größenausschlusschromatographie ein großer Teil des Proteins aggregiert. Aufgrund dieses Aggregationsverhaltens von isoliertem MCU waren die ersten Kristallisationsansätze bisher nicht erfolgreich. Dieses Aggregationsverhalten ist vermutlich proteinkonzentrationsabhängig und ein weiter optimiertes Reinigungsprotokoll könnte dieses Problem lösen. Möglicherweise könnte auch die Interaktion eines weiteren Proteins, EMRE, das im Menschen vermutlich direkt mit MCU interagiert, das Aggregieren von MCU verhindern. Die Co-Expression von EMRE und MCU könnte daher zu einem stabilen heterodimeren Komplex führen.

Preface

This thesis describes the work that I did as a PhD student in the lab of Prof. Dr. Werner Kühlbrandt for the last 4 years. I have worked on the functional and structural characterization of two different membrane proteins, a secondary transporter named CaiT and a mitochondrial calcium channel named MCU. The thesis is divided into two chapters titled '**Structural and biochemical characterization of the substrate/product antiporter CaiT**' and '**Expression and purification of the human mitochondrial calcium uniporter**'. Each chapter comprises of a separate Introduction, Results and Discussion sections. Since the materials and methods used in both the projects are very similar, the materials and method section is included under Chapter-I. Part of the results described in the first chapter was published as a research article in PNAS journal with the title; **'Arginine oscillation explains Na^+ independence in the substrate/product antiporter CaiT**'.

Chapter I

Structural and biochemical characterization of the substrate/product antiporter CaiT

1 Introduction

Biological membranes are selectively permeable barriers that surround cells of all organisms. Made up of a phospholipid bilayer, membranes house proteins encoded by 30% of the genes in the human genome (Overington *et al*, 2006). These proteins facilitate the selective passage of solutes and ions across the membrane. Their physiological functions include metabolism, signal transduction and information processing and energy conversion and utilization (Krogh *et al*, 2001) (Engel & Gaub, 2008). Aberrant activities of membrane proteins are the primary cause of large number of human diseases such as cancer, Alzheimer's disease and metabolic diseases (Sanders & Myers, 2004) (Overington *et al*, 2006). As a result, membrane proteins are important drug targets and are the primary focus of research in pharmaceutics (Yildirim *et al*, 2007).

Membrane proteins can be broadly classified into 2 major categories depending on the mode of the protein's association with the membrane (Fig 1.1). Integral membrane proteins contain hydrophobic membrane-spanning domains that are fully inserted into the lipid bilayer. Integral membrane proteins alone or in association with other proteins (soluble or membrane-associated) are responsible for all solute transport processes across the membrane. Peripheral membrane proteins on the other hand do not interact with the hydrophobic core of the phospholipid bilayer. These are hydrophilic proteins that attach directly to the membrane or through integral membrane proteins by ionic or hydrogen bond interactions (Berk *et al*, 2003).

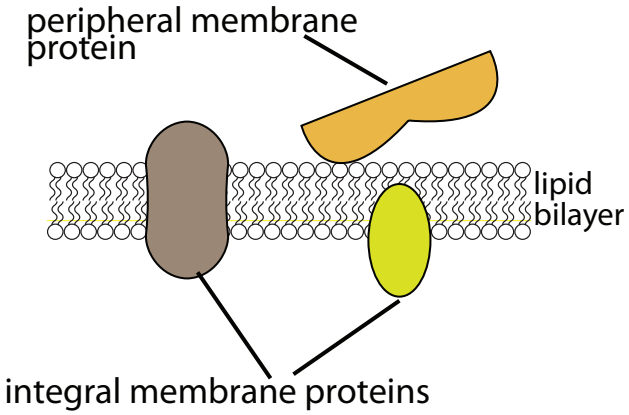

Figure 1.1 Classification of membrane proteins

Integral membrane proteins mostly span the lipid bilayer interacting with the membrane lipids directly using hydrophobic residues. Peripheral membrane proteins anchor to the membrane or interact with integral membrane proteins using ionic interactions.

Integral membrane proteins that transport solutes across the membrane can further be divided into three categories: channels, pumps and transporters. This thesis describes the structural characterization of a channel and a transporter in two different chapters. Details about the transport modes and examples are discussed in detail in the following section.

1.1 Channels, pumps and carriers

Channels permit the passage of small solutes across the membrane, often in a diffusion-limited manner, by providing a pathway through the interior of the protein. The passage of solutes is down an electrochemical gradient and hence is an energetically favorable process. This passive process mediated by channels is called facilitated diffusion. Ion channels alter from a closed conformation to an open state in response to a stimulus. This process is called gating and the gating event can be voltage or ligand-dependent. Passage of ions through channels is very rapid (10^7 ions/s) and is often diffusion-rate limited. One of the first insights into an ion channel mechanism was provided by the crystal structure of a bacterial potassium channel, KcsA (Doyle *et al*, 1998). Several main chain carbonyl groups from the potassium channel signature sequence form a selectivity filter that ensures the passage of only

dehydrated potassium ions (Fig 1.2). Such constrictions formed by highly conserved amino acid sequences are also responsible for substrate selectivity in water channels called aquaporins. In the absence of such strict selectivity, ions could pass through aquaporins, which remain mostly open, thus collapsing the membrane potential. The second part of my thesis deals with the expression, purification and biochemical characterization of a mitochondrial Ca^{2+} channel.

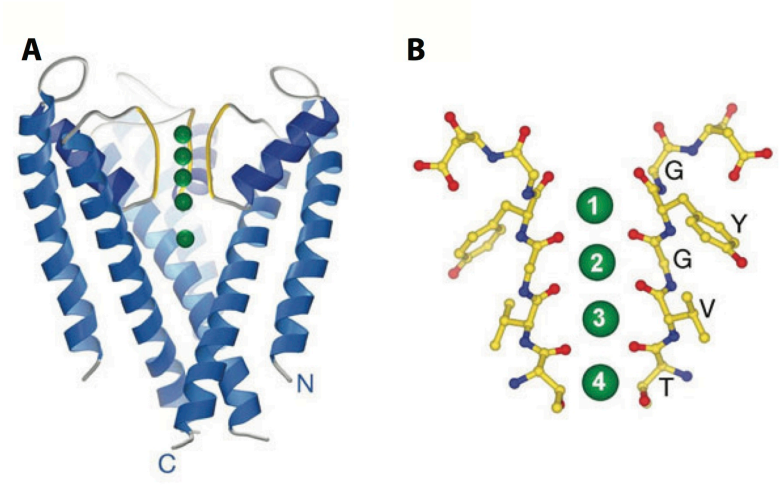

Figure 1.2 Selectivity filter of a potassium channel

A) Ribbon representation of the KcsA channel. Potassium ions (green spheres) are recognized by the selectivity filter (yellow). B) Carbonyl groups from the backbone of amino acids line the selectivity filter. Position 1 is closest to the extracellular solution and position 4 is closest to the water-filled cavity at the membrane centre (Zhou *et al*, 2001).

As opposed to channels, pumps and transporters carry out active transport that requires energy expenditure for transmembrane solute translocation. During active transport, a solute is transported against its concentration gradient (Fig 1.3). If the energy for the transport comes from a primary source such as light absorption, electron flow or ATP (adenosine triphosphate) hydrolysis, it is called primary active transport. Such transporters, better known as pumps include the Na^+/K^+ ATPase, K^+/H^+ ATPase and Ca^{2+} ATPase. On the other hand, if the energy for transport is provided by an electrochemical gradient generated by a primary active transporter, it is called secondary active transport (Saier, 2000). Examples of secondary active transporters include the sodium coupled glucose transporter (SGLT), Na^+/Ca^{2+}

exchanger, H^+/oligopeptide transporter (PepT) etc. Since pumps and carriers transport against an electrochemical gradient it is crucial that there is no leakage of ions caused by diffusion. To achieve this, these transporters undergo structural changes to alternately open and close at either side of the membrane, thus preventing a complete open pathway through the lipid bilayer. The average rate of transport is about 100 ions/s in the case of pumps (Gadsby *et al*, 2009) and 10^2-10^4 molecules/s for a carrier/secondary active transporter (Fig 1.3).

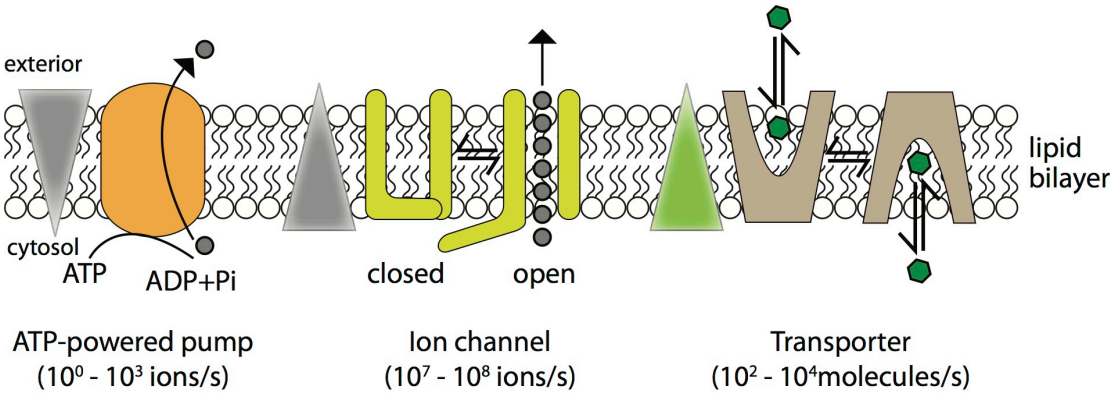

Figure 1.3 Membrane transport by channels, pumps and transporters

During active transport a solute is transported against the electrochemical gradient, powered by ATP hydrolysis. For a channel, the flow of ions is down a concentration gradient and the channel usually alternates between a closed and an open state. Once the channel opens in response to a gating event, the flow of ions occurs unhindered. For transporters there is a large conformational change that exposes the central solute-binding site to either side of the membrane. This ensures that there is no leakage of molecules since the transport occurs against the electrochemical gradient.

1.2 Secondary active transport and alternating access mechanism

There are two modes of secondary active transport, namely symport and antiport. During transport, both symporters and antiporters undergo a series of conformational changes exposing their substrate-binding site located at the center of the macromolecule, alternatively to either sides of the membrane. This mechanism is referred to as the alternating access mechanism (Jardetzky, 1966) (Fig 1.4). This ensures that the transporter is not constitutively open, which could lead to

the collapse of the electrochemical gradient present across the membrane. A third kind of transport where the transporter undergoes alternating access, but transports solute via facilitated diffusion is called uniport. The direction of transport by a uniporter is determined by the gradient of the solute as in the case of an ion channel transport. An example for a uniporter is the human glucose transporter that transports glucose into cells down the concentration gradient. When the concentration gradient of glucose is switched, the transporter operates in reverse (Fehr *et al*, 2005).

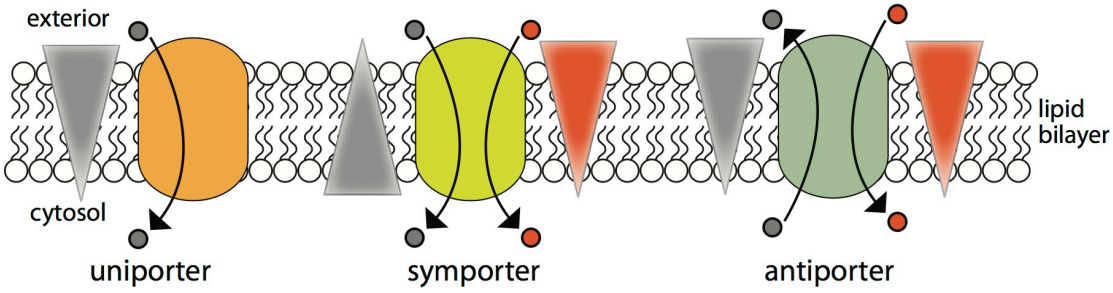

Figure 1.4 Solute transport by a uniporter, symporter and an antiporter

For a uniporter the solute transport is down the concentration gradient while symporter and antiporter involves substrate transport down and against an electrochemical gradient.

In symport, the transport of an ion/ solute down its concentration gradient facilitates the co-transport of another ion/ solute (sometimes more than one) against its concentration gradient (Fig 1.5). Effectively, symporters have two substrates and during the transport process, the transporter can switch between conformations only when both or none of the substrates are bound. This strong coupling between substrates prevents the leakage of solutes that are being transported down the gradient.

An antiporter exchanges two substrates across the membrane, also in a tightly coupled process. Similar to symporters, antiporters use the free energy of the movement of one solute down its electrochemical gradient to drive the movement of a second solute against its electrochemical gradient. The antiporter binds a substrate from one side of the membrane, undergoes a conformational change and

releases it to the other side of the membrane. This process is followed by the binding of a second substrate, another conformational change of the transporter to release the second substrate on the opposite side of the membrane. In contrast to a symporter, an antiporter changes conformation only when one of the substrates is bound (Fig 1.5).

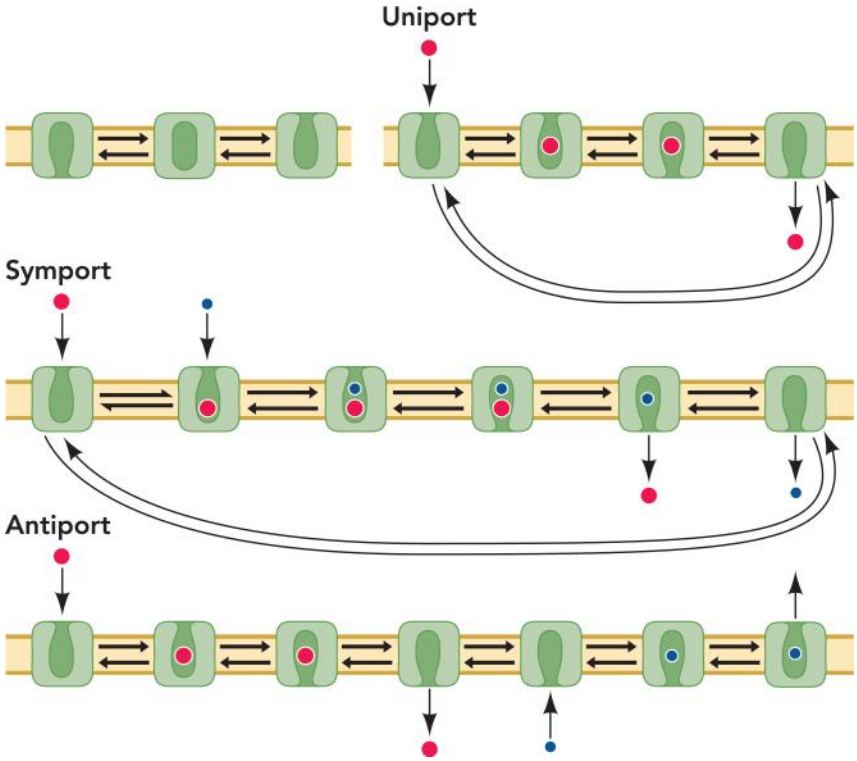

Figure 1.5 Alternating access mechanism for uniport, symport and antiport

A uniporter transports only one substrate while symport and antiport involves two or more substrates. (Forrest & Rudnick, 2009).

1.3 Structural fold of secondary active transporters

Most structurally characterized secondary active transporters fall under two major superfamilies called the MFS (Major Facilitator Superfamily) and the APC (Aminoacid-Polyamine-organoCation) superfamilies (Wong *et al*, 2012) based on their functional role, sequence similarity and structural fold. MFS, the largest known superfamily of secondary transporters consists of 84 families with over 10,000

sequenced members while the APC superfamily has 15 identified families (Wong *et al*, 2012) (Reddy *et al*, 2012) (Saier *et al*, 2014).

A common feature of all secondary active transporters is the presence of structural repeats constituted by several TM (transmembrane) helices. These structural repeats are related by a pseudosymmetry axis perpendicular to the membrane plane. A schematic below demonstrates the 'structural repeat fold' usually seen in the MFS and APC superfamilies (Fig 1.6). The MFS fold consists of a 6 TM structural repeats (also known as the 6+6 fold) while the APC superfamily has a 5 TM helix repeat fold commonly referred to as the LeuT fold (5+5 fold), after the first transporter with this fold to have its structure solved. While the structural repeats have a parallel orientation in MFS tranporters, LeuT fold shows an inverted repeat fold (Fig 1.6). The first part of my thesis involves the structural and functional characterization of a substrate/product antiporter called CaiT that exhibits a LeuT fold. CaiT is a member of the 'BCCT family', which falls under the APC superfamily.

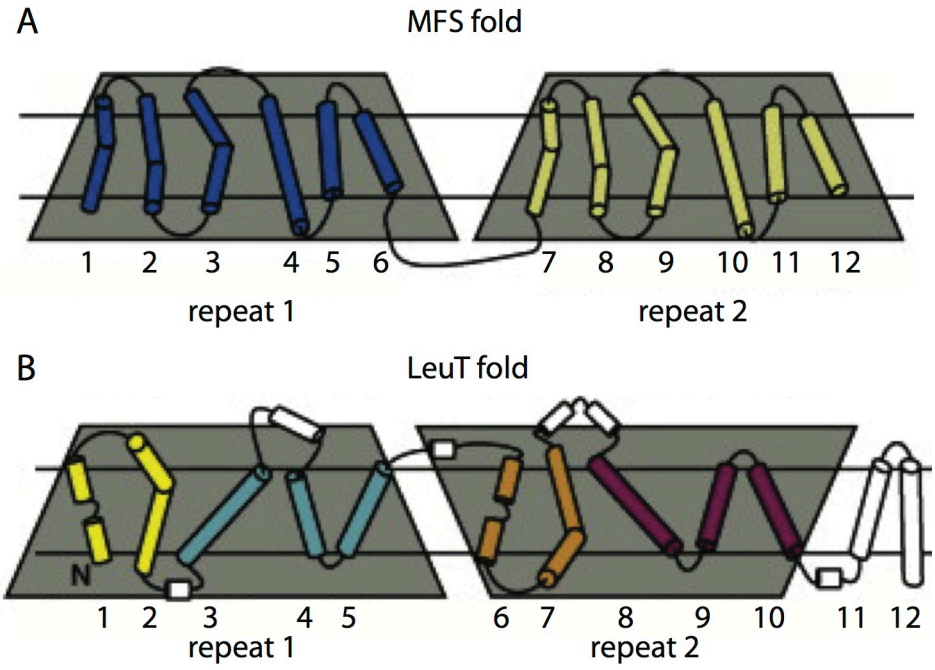

Figure 1.6 Topology diagrams of MFS and LeuT fold transporters

A) Topology diagram of the lactose transporter LacY from the MFS family. The two repeats (helices 1-6 and 7-12) that constitute the transporter are parallel to each other. The shaded trapezoids emphasize their relative orientation. B) Topology of the alanine transporter LeuT

from the NSS (neurotransmitter sodium symporter) family, a subfamily of the APC superfamily. TM helices (1-5) form repeat 1 and are inverted with respect to helices (6-10) from repeat 2. Segments that are not a part of the repeats are shown in white. Figure adapted from (Boudker & Verdon, 2010).

1.4 The BCCT (Betaine-carnitine-choline transporter) family

The biochemical characterization of members of the BCCT family reveals that almost all of them are involved in stress response in bacteria. Most of them combat osmostress by amassing osmolytes like glycine betaine (GB) or ectoine in the cell thus ensuring water retention. These osmolytes transported by BCCT carriers have a characteristic quaternary ammonium head group, with a few exceptions (*e.g*. proline betaine, acetyl choline) (Fig 1.7) (Ziegler *et al*, 2010). Additionally, almost all the BCCT family transporters that have been characterized are either sodium or proton dependent symporters (Table 1.1). Thus these transporters harness the sodium/ proton gradient existing across the membrane for the transport of a solute against its concentration gradient. The only known exception to this rule in the BCCT family is the carnitine/γ-butyrobetaine antiporter or CaiT, which is independent of a sodium or proton gradient. CaiT is a precursor/product antiporter, mainly acting during anaerobic growth conditions, unlike other members of the BCCT family that are involved in osmostress.

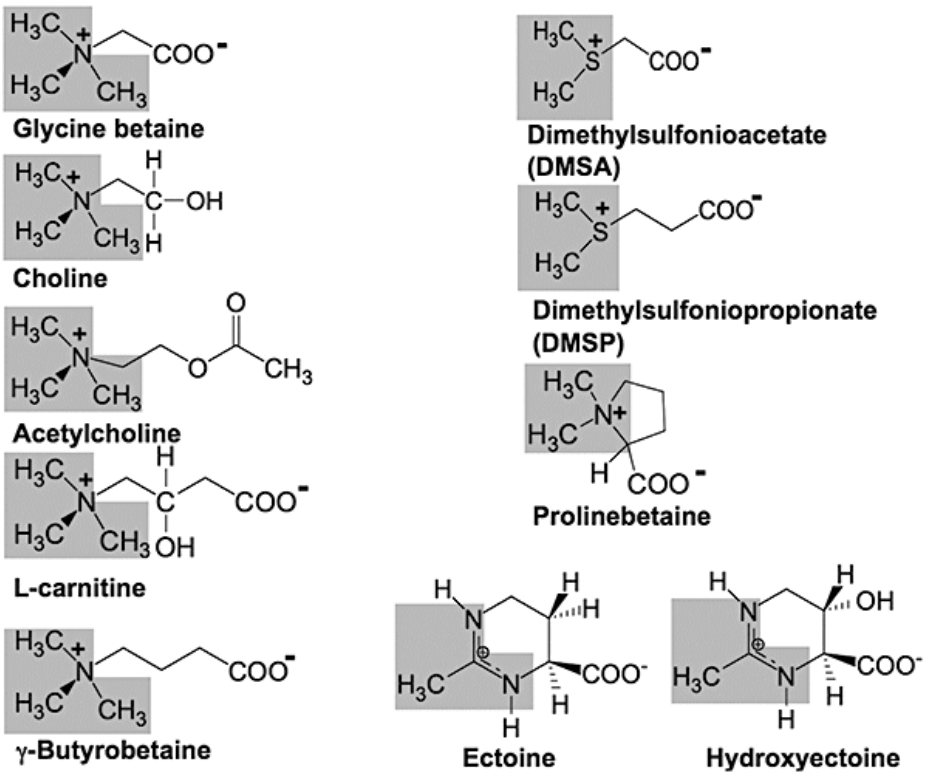

Figure 1.7 Known substrates of BCCT transporters

Positively charged head groups, either nitrogen or sulphur are shown in shaded boxes (Ziegler *et al*, 2010).

The table below summarizes the BCCT transporters that have been biochemically and /or structurally characterized. The details include their origin, their substrates and the mode of action.

Table 1.1 List of biochemically characterized BCCT transporters

The abbreviations stand for GB = glycine betaine, PB = proline betaine, E = ectoine, HE = hydroxyectoine, Ch = choline, Ach = acetylcholine, DMSP = dimethylsulphoniopropionate, C = carnitine, g-BB = γ-butyrobetaine smf = sodium motive force, pmf = proton motive force. (Adapted from (Ziegler *et al*, 2010))

Transporter	Organism	Substrate	Driving force/ direction
BetP	*Corynebacterium glutamicum*	GB	smf/symport
OpuD	*Bacillus subtilis*	GB	smf/symport
BetL	*Listeria monocytogenes*	GB	smf/symport
BetH	*Halobacillus trueperi*	GB	smf/symport
BetM	*Marinococcus halophilus*	GB	smf/symport
ButA	*Tetragenococcus halophile*	GB	smf/symport
OpuD	*Vibrio cholera*	GB	smf/symport
BetT	*Aphanothece halophytica*	GB	smf/symport
BetP	*Vibrio parahaemolyticus*	GB	smf/symport
BetU	*Escherichia coli*	GB	smf/symport
BetS	*Sinorhizobium meliloti*	GB/PB	smf/symport
DddT	*Psychrobacter* sp.	GB/DMSP	smf/symport
LcoP	*Corynebacterium glutamicum*	E/GB	smf/symport
EctT	*Virgibaccilus pantothenticus*	E/HE	smf/symport
EctM	*Marinococcus halophilus*	E/HE	smf/symport
EctP	*Corynebacterium glutamicum*	E/P/GB	smf/symport
BetT	*Pseudomonas syringae*	Ch/ACh	pmf/symport
BetT	*Escherichia coli*	Ch	pmf/symport
CudT	*Staphylococcus xylosus*	Ch	pmf/symport
* CaiT	*Escherichia coli*	C/g-BB	Substrate: product antiport
* PmCaiT	*Proteus mirabilis*	C/g-BB	Substrate: product antiport

The BCCT family was only recently included in the APC superfamily of secondary transporters (Wong *et al*, 2012). This classification was based on the recent high-resolution crystallographic data obtained on two of the BCCT family transporters namely BetP and CaiT. While BetP is a Na^+ dependent betaine symporter, CaiT is a carnitine/γ-butyrobetaine antiporter. BetP is the most extensively characterized transporter, both functionally and structurally, in the BCCT family. Crystal structures of BetP are available in eight different conformations, more than any of the secondary transporter studied so far (Perez *et al*, 2012) (Perez *et al*, 2014). Each conformation depicts a distinct state of the transport cycle. Besides the structural information, a wealth of functional studies has also been performed to support the BetP alternating access model deduced from the crystal structures. BetP thus serves

as the prototype transporter for BCCT superfamily, whose mechanistic principles of solute transport can largely be extended to other transporters in the family.

Comparison of the available structural states in BetP reveal that the structural changes, both local and global, occurring during the alternating access cycle are dictated by the binding and dissociation of two sodium ions at two conserved binding sites namely Na1 and Na2. All the structural elements involved in the transformation of BetP from an outward-open conformation (substrate binding site exposed to periplasm) to an inward-open state (substrate binding site exposed to cytoplasm) are directly or indirectly involved in the formation of the sodium binding sites in the protein (Perez *et al*, 2012). Although these conformational changes in BetP resemble those occurring in other structurally characterized transporters like LeuT, there are several differences that could be attributed to the osmolytic nature of betaine and the substrate specificity and regulatory properties in BetP.

Interestingly, despite sharing a similar fold with BetP, the transport mechanism in CaiT is independent of an electrochemical gradient across the membrane. Also CaiT is not involved in osmoregulation, as demonstrated by the absence of the long osmosensing C-terminal helix present in BetP. The structural changes occurring in CaiT therefore are not mediated by sodium ions as seen in BetP but rather by the substrates L-carnitine and γ-butyrobetaine. The Na^+ independence of CaiT makes it unique within the BCCT superfamily and makes it interesting to investigate how alternating access mechanism is dictated in CaiT.

1.5 The Carnitine/γ-butyrobetaine transporter CaiT

Many enterobacteria, when grown under anaerobic conditions and in the presence of carbon and nitrogen sources, are able to convert carnitine to γ-butyrobetaine via an intermediate crotonobetaine (Fig 1.8). This intermediate is believed to serve as an electron acceptor under such growth conditions. There are several genes involved in the carnitine metabolic pathway in *E. coli* and are encoded by the *caiTABCDE* operon

(Eichler *et al*, 1994). The operon encodes for several enzymes of the carnitine pathway including the carnitine transporter (*caiT*), crotonobetainyl-CoA reductase (*caiA*), carnitine dehydratase (*caiB*), crotonobetaine/carnitine-CoA ligase (*caiC*), carnitine racemase (*caiD*) and *caiE,* whose precise function is still unknown. The carnitine catabolism in *E. coli* was found to be not involved in osmoregulation (Jung *et al*, 1990).

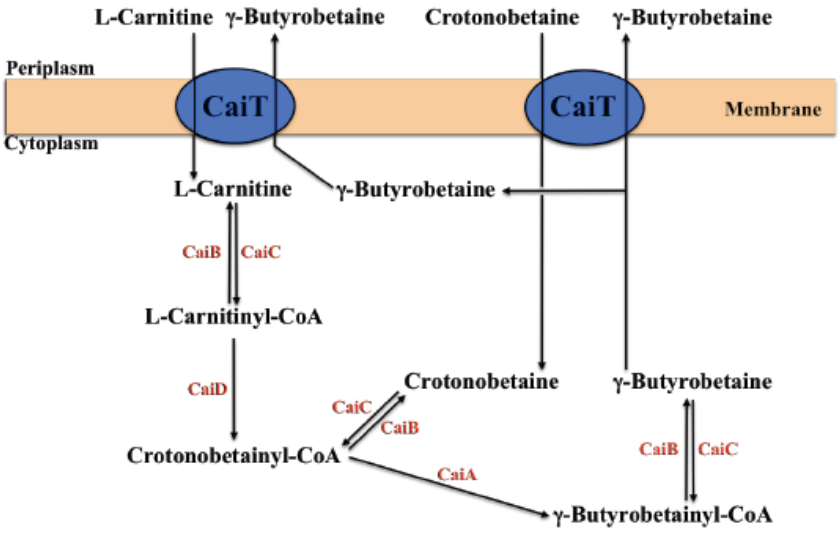

Figure 1.8 Enzymes involved in carnitine metabolism in *E. coli*

The *caitABCDE* operon encodes for all the enzymes involved in carnitine metabolism under anaerobic growth conditions (Schulze, 2011).

1.5.1 Biochemical characterization of CaiT

Based on sequence comparison and hydropathy profile analyses the *caiT* gene was predicted to encode for a membrane protein (Eichler *et al*, 1995). The *caiT* gene encodes a 504 amino acid protein that is predicted to contain 12 transmembrane (TM) helices. Uptake assays of overexpressed CaiT protein in *E. coli* and reconstituted protein in liposomes demonstrated that it could exchange L-carnitine for γ-butyrobetaine. L-carnitine counterflow analysis gave an apparent external Km of 105 µM and a turnover number of 5.5 s^{-1} (Jung, 2002). It was also observed that electrochemical ion gradients did not significantly increase the carnitine uptake.

Increasing the medium osmolality did not stimulate the exchange process in CaiT unlike in BetP that showed enhanced activity under similar conditions (Jung, 2002) (Racher *et al*, 1999) (Rübenhagen *et al*, 2000). Thus, contrary to other proteins of the BCCT family, CaiT activity is not stimulated by osmotic stress (Jung, 2002).

1.5.2 Structural characterization of CaiT

The first information on the quarternary structure of CaiT was obtained by a combination of chemical cross-linking, size exclusion chromatography and electron microscopy (EM) on purified protein from *E. coli* (Vinothkumar, 2005). In combination, the data demonstrated that CaiT forms homo-trimers in solution. Previous studies on BetP had shown that this protein also adopts a trimeric architecture (Ziegler *et al*, 2004). Size exclusion chromatography of CaiT predicted a molecular weight of around 440 kDa, which perfectly corresponds to a protein trimer (protein alone 174 kDa) surrounded by a DDM micelle (70-90 kDa per monomer). The dimensions of the CaiT trimer obtained from the projection map of 2-dimensional crystals were in good agreement with single particle cryo-EM analyses of CaiT. The dimensions of the CaiT trimer were similar to that of BetP (Ziegler *et al*, 2004).

The first atomic resolution structure of CaiT was determined by X-ray crystallography (Schulze *et al*, 2010). The structures of both *E. coli* CaiT (EcCaiT) at 3.5Å resolution and *Proteus mirabilis* CaiT (PmCaiT) at a resolution of 2.3Å were determined in substrate-bound and substrate-free states, respectively. Moreover, both structures were in an inward-open (cytoplasm facing) conformation. As expected, the three-dimensional fold adopted by CaiT was similar to that of BetP of the BCCT family (Ressl *et al*, 2009). Crystal structures of CaiT provided great insights into the substrate transport mechanism and Na^+ independence in CaiT (Schulze *et al*, 2010).

1.5.2.1 Substrate binding in CaiT

In the substrate (γ-butyrobetaine) bound EcCaiT structure, the substrate is coordinated by the so-called tryptophan box (W142 and W147 from TM2', W323 and W324 from TM6'), which is also conserved in BetP. The substrate was held in place by cation-π interactions between the quaternary ammonium group of the substrate and the indole ring of W323 from the tryptophan box. An additional substrate was also bound on the periplasmic side (an external binding site) of EcCaiT. Substrate-binding studies using EcCaiT reconstituted into proteoliposomes showed positive co-operativity indicating allosteric regulation between substrate binding at the two binding sites. Interestingly, mutating the external binding site resulted in a drastic decrease in transport activity, which led to the postulation of a regulatory role of this external binding site (Schulze *et al*, 2010).

The sidechain of the tryptophan residue at position 323 (W323) in the EcCaiT structure was rotated by ~45° compared to the same in the substrate free PmCaiT structure. The difference in orientation of W323 in both structures was attributed to the occupancy of the external substrate-binding site. While the external site in PmCaiT was blocked by crystal contacts, it was free for the substrate to bind in EcCaiT. This binding was postulated to allosterically affect the central binding site leading to the rotation of W323 and subsequent binding of substrate in the central binding site of EcCaiT (Fig 1.9).

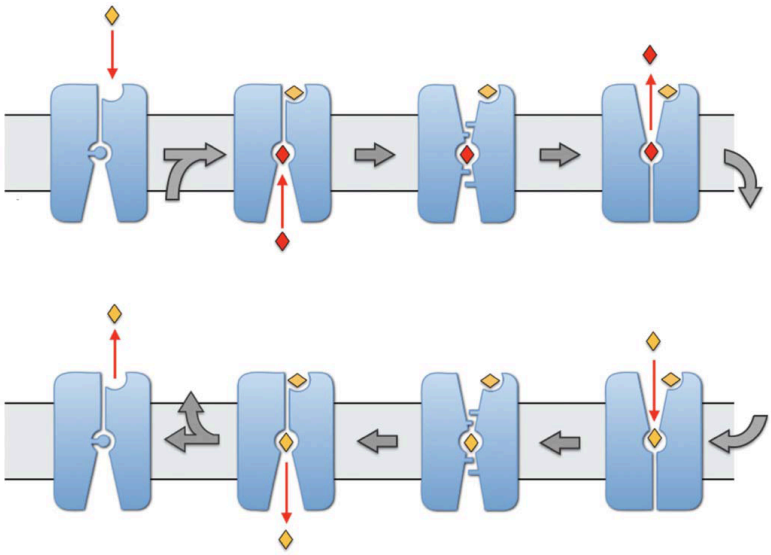

Figure 1.9 Model of cooperative substrate transport in CaiT

Binding of carnitine (yellow diamond) from the periplasmic space to the extracellular binding pocket, leads to the reorientation of W323 at the central binding site. This in turn favors the binding of the second substrate γ-butyrobetaine (red) from the cytoplasm. The transporter adopts an occluded state, blocking access of the substrate to either side of the membrane. This is followed by a conformational change, opening the transporter to the outside and releasing the substrate. The next carnitine molecule binds and the cycle continues. The extracellular binding pocket remains occupied during the entire process. Once the carnitine concentration drops, it diffuses off from the extracellular binding pocket, switching off the transport (Schulze *et al*, 2010).

1.5.2.2 Na^+ independence in CaiT

Most transporters that adopt a LeuT-type fold show a sodium-dependent substrate transport mechanism. LeuT itself (NSS family) and BetP (BCCT family) symport their specific substrates along with 2 sodium ions (Yamashita *et al*, 2005) (Farwick *et al*, 1995) (Khafizov *et al*, 2012). These sodium ions bind at two conserved binding sites, Na1 and Na2. However, other LeuT-type transporters like Mhp1 (nucleobase/cation symport 1 or NCS1 family) and vSGLT (solute/sodium symporter or SSS family) show a 1:1 substrate:sodium stoichiometry by retaining only the Na2 site (Weyand *et al*, 2008) (Shimamura *et al*, 2010) (Turk, 2000) (Faham *et al*, 2008) (Fig 1.10). These sodium ions, Na1+Na2 or Na2 alone, play a major role in facilitating the alternate

access substrate transport mechanism as explained previously with BetP as an example.

In addition to allosteric substrate binding, ion-independent substrate transport in CaiT could also be explained by its crystal structure. In CaiT, sidechains of two conserved residues occupy the positions of Na1 and Na2, thus compensating for the absence of sodium ions (Schulze *et al*, 2010). A methionine residue at position 331 (M331) in CaiT coordinates the carboxyl group of the substrate in the central binding site thus assuming the role of the Na1 seen in LeuT (Yamashita *et al*, 2005). Mutating M331 to valine reduced the substrate affinity four-fold and V_{max} by a factor of 10. However, this mutation did not render the transport Na^+ dependent (Schulze *et al*, 2010). This can be explained by the fact that the position/presence of the Na1 site is not strictly conserved among Na^+ dependent transporters like MhP1 and vSGLT.

The Na2 site in CaiT is occupied by the sidechain of an arginine residue at position 262 (R262) assuming the role of the second sodium ion (Fig 1.10). Unlike the Na1 site, the Na2 site is one of the unifying features of LeuT fold transporters (Krishnamurthy *et al*, 2009). The binding or dissociation of a sodium ion at the Na2 site is proposed to facilitate structural changes mediated by the TM1' helix during substrate transport (Zhou *et al*, 2004) (Watanabe *et al*, 2010) (Krishnamurthy & Gouaux, 2012) (Perez *et al*, 2012). In addition to CaiT, ApcT and AdiC (arginine/agmatine antiporter) are two other Na^+ independent transporters with a LeuT fold (Reig *et al*, 2007) (Shaffer *et al*, 2009) (Iyer *et al*, 2002) (Gong *et al*, 2003). Interestingly, the H^+-coupled amino acid transporter ApcT also possesses a positively charged lysine (K158) replacing the Na2 (Shaffer *et al*, 2009) (Fig 1.10). Hence it was interesting to find out if the positively charged R262 in CaiT substitutes for a sodium ion, indicating a common mechanistic principle of a Na2-driven alternating access transport in LeuT fold transporters.

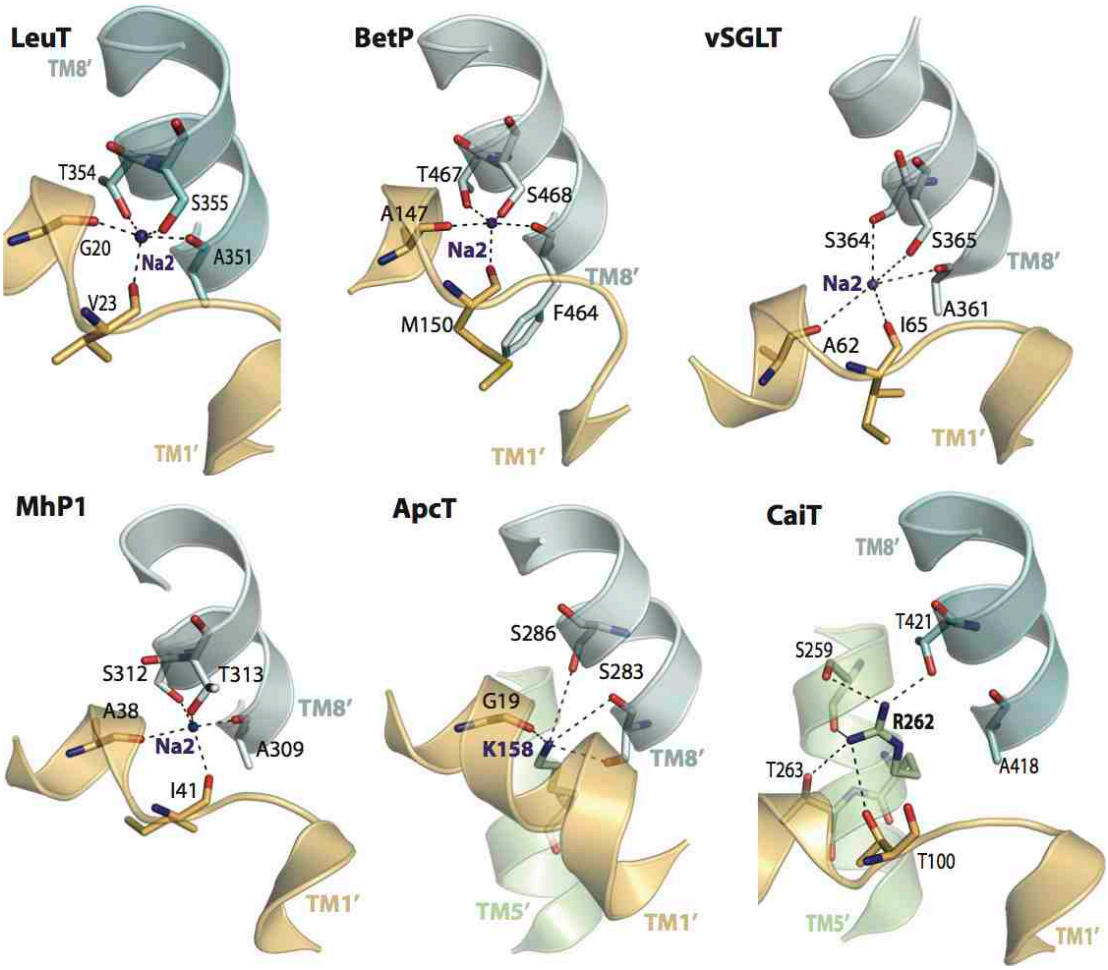

Figure 1.10 Highly conserved Na2 sites in LeuT fold transporters

Residues from two transmembrane helices, TM1‘ as well as TM8’, constitute the Na2 site. Transmembrane helices are numbered according to the LeuT system, for uniformity. In ApcT and CaiT the positive charge of the Na2 site is compensated by a lysine (K158) and an arginine residue (R262) respectively.

1.6 Alternating access mechanism in antiporters from MFS and APC superfamilies

Snapshots of secondary transporters in various states of the transport cycle have enabled us to understand the conformational changes that underlie transport mechanisms. Several transporters including LeuT, BetP (both LeuT fold) as well as Glt_{Ph} (Glt_{Ph} fold) have been crystallized in various conformations. The mechanistic details of transport varies even within LeuT fold transporters and these differences

are dictated by the presence/absence and the location of the sodium-binding sites (Perez *et al*, 2012).

Antiporters that share the same fold as symporter, occur in both MFS and APC superfamilies. So far, crystal structures of only three substrate/ product antiporters have been determined from both these superfamilies (Huang *et al*, 2003) (Gao *et al*, 2010) (Schulze *et al*, 2010). From the MFS superfamily, the crystal structure of GlpT (Glycerol-3-phosphate/inorganic phosphate antiporter) is known while from the APC superfamily the crystal structures of CaiT and AdiC are available. So far, none of these transporters were crystallized in more than one conformation. While GlpT and CaiT were crystallized in an inward-open conformation, AdiC was crystallized exclusively in an outward-open conformation. Obtaining crystal structures of distinct conformations of an antiporter can thus shed light on how the alternating access mechanism compares between antiporters and symporters.

1.7 Aim of this work

Despite sharing a similar fold, the mechanistic principles guiding the transport in antiporters are different in many respects when compared to ion/substrate symporters. While sodium ions or protons play an important role in driving transport in symporters, the substrate binds from both sides in antiporters, leading to alternating substrate release on either side of the membrane. This symmetry in substrate binding and release can be fully understood only when structures are available in both outward-facing and inward-facing states. Towards this, one aim of this work was to crystallize CaiT in an outward-open conformation. Various strategies including substrate soaking during crystallization, altering crystal contacts and introducing mutations that are expected to stabilize the outward-open conformation were adopted to push the equilibrium of CaiT to an outward-open state.

The other major aim of this project was to understand the Na^+ independence in CaiT. The close homolog BetP has been well studied both biochemically and through crystal structures of distinct conformational states. In BetP, the Na2 site was found to dictate important transitions during the substrate transport cycle. This Na2 site has been proposed to be the unifying feature of LeuT fold transporters. Hence, it was important to study how CaiT compensates for the lack of the Na2 ion and drives the transport process.

2 Materials and Methods

2.1.1 Instruments

Microfluidizer (Model M-110L, Microfluidics Corp., Newton, MA), Cary 50 UV-Vis Spectrometer (Varian), Ettan LC system (GE Healthcare), Äkta Explorer (GE Healthcare), F-4500 Fluorescence Spectrophotometer (Hitachi), Monolith NT.115 series (NanoTemper Technologies), TRI-CARB 1500 scintillation counter (Canberra-Packard), Mosquito™ pipetting robot (TTPLabtech)

2.1.2 Chemicals

Chemicals used in this work were purchased from Anatrace, Avanti, Biomol, Bio-Rad, Fermentas, Glycon, Merck, New England Biolabs, Roth, Pierce, Roche and Sigma.
γ-butyrobetaine was a kind gift from Lonza Group Ltd.

2.1.3 Column materials

Ni-NTA Agarose (Sigma Aldrich), Talon Metal affinity resin (Clontech), Chelating Sepharose™, PD-10 Sephadex G-25M, Superose™ 6 3.2/30, Superdex 200 10/300 Increase, Superdex 200 16/60 (all from GE Healthcare).

2.1.4 Reagent kits

PCR Purification Kit (Qiagen), QIAquick Gel Extraction Kit (Qiagen), QIAprep Spin Miniprep Kit (Qiagen), QuikChange® Site-Directed Mutagenesis Kit (Stratagene).

2.1.5 Antibiotics

Ampicillin 100 mg/ml, Carbenicillin 100mg/ml

2.1.6 Media

Table 2.1 Media Components

Luria Bertani (LB)	10 g/l Bacto-tryptone, 5 g/l Yeast Extract, 10 g/l NaCl
2*YT (Yeast Extract & Tryptone)	16 g/l Bacto-tryptone, 10 g/l Yeast Extract, 5 g/l NaCl
Terrific Broth (TB)	12 g/l Bacto-tryptone, 24 g/l Yeast Extract, 4 ml/l Glycerol, 100 mM/l Phosphate buffer

2.1.7 Oligonucleotide primers

Table 2.2 Oligonucleotide primers for site directed mutagenesis of PmCaiT

Mutation	Forward and reverse primer sequence
PmCaiT A97C	5'- CTTTATGATGTTTTGTTCTTGTACATCAGCG -3' 5'- CGCTGATGTACAAGAACAAAACATCATAAAG -3'
PmCaiT S98C	5'- CTTTATGATGTTTGCTTGTTGTACATCAGCGGC -3' 5'- GCCGCTGATGTACAACAAGCAAACATCATAAAG -3'
PmCaiT A97C/S98C	5'- GATCTTTATGATGTTTTGTTGTTGTACATCAGCG -3' 5'- CGCTGATGTACAACAACAAAACATCATAAAGATC -3'
PmCaiT T263C	5'- GTGATGTGCGTTGTTACCTGAGCTTCTTAATG -3' 5'- CATTAAGAAGCTCAGGTAACAACGCACATCAC -3'
PmCaiT F334C	5'- CATTCAAATGAGTATCTGCTTAGCGCGTATTTC -3' 5'- GAAATACGCGCTAAGCAGATACTCATTTGAATG -3'
PmCaiT A425C	5'- CTTTAATCAATTGCTGCTCTTACACACTAGC -3' 5'- GCTAGTGTGTAAGAGCAGCAATTGATTAAAG -3'
PmCaiT W316R	5'- GTTTTCCTCAGGCTCGGACTGTCTTCTATTG -3' 5'- CAATAGAAGACAGTCCGAGCCTGAGGAAAAC -3'
PmCaiT S259A	5'- GGGGTAAAAATCGCCGCTGATGTGCGTACTTACCTG –3' 5'- CAGGTAAGTACGCACATCAGCGGCGATTTTTACCCC –3'
PmCaiT T263A	5'- GCCAGTGATGTGCGTGCTTACCTGAGCTTCTTAATG –3' 5'- CATTAAGAAGCTCAGGTAAGCACGCACATCACTGGC –3'
PmCaiT T100A	5'- GTTTGCTTCTTGTGCATCAGCGGCTGTGCTGTTTTGGGGC- 3' 5'- GCCCCAAAACAGCACAGCCGCTGATGCACAAGAAGCAAAC- 3'
PmCaiT T100AS101A	5'- GTTTGCTTCTTGTGCAGCAGCGGCTGTGCTGTTTTGGGGC- 3' 5'- GCCCCAAAACAGCACAGCCGCTGCTGCACAAGAAGCAAAC- 3'

PmCaiT S266A	5’- GATGTGCGTACTTACCTGGCCTTCTTAATGTTAGGTTGGG- 3’ 5’- CCCAACCTAACATTAAGAAGGCCAGGTAAGTACGCACATC- 3’
PmCaiT T421A	5’- GCTTTATCGCCACCGTCGCTTTAATCAATGCCTGC- 3’ 5’- GCAGGCATTGATTAAAGCGACGGTGGCGATAAAGC- 3’
PmCaiT S101A	5’- GTTTGCTTCTTGTACAGCAGCGGCTGTGCTGTTTTGGGGC- 3’ 5’- GCCCCAAAACAGCACAGCCGCTGCTGTACAAGAAGCAAAC- 3’
PmCaiT L422S	5'-GCTTTATCGCCACCGTCACTTCAATCAATGCCTGCTCTTACACACTAGC-3' 5'-GCTAGTGTGTAAGAGCAGGCATTGATTGAAGTGACGGTGGCGATAAAGC-3'
PmCaiT L422T	5'-GCTTTATCGCCACCGTCACTACAATCAATGCCTGCTCTTACACACTAGC-3' 5'-GCTAGTGTGTAAGAGCAGGCATTGATTGTAGTGACGGTGGCGATAAAGC-3'
PmCaiT 206A207A	5'- GCTTTGATCCTAGCAATGGGCGCCGCCCTTGGGCTTGCAACGCC -3' 5'- GGCGTTGCAAGCCCAAGGGCGGCGCCCATTGCTAGGATCAAAGC -3'
PmCaiT R262E	5’- GTAAAAATCGCCAGTGATGTGGAGACTTACCTGAGCTTCTTAATG –3’ 5’- CATTAAGAAGCTCAGGTAAGTCTCCACATCACTGGCGATTTTTAC –3’
PmCaiT R262A	5’- GTAAAAATCGCCAGTGATGTGGCTACTTACCTGAGCTTCTTAATG –3’ 5’- CATTAAGAAGCTCAGGTAAGTAGCCACATCACTGGCGATTTTTAC –3’

2.1.8 Crystallization screens

Index™ (Hampton)

Crystal Screen™ (Hampton)

Crystal Screen II™ (Hampton)

Detergent Screening Kits™ 1 – 3 (Hampton)

Memgold (Molecular Dimensions)

Memgold II (Molecular Dimensions)

MbClass™ (Qiagen)

MbClass II™ (Qiagen)

MemStart™ (Jena Bioscience)

MemSys™ (Jena Bioscience)

JB Screen 1-10 (Jena Bioscience)

2.2 Molecular Biology methods

2.2.1 Polymerase chain reaction

Polymerase chain reaction (PCR) is used to amplify a DNA strand using primers designed to bind the known DNA sequences at both ends of the template strand. It is an iterative process involving three major steps, namely denaturation (strands of the DNA are separated), hybridization (annealing of the primers to both ends of the DNA) and elongation of the new strands (Table 2.4). Elongation of DNA performed by DNA polymerases and in particular Pfu Turbo polymerase (Thermo Scientific) was used in this study (Table 2.3). The PCR product can be purified by Qiagen PCR purification kit, which gets rid of enzymes and primers while the gel extraction protocol removes the enzymes, primers as well as the template strand thus leading to pure amplified DNA.

Table 2.3 PCR reaction composition

Components	Volume (μl)
Pfu Buffer (10x)	5
Template DNA (100-150 ng/μl)	1
Forward primer (100 μM)	0.25
Reverse primer (100 μM)	0.25
dNTPs (2mM each)	5
H2O (autoclaved)	37.5
Pfu DNA polymerase (2.5u/μl)	1
Total volume	50

Table 2.4 standard reaction setup

	Steps	**Temp (°C)**	**Time**	**No: of cycles**
1	Initial denaturation	95	3 min	1
2	Denaturation	95	30s	
3	Annealing	Tm-5	45 s	Steps 2-4 30x
4	Extension	72	2min/kb	
5	Final extension	72	10 min	1

2.2.2 Site directed mutagenesis

Site-directed mutagenesis was performed using the Quikchange Site Directed Mutagenesis Kit (Stratagene) according to the manufacturer's instructions. All constructs we verified by nucleotide sequencing.

2.2.3 Agarose gel electrophoresis

0.8-1.2% agarose gels were cast in TAE buffer (40 mM Tris acetate, pH 8.3) in the presence of Ethidium bromide (final concentration 0.5 μg/ml). Ethidium bromide ensures visualization of the DNA through fluorescence, due to its intercalation between the nucleotide bases in the DNA. The gels were loaded with DNA samples in loading buffer (Fermentas) along with a marker (Fermentas). The DNA due to its negatively charged phosphate groups migrates to the positively charged anode (red) during electrophoresis. The electrophoresis is performed at 100V.

2.2.4 Measurement of DNA concentration

The concentration of double-stranded DNA can be calculated with the optical density (OD) at an absorption maximum of 260 nm (OD_{260}). The reference value is $OD_{260} = 1$ for a pure 50 μg/ml DNA solution. The concentration of 1-2 μl DNA in a final volume of 50-100 μl is measured using a standard disposable cuvette in a Biophotometer (Eppendorf).

2.2.5 Restriction digestion and Ligation

The double stranded PCR product is subjected to digestion by two enzymes (double digestion) in a compatible buffer system (Thermo Scientific) to yield DNA with overhangs or sticky ends. Almost 2 μg of the insert is digested in a volume of 100 μl. The vector DNA in which new gene is to be cloned into is digested using the same enzymes. The reaction is performed at 37°C for 2 hours. A mastermix is usually prepared for performing multiple digestions.

For ligation a vector concentration of around 60 ng in a reaction volume of 20 µl is used. Digested insert at a 3-5 molar excess ratio of vector, is used for ligation. T4 DNA Ligase is used and the reaction is incubated at 22°C for 2 hours before heat inactivating the ligase at 70°C for 5 minutes.

2.2.6 Preparation and transformation of chemically competent cells

Chemically competent *E. coli* cells are produced by the Chung method (Chung *et al.*, 1989). This method uses TSS (Transformation and Storage Solution) medium, which is based on LB medium (Table 2.5).

The *E. coli* strain to be made competent are inoculated (from a freshly streaked agar plate or from a competent cell aliquot) into 100 ml LB medium and grown overnight (37 °C, 125 rpm). The culture is adjusted to an OD_{600} of 0.1 and grown further (20 °C, 125 rpm). Once an OD_{600} = 0.4 (early exponential phase) is reached the culture is then immediately transferred to ice and it is ensured that all the following steps are on ice/ 4°C. The cells are incubated for 30 minutes and pelleted (4°C, 2500 g, 10 min). The supernatant is removed and the cells are resuspended in TSS medium (Table 2.5) with 1/10 of the original culture volume. The cell suspension is then aliquoted (100 – 200 µl) and snap frozen in liquid nitrogen. The aliquots are stored at -80 °C.

Table 2.5 TSS medium

Components	
PEG 8000 (w/v)	10%
DMSO (v/v)	5%
$MgCl_2$	50 mM
Glycerol (v/v)	15%
LB medium	Make up to 50 ml

Sterilized by filtration

For transformation, the aliquots of competent *E. coli* cells (XL-1 Blue, BL21(DE3) pLysS) are thawed on ice. Usually 50ng of plasmid DNA (isolated by Qiagen mini

prep) or 10 μl of a 20 μl ligation reaction is used to transform 100 and 200 μl of competent cells respectively. After the addition of DNA the cells are incubated for 30 minutes on ice which is followed by a heat shock at 42°C for 45-60 seconds. The cells are incubated on ice for 2 minutes followed by the addition of 800-900 μl of LB/ SOC media. The transformed cells are then incubated at 37°C for 45 minutes to 1 hour with shaking, in the absence of any antibiotic. The cells are then centrifuged (table top Eppendorf centrifuge, 4000 rpm, 3 minutes) so that most of the cells can be plated. 800 μl of the supernatant is discarded and the cells are resuspended in 100 to 200μl of the remaining medium. The cells are then plated on the appropriate antibiotic (e.g. ampicillin) resistant plates.

2.3 Biochemical methods

2.3.1 Over expression of recombinant CaiT

Escherichia coli BL21 (DE3) pLysS cells were transformed with pET-15b plasmids carrying CaiT from *Proteus mirabilis* (PmCaiT). The target gene is under the control of a strong bacteriophage T7 transcription. The lacUV5 promoter that controls T7 RNA polymerase is IPTG inducible. The pLysS cells contain an additional compatible plasmid that produces a small amount of T7 lysozyme, a natural inhibitor of T7 RNA polymerase thus ensuring there is no leaky expression of the target gene in the absence of IPTG induction. This enzyme also enables cell lysis by cleaving the peptidoglycan layer of the *E. coli* cell wall when the cells are subjected to freeze-thaw cycles.

For protein production 50-100 ml LB medium (with 100 μg/ml ampicillin) is usually inoculated with a single colony from fresh transformations (or from glycerol stocks) and grown overnight at 37°C at 250 rpm. The starter culture grown overnight is used to induce 1.5L 2*YT medium in a 5*L baffled flask to an OD_{600} of approximately 0.1. Usually 6-12 liters of cells are grown at a time. The cells are grown at 37°C to an OD_{600} of 0.6–0.7. The cells are then induced with 0.5 mM IPTG (Isopropyl β-D-1-thiogalactopyranoside) and grown further for 4 h at 30°C. The cells are harvested by

centrifugation (4000 g, 10 min, 4°C). The cell pellet is homogenized in a buffer containing 25mM HEPES (pH 7.5) and 100 mM NaCl and frozen overnight at -20°C.

2.3.2 Cell lysis

Freezing and thawing of BL21 pLysS cells leads to the disruption of inner membranes of bacteria. This facilitates the release of T7 lysozyme leading to the cleavage of the outer bacterial cell wall made of peptidoglycan. The lysis of cells leads to a highly viscous cell suspension due to the release of genomic DNA. The viscosity of the cell suspension can be reduced by the addition of a pinch of DNaseI (Roche) and passing the cells three times through a potter-douncer. The cells are then filtered before lysing them further in a microfluidizer. The cells, lysate, buffer and the lysis chamber are all kept on ice/cold to avoid the cells from getting heated up during operation. At least 3 passes of the cells at 60,000 psi (8.7MPa) are performed for complete lysis. The cells are pushed through a narrow nozzle at high pressure. Once the cells leave the nozzle they are subjected to expansion and shearing force, which leads to cell disruption. For small-scale cultures the cells are lysed using a sonicator and lysed by liquid shear and cavitation. The sample is kept on ice because sonication generates high heat. To avoid unnecessary heating, short pulses of (5-10 sec) with longer pauses (10-30 sec) are provided. There is increase the efficiency of recovery if sonication is performed on cells that have already been lysed with lysozyme.

2.3.3 Protein purification

Cell debris is removed after cell lysis by low-speed centrifugation (10,000 g, 4°C, 30 min). This is followed by a high-speed centrifugation (125,000 g, 4°C, 1:30 h) step to obtain the membrane fraction. The membranes are homogenized in membrane buffer (Table 2.6) (made at 2X concentration to facilitate the addition of detergent for solubilization) using a potter-douncer. Aliquots of membranes at 10 mg/ml protein concentration are flash-frozen, and stored at −80°C until further use.

Table 2.6 Membrane buffer composition

Membrane buffer (2X)	
HEPES, pH 7.5	50 mM
NaCl	200 mM
TCEP	2 mM
Glycerol (v/v)	20%

2.3.4 Detergent solubilization

The membranes are solubilized overnight at 4°C with 2% (wt/vol) Cymal-5 (5-Cyclohexyl-1-Pentyl-β-D-Maltoside) with constant stirring, followed by high-speed centrifugation (125,000 g, 4°C, 45 min) to remove detergent-insoluble material. For transport assays and fluorescence binding studies, the membranes are solubilized using 2% (wt/vol) DDM (n-Dodecyl β-D-maltoside) for 2 h/ overnight at 4°C.

2.3.5 Immobilized metal ion chromatography (IMAC)

The protein expressed by pET15-b vector has an N-terminal hexa-histidine (His_6) tag followed by a thrombin cleavage site. The basic principle of Nickel/Cobalt IMAC is that the His_6 interacts with the exposed coordination sites of the transition metal that is in turn supported by a solid resin. Imidazole has higher affinity for the metal than histidine, hence a linear gradient of imidazole can be used to elute first the non-specific and later the His_6 tagged protein from the column. 50 mM Imidazole is added to the supernatant before binding it with Ni^{2+}-chelating Sepharose beads (Amersham), to prevent unspecific binding. The Ni^{2+}-chelated sepharose beads or Talon beads are washed in equilibriation buffer before incubating with the supernatant (Table 2.7). The beads are then applied to a gravity flow column and washed extensively with equilibriation buffer to remove any unbound/ non-specific proteins. This is followed by further washing (wash buffer) to remove glycerol. The protein is then eluted using elution buffer containing 200 mM Imidazole in several fractions of 1 ml each (Table 2.7).

Table 2.7 IMAC buffers

Components	Equilibriation	Wash buffer	Elution buffer
HEPES	25 mM	25 mM	25 mM
NaCl	50 mM	50 mM	50 mM
TCEP	1mM	1mM	1mM
Glycerol	10% (v/v)	___	___
Cymal-5/DDM	0.2%	0.2%	0.2%/0.05%
Imidazole	50 mM	50mM	200mM

The elution fractions containing the protein are identified using Bradford assay. The protein fractions are pooled and concentrated to a final volume of 2.5 ml or less (Vivaspin 100 kDa, Sartorius) for buffer exchange in a PD-10 Sephadex desalting column (GE Healthcare).

The PD-10 Sephadex desalting column was equilibriated (Table 2.8) after which the protein (2.5 ml) was loaded on the column. If the total volume of the protein is or <2.5 ml the rest of the volume is made up by adding buffer after the protein sinks into the bed. Protein is eluted in aliquots of 200 – 500 μl with the final elution buffer. For crystallization, the purified protein after buffer exchange was concentrated to 3–5 mg/mL (Vivaspin 100 kDa, Sartorius).

Table 2.8 Desalting column buffer/ Size exclusion chromatography buffer

Components	Crystallization	Transport/Binding
HEPES	25 mM	50mM Tris
Salt	25-50 mM NaCl	25-30 mM KCl
TCEP	1mM	1mM
Detergent	Cymal-5 0.2%	DDM 0.05%

Made in low sodium H_2O

2.3.6 Ion exchange chromatography

Ion exchange chromatography can be used as an additional step in purification to remove the impurities present in the protein sample after the IMAC. This chromatography procedure exploits the protein's overall charge which in turn

depends on the pI (isoelectric point) of the protein and the pH of the buffer in which the protein is present. In cation exchange chromatography (mono S) positively charged molecules are attracted to the negatively charged solid support while the converse is true for anion exchange chromatography (mono Q). Whether a protein binds to the column or not is dependent on the overall surface charge of the protein. Once the protein is applied to the column, it is eluted using a linear salt gradient. The protein of interest could also appear in the flowthrough (while the impurities could be bound to the column).

2.3.7 Gel filtration chromatography/Size-exclusion chromatography (SEC)

SEC is used as a final step in the purification procedure to analyze molecular size and homogeneity of the sample. It is also serves as a way of exchanging the buffer that is suitable for downstream applications (for e.g. crystallization). In addition, SEC can also separate components in a mixture based on their size. During SEC, the sample migrates through a bed of porous beads, wherein the small molecules are adsorbed onto the beads and hence move slowly through the bed while larger molecules move much faster through the void space of the column bed and are hence eluted first.

Analytical SEC was carried out using the Ettan LC system (GE Healthcare) and a Superose™ 6 (3.2/30) column (GE Healthcare). The flow rate was kept constant at 50 µl/min. Sample sizes ranged between 50 and 100 µl. All buffers used during analytical SEC were filtered (exclusion size 0.2 µm) and degassed. The buffer composition remained same as the one used for PD-10 desalting columns (Table 2.8)

For purification of the mitochondrial calcium uniporter (MCU), preparative SEC was performed using Superdex 200 10/300 Increase and Superdex 200 16/60 (GE Healthcare).

2.3.8 Crystallization

Although the crystallization conditions for CaiT have been optimized before, large-scale screening was done using commercial screens in 96-well plates to find new

crystal forms of CaiT that potentially favour other conformational states of the protein. Large-scale screening of crystallization conditions was also done for MCU, the details of which are discussed in the Results secion of Chapter II. Usually a protein concentration of 3-5 mg/ml was used. The purified protein solution was clarified by centrifugation (100,000g, 4°C, 30 min) before setting up crystallization experiments. Crystals of the mutants were mostly grown at 4°C by vapor diffusion in hanging drops of 2 μl protein solution and 1 μL reservoir buffer [50 mM Ca^{2+}-acetate at pH 4.5–5.5, 0–200 mM NaCl, 19–30% (v/v) PEG400]. Small cubic and triangular crystals start appearing overnight or within 2–3 d and were frozen directly in liquid nitrogen with 35% (vol/ vol) PEG400 as a cryoprotectant. New conditions identified through 96-well screening were further optimized using 24-well screens.

2.3.9 Diffraction data collection

X-ray diffraction data of CaiT crystals were collected at Swiss Light Source, PSI, Villigen. Several experimental parameters including radiation wavelength, crystal rotation range and rotation start, exposure time and/or beam attenuation, crystal-to-detector distance, beam size etc. are to be decided during data collection. For data completeness, the most important factors are total rotation range and rotation start position that in turn depend on the crystal symmetry. For each crystal mounted on the beam, 3 image frames, each 45° apart are collected to determine the crystal symmetry. Based on crystal symmetry, the data processing software suggests a starting angle and amount of rotation required to safely cover the asymmetric unit of reciprocal space for the collection of a complete native dataset.

CaiT crystals usually belong to the space group H3 while the ΔN construct and mutants with a ΔN background crystallize in P63 space group. For R262 mutants crystallized in the presence of Rubidium and Thallium, a fluorescence scan is first performed to ensure that the crystal has a bound heavy atom and also to determine the wavelength at which the anomalous scattering signal would be maximized. The fluorescence scan be performed only for backsoaked crystals where the crystals are washed in a cryosolution to remove nonspecifically bound heavy atoms. The data is

then collected with radiation wavelength set to the peak wavelength of the respective heavy atoms.

2.3.10 Data processing (XDS Package)

All the datasets are processed using the XDS package. The package consists of the programs XDS, XSCALE and XDSCONV. XDS is used for the reduction of single-crystal diffraction data recorded on a planar detector by the rotation method using monochromatic X-rays (Kabsch, 2010). XDS program itself has 8 major steps (Table 2.9), which leads to the creation of several output files that can be closely analyzed to understand whether data processing was satisfactory or if it was a failure.

Table 2.9 Data processing steps in XDS

XDS steps	Function
XYCORR	Corrects data images for geometrical distortions
INIT	Classifies pixels as background or diffraction spots
COLSPOT	Locates and saves strong diffraction spots
IDXREF	Finds and refines the orientation, metric and symmetry of crystal lattice
DEFPIX	Forms background table by marking pixels as reliable or untrusted
XPLAN	Supports the planning of data collection by processing a few test images
INTEGRATE	Determines intensity of each reflection
CORRECT	Applies correction factors to the intensities and standard deviations of all reflections generated in INTEGRATE Determines space group if unknown Refines unit-cell parameters Reports the quality and completeness of the data set Saves the final integrated intensities in XDS_ASCII.HKL

2.3.10.1 XSCALE

The scaling program XSCALE

(i) puts one or more files obtained from data processing with XDS on a common scale and reports the completeness and quality of the data sets;

(ii) offers a choice of either combining symmetry-equivalent observations into a

single unique reflection or saving the scaled but unmerged observations in the output file;
(iii) allows scaling of multiple datasets together, a feature that is recommended for MAD data sets taken from the same crystal at different wavelengths;
(iv) determines correction factors that partially compensate for absorption effects, sensitivity variations in the detector plane and radiation damage; and
(v) can correct reflections individually for radiation damage (Kabsch, 2010).

For mutant datasets with Rubidium and Thallium in the crystallization conditions, the data was processed with the parameter FRIEDEL'S LAW=FALSE. The reflections will be unmerged in this case and the Friedel pair will be considered different.

2.3.10.2 XDSCONV

XDSCONV converts reflection-intensity data files from XSCALE/CORRECT into formats required by various software packages for structure determination.

2.3.11 Molecular replacement and refinement

In molecular replacement, phases of a known structure that is similar to the protein of interest are used to estimate the unknown phases. In this study, the CaiT mutant structures were solved by molecular replacement using the wildtype PmCaiT (PDB code: 2WSW) structure as a search model in PHASER. The phasing algorithms in PHASER make use of maximum likelihood and multivariate statistics. When searching for multiple molecules in an asymmetric unit, PHASER forms a search tree, in which all plausible solutions for one molecule are used as a starting point for the search for subsequent molecules. Once the right solution is obtained, the structures are refined with iterative rounds of manual rebuilding in COOT and maximum likelihood energy minimization and isotropic B-factor refinement in PHENIX.

2.3.12 Protein reconstitution into liposomes

The purified protein was reconstituted into liposomes made from *E. coli* polar lipid

(EPL) extract (Avanti). The EPL (25 mg/ml) suspended in chloroform is air dried and resuspended in 25mM HEPES, 1mM TCEP to make 800 μl aliquots of 20mg/ml. These aliquots are used to make liposomes immediately or flash frozen and stored at -80°C. To make liposomes, the lipid aliquot is extruded 15 times in a lipid extruder using a 400 nm polycarbonate membrane (Avestin). The final volume of the liposome solution is made up to 3.2 ml in a glass cuvette using 25mM HEPES, 1mM TCEP yielding a final lipid concentration of 5 mg/ml. The liposomes are then solubilized by titrating in 10% (w/v) Triton X-100 in 2 μl increments and the onset of solubilization is monitored at Abs_{540}. An lpr (lipid to protein ratio) of 10:1 or 15:1 (w/w) is usually used. Protein (in DDM) is slowly added (few μl at a time) to the liposome mixture while stirring it. The proteoliposome mixture is then incubated for 20 minutes at room temperature under gentle agitation. Detergent removal is initiated by the addition of Bio-Beads (SM-2 Macroporous beads, Bio-Rad) suspended in sodium free Tris buffer at pH 7.5. A total of 400-600 mg Bio-Beads in 50 mg to 100 mg steps (every one hour at room temperature) is usually added to every 800 μl EPL aliquot. This ensures the complete removal of detergent and the formation of non-leaky liposomes. Proteoliposomes are then collected by ultra-centrifugation (20°C, 100,000 g, 35 min) followed by washing twice in Tris buffer. The proteoliposomes are finally resuspended in 50 mM Tris buffer to a final lipid concentration of 60 mg/ml and aliquots are flash-frozen and stored at -80°C. Efficiency and the quality of protein reconstitution is verified by freeze-fracture electron microscopy.

2.3.13 Freeze-fracture images

The protein reconstituted into liposomes was analyzed by freeze-fracture electron microscopy (EM) to assess the distribution of the protein on the liposomes as well as to understand the liposome morphology. In freeze-fracture EM, the sample is frozen to observe biological structures with minimal damage to the specimen. Freeze-fracture images provide a planar view of the internal organization of membranes or surface structures of cells and their components. Making a freeze-fracture replica involves four essential steps:

(i) Rapid freezing of the specimen

(ii) Fracturing of the specimen usually under vacuum by using a liquid-nitrogen-cooled microtome blade or by breaking the frozen specimen apart in a hinged device

(iii) Making the replica of the frozen fractured surface by vacuum-deposition of platinum and carbon

(iv) Cleaning the replica to remove all the biological material (Severs, 2007)

F. Joos at the MPI of Biophysics performed all the freeze-fracture and imaging steps, using an EM208S electron microscope (FEI). The freeze fracture images below demonstrate the insertion of PmCaiT into liposomes (Fig. 2.1 A,B). Freeze-fracture of proteoliposomes stored at 4°C for a couple of days show a crystalline array of proteins, probably due to an ordered aggregation (crystallization) of CaiT in the lipid bilayer (Fig. 2.1 C,D).

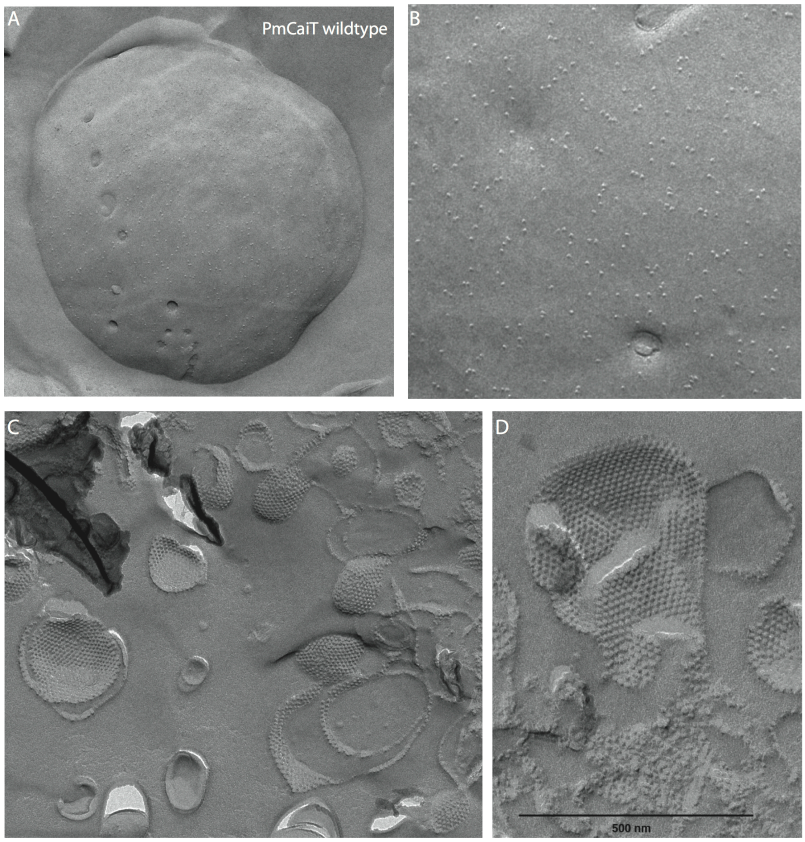

Figure 2.1 Freeze-fracture images of CaiT reconstituted into EPL liposomes

A) An intact liposome packed with reconstituted wildtype PmCaiT B) A closer view of the same proteoliposome showing the CaiT molecules. C) Liposomes that were stored at 4°C show a crystalline array of CaiT similar to what is seen in 2D crystals. D) A closer view of these liposomes reveals the triangular morphology that in turn corresponds to a CaiT trimer.

2.3.14 Radioactive carnitine uptake assay

For uptake assays, the proteoliposome aliquots are preloaded with 50 mM Tris at pH 7.5, 1 mM TCEP, and 10 mM γ-butyrobetaine in two freeze–thaw cycles. After the second freeze–thaw cycle, the proteoliposomes are extruded 15 times through a 400-nm membrane filter (Avestin). The extraliposomal substrate is removed by ultracentrifugation (100,000 g, 20 °C, 30 min), and the proteoliposomes are washed twice with buffer (50 mM Tris at pH 7.5, 1 mM TCEP). Substrate exchange is measured by recording the uptake of L-[N-methyl ^{14}C] carnitine hydrochloride (^{14}C-L-carnitine, Perkin-Elmer) into proteoliposomes.

Substrate uptake was initiated by the addition of a 1 µL aliquot of the proteoliposome suspension into a 200µL reaction buffer (50 mM Tris at pH 7.5, 1mM TCEP) with the concentration of [^{14}C]-L- carnitine (2.5 µCi/mL) kept at 40 µM. In addition, 50 mM NaCl was always included in the reaction buffer for Na^+-dependent uptake activity measurements performed with the R262 mutants. For membrane potential measurements, the proteoliposomes also were preloaded with 50 mM KCl, and the reaction buffer was supplemented with 1 µM valinomycin and 50 mM NaCl. For transport kinetics measurements, the concentration of [^{14}C]-L-carnitine was varied from 0.3 to 60 µM. At various times, reaction was stopped by filtering aliquots of the reaction on a Millipore membrane filter (0.22 µm), followed by washing with 3.5 mL of ice-cold Tris buffer (25 mM at pH 7.5). [^{14}C]-L-carnitine uptake was determined with a TRI-CARB 1500 scintillation counter (Canberra-Packard).

2.3.15 Tryptophan fluorescence substrate-binding assay

Tryptophan fluorescence refers to the intrinsic fluorescence of a protein that occurs

when a protein sample is excited at 280 nm or higher wavelengths. Excited tryptophans lead to emissions at around 348 nm. Tryptophan fluorescence can be used to measure the binding affinity of a substrate to a protein by monitoring substrate-induced changes in tryptophan fluorescence. If the tryptophan residue is more exposed to aqueous media following substrate-induced conformational changes, the fluorescence is more quenched compared to the absence of substrate. Conversely, when the tryptophan residue becomes more buried in the hydrophobic core, there is an increase in the fluorescence signal.

Tryptophan fluorescence was used for measuring substrate-binding affinity in CaiT since the substrates L-carnitine and γ-butyrobetaine are known to bind to a highly conserved tryptophan box at the central substrate-binding site. This binding was seen to influence the tryptophan fluorescence spectrum in CaiT (Jung, 2002). Binding of L-carnitine was measured using CaiT in DDM (10 μM) or with proteoliposomes diluted to 10 μM, in 50 mM Tris at pH 7.5 and 1 mM TCEP with or without 50 mM NaCl. The final volume of the reaction was 1 ml. L-carnitine concentration was increased from 0.6 to 175 mM. The fluorescence emission was recorded using the F-4500 Fluorescence Spectrophotometer (Hitachi). A wavelength scan was performed with the excitation wavelength set to 295 nm and recording the emission spectra between 305 and 390 nm. The scan speed was set to 240 nm/min. The excitation and emission slit widths were set to 2.5 nm and 5 nm, respectively. Data were fitted, and apparent Kd values were obtained using GraphPad Prism.

2.3.16 Microscale thermophoresis

Microscale thermophoresis (MST) was also employed to measure the substrate binding affinity of PmCaiT and its mutants. Due to the low affinity (2-5 mM) of the substrate to CaiT, a method such as isothermal titration calorimetry (ITC) is difficult to perform owing to the requirement for large amounts of protein. On the other hand MST requires much less sample when compared to ITC. It measures substrate affinity in any buffer or a complex bioliquid. This method operates by detecting changes in the hydration shell, charge or size of molecules. Any change of the hydration shell of biomolecules due to changes in their primary, secondary, tertiary

and/or quaternary structure affects the thermophoretic movement. Any change in thermophoretic properties is observed as a change in the fluorescence intensity, which is then used to determine binding affinities with high accuracy. During an MST experiment, an infrared laser shining on a capillary containing the sample induces a microscopic temperature gradient. The resulting local changes of fluorescence intensity due to the motion of labeled molecules in the glass capillaries are monitored.

Our experiments involved Cy5 labeling of protein and a buffer exchange into 25mM HEPES pH 7.5, 50mM NaCl, 0.2% Cymal-5 and 1 mM TCEP while removing excess dye. The final concentration of the protein in the capillaries was maintained constant at around 0.5 μM. Substrate concentration was varied from 3 μM to 50 mM. The total sample volume for each concentration of the substrate was 8-10 μl. Standard capillaries gave most uniform fluorescence peaks and lacked any artifacts as opposed to hydrophobic and hydrophilic capillaries that showed sample sticking. Also a laser voltage of 1.8 V was most effective in giving a meaningful binding curve compared to 1.0 or 1.4 V. The values of the binding dissociation constants obtained are in agreement with the tryptophan fluorescent binding assays (Fig 2.2).

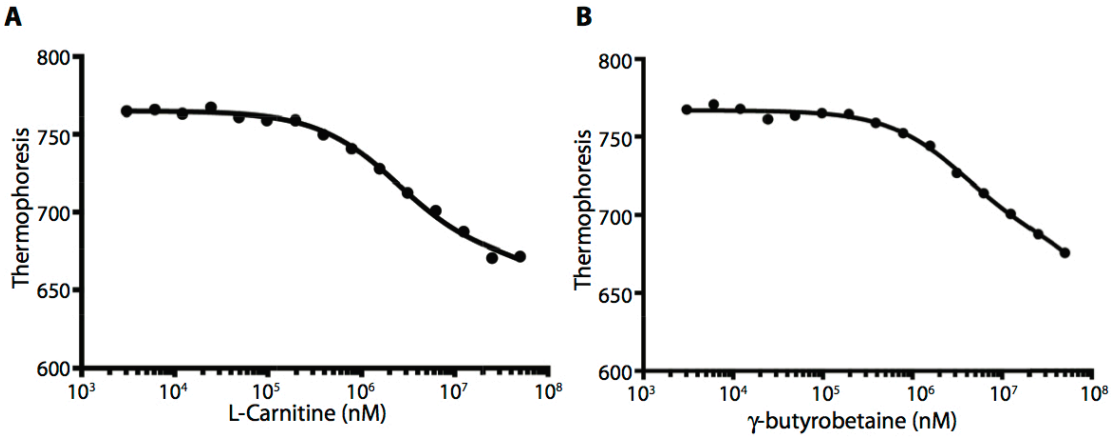

Figure 2.2 Microscale thermophoresis of PmCaiT wildtype

A) One-site total binding model for the MST analysis of L-carnitine binding to PmCaiT gives a Kd of 2.4 mM. B) The binding affinity of g-butyrobetaine for CaiT is 3.8 mM.

However, MST failed to measure the binding affinities of CaiT R262 mutants for the

substrate, probably due to the very weak binding affinities as shown subsequently by tryptophan fluorescent binding measurements.

2.3.17 Homology Modeling

CaiT from *P. mirabilis* was modeled using BetP in the closed [Protein Data Bank (PDB) code 4AIN, chainA] and outward-open (PDB code 4DOJ, chain B) conformation with Modeler 9.11 (Eswar *et al*, 2008). Twenty models were generated for each conformation, and the five with lowest energy were further analyzed using MolProbity. Of these, the model chosen for further analysis had 93.7% and 90.5% of the residues in Ramachandran-favored regions, for closed and outward-open conformations, respectively.

2.3.18 Sequence Alignment

The structures of LeuT type transporters with a high degree of structural similarity to the PmCaiT structure (PDB code 2WSW) were obtained on the Dali server (Holm & Rosenström, 2010). The rmsd of the structures varied from 2.2 to 4.4 Å. A multiple sequence alignment of these proteins was generated from the 3D alignment of protein structures with PDBeFold (SSM), and the resulting alignment was manually checked and corrected (Krissinel & Henrick, 2004).

3 Results

3.1 Biochemical and structural characterization of R262 mutants

Structural comparison of various LeuT fold transporters shows that R262 in CaiT occupies the corresponding Na2 site in Na^+ dependent transporters (Fig 1.10). Akin to CaiT, the proposed H^+-coupled broad-specificity amino acid transporter ApcT also contains a positively charged amino acid residue (K158) at the Na2 site (Shaffer *et al*, 2009). This K158 residue, buried in the protein interior, was predicted to have a pKa that is 3–4 units below the pKa of a free lysine residue in solution (10.53). Hence K158 in ApcT was proposed to undergo protonation/ deprotonation cycles that facilitate substrate transport. A similar analysis in CaiT revealed that the R262 sidechain has a pKa of 10.5 in its microenvironment (Li *et al*, 2005). A pKa of 10.5 for R262 is too high for it to undergo protonation/deprotonation under physiological conditions. Moreover, previous studies have shown that transport in CaiT is independent of an electrochemical proton gradient (Jung, 2002); however, the exact experimental conditions were not described. We therefore measured the L-carnitine uptake activity of PmCaiT in a wide pH range from 5 to 11, both within and outside proteoliposomes.

PmCaiT was expressed, purified and reconstituted into *E. coli* polar lipid (EPL) liposomes, as described in the methods section. The proteoliposomes were preloaded with 10mM γ-butyrobetaine and the uptake of [^{14}C] L-carnitine was measured. It was observed that CaiT is maximally active when the pH was adjusted to 7 both inside and outside the proteoliposomes (Fig 3.1). Applying a pH gradient across the membrane could not increase the substrate uptake significantly. This indicates that R262 does not undergo a protonation/ deprotonation cycle in CaiT, as it was proposed for K158 in ApcT. This points to a different substrate transport mechanism in CaiT when compared to ApcT.

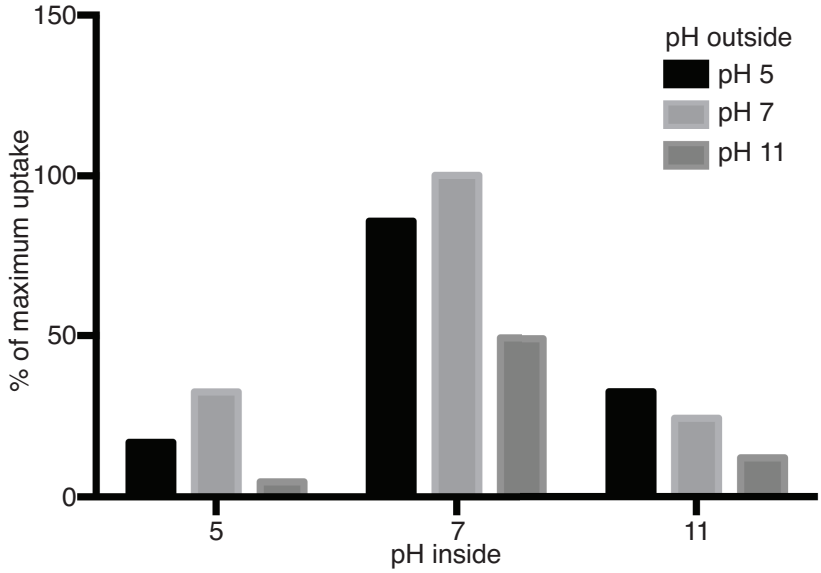

Figure 3.1 pH-dependent L-carnitine uptake of wild type PmCaiT

[^{14}C] L-carnitine uptake activity was measured using proteoliposomes preloaded with 10mM γ-butyrobetaine. The pH inside the proteoliposomes is denoted on the x-axis and the pH of the external medium differs for each bar, as indicated. The maximum L-carnitine uptake activity at pH $7_{in}/7_{out}$ is taken as 100% while the others are shown relative to this.

3.1.1 Purification and activity measurements

To understand the role of R262 in CaiT transport mechanism, we changed this residue into a neutral alanine (R262A) or a negatively charged glutamate (R262E) in PmCaiT. The R262A and R262E mutants were expressed, purified, and reconstituted into liposomes. The size exclusion chromatography profiles of the mutants confirm the trimeric architecture of both mutants, similar to the wild type (WT) protein. Both mutants remain stable throughout the purification procedure (Fig 3.2). CaiT wild type and the mutant proteins migrate at around 45kDa in an SDS gel, a factor of 1.25 lower than the predicted molecular weight of 56.3 kDa.

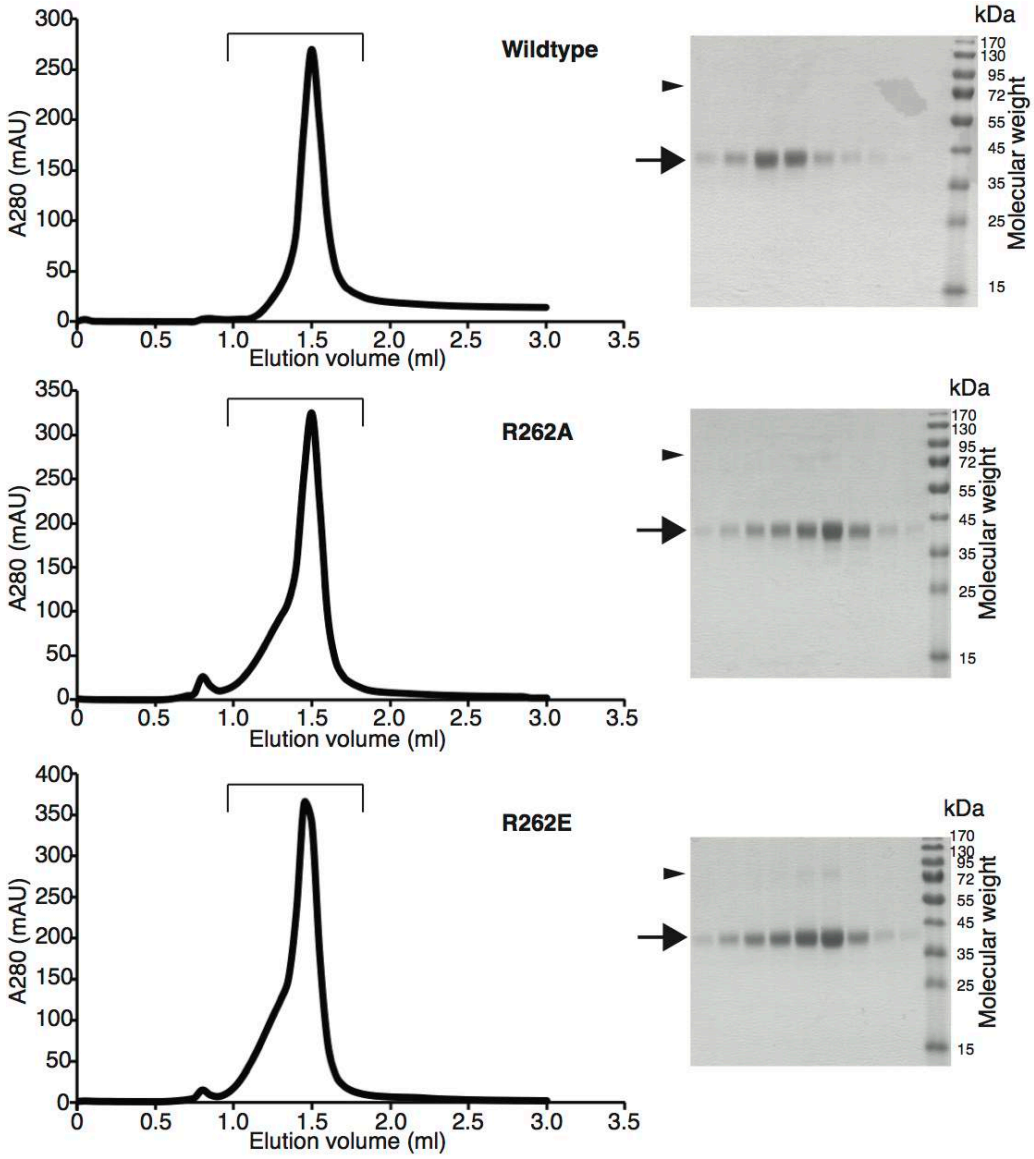

Figure 3.2 Analytical size exclusion chromatography of PmCaiT wild type and R262 mutants
Both the wild type and the R262 mutants elute at around 1.5 ml from a Superose-6 (3.2/30) column. The small peak in the void volume (around 0.8ml) is due to aggregated protein. The right panel shows the corresponding SDS gel of the peak fractions obtained in SEC. The arrow indicates the monomeric protein and the arrowhead indicates the protein trimer.

The proteoliposomes were preloaded with 10 mM γ-butyrobetaine and assayed for uptake of [^{14}C] L-carnitine. Although the wild type protein showed robust uptake of L-carnitine, it was drastically reduced in the R262A and R262E mutants, indicating the importance of R262 for CaiT transport activity (Fig 3.3).

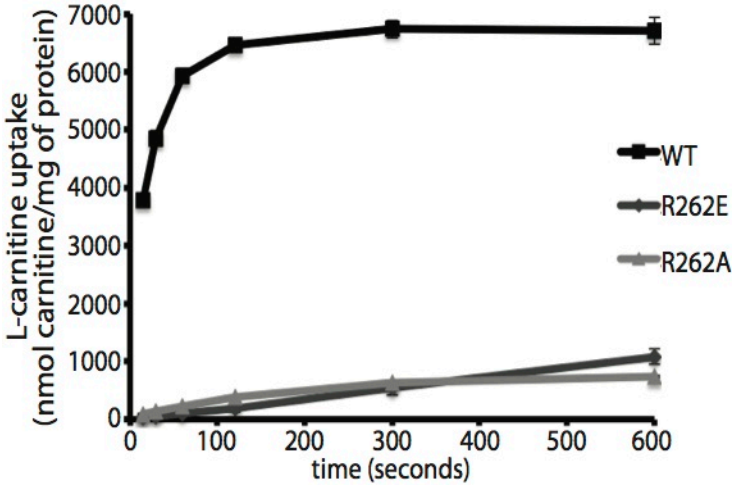

Figure 3.3 L-carnitine uptake by PmCaiT wild type and R262 mutants

Proteoliposomes were preloaded with 10 mM cold γ-butyrobetaine, and counterflow uptake activity of 40 μM [^{14}C] L-carnitine was measured.

3.1.2 R262 mutants are Na^+ specific

Since the positively charged R262 sidechain was proposed to replace the Na2 ion in CaiT, it was tested whether the activity of mutants R262E and R262A could be rescued by adding NaCl to the transport assay. Indeed, addition of 50 mM NaCl to the reaction buffer increased the uptake activity of R262E and R262A mutants by nearly 12-fold and 3-fold respectively when compared to the uptake activity in Na^+-free buffer (Fig 3.4).

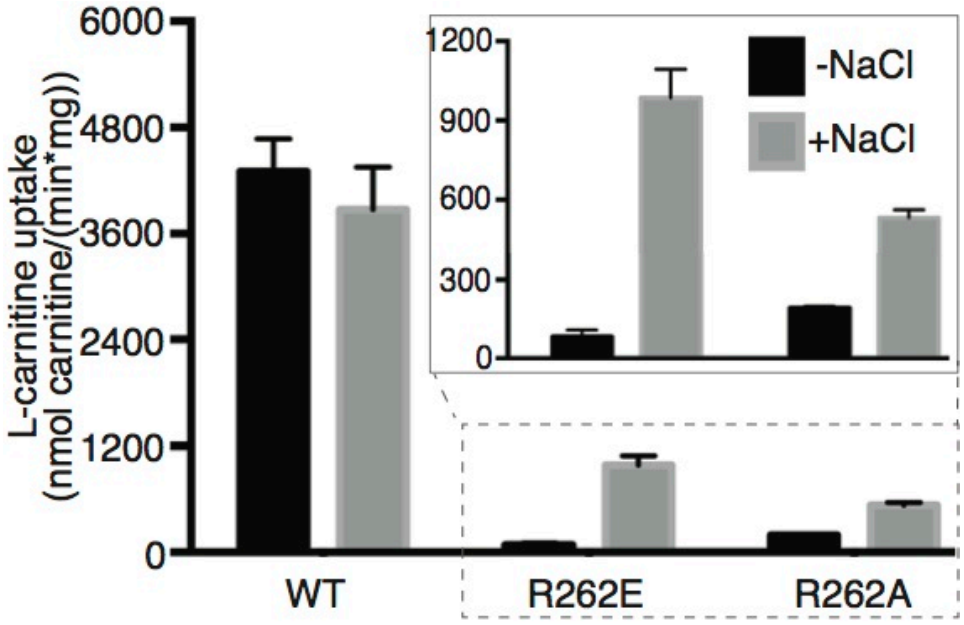

Figure 3.4 Na^+-dependence of L-carnitine uptake by PmCaiT wild type and R262 mutants

Initial rates of L-carnitine uptake by proteoliposomes with or without 50 mM NaCl. Inset shows the uptake activities of R262E and R262A and the effect of Na^+ on the uptake activity.

To test if the stimulation of transport activity seen in R262 mutants is specific to sodium ions, uptake assays were performed with various salts (50 mM NaCl/NaBr/LiCl/KCl) in the external medium. Although NaCl and NaBr increased the [^{14}C] L-carnitine uptake activity of the R262E mutant to similar levels, KCl did not stimulate uptake activity significantly (Fig 3.5). The increase in uptake in the presence of LiCl was about 40% compared with NaCl. This indicates that uptake is, in fact, preferentially stimulated by sodium ions and that the protein can accommodate Li^+ better than K^+.

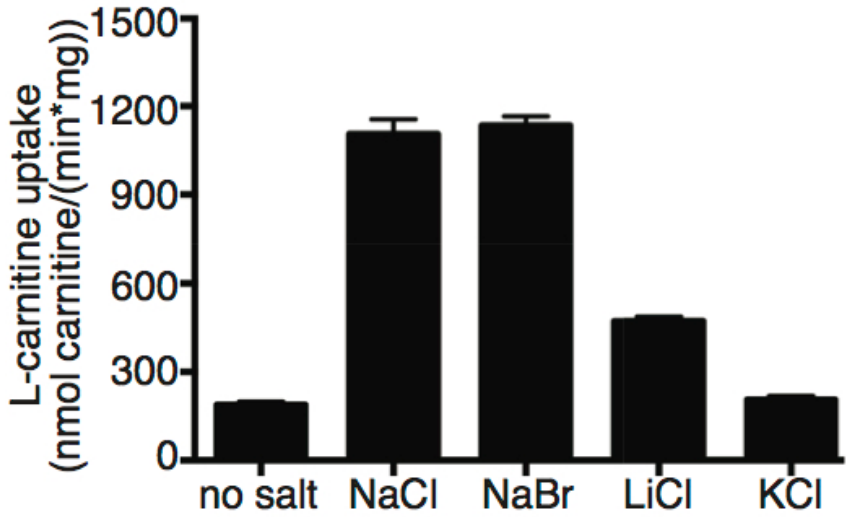

Figure 3.5 Increase in R262 uptake is specific for sodium ions

Initial uptake activity rates were measured in the absence of salt or in the presence of 50 mM NaCl, NaBr, LiCl, or KCl.

Hyperosmotic external buffer can lead to water efflux from proteoliposomes causing liposome shrinkage (Rübenhagen, 2001). This might result in an increase in the relative concentration of cold substrate preloaded in proteoliposomes, which in turn could lead to enhanced substrate uptake. In order to exclude this possibility, we varied the NaCl concentration both inside and outside the proteoliposomes to create different osmotic conditions, and assayed the uptake activity (Fig 3.6). We found that the maximum uptake activities of both R262A and R262E mutants occurred under iso-osmotic conditions, in which 50mM NaCl was present both inside and outside the proteoliposomes. This ruled out the possibility of an increased uptake resulting from liposome shrinkage. Both R262 mutants of CaiT are therefore sodium-dependent, similar to BetP or LeuT.

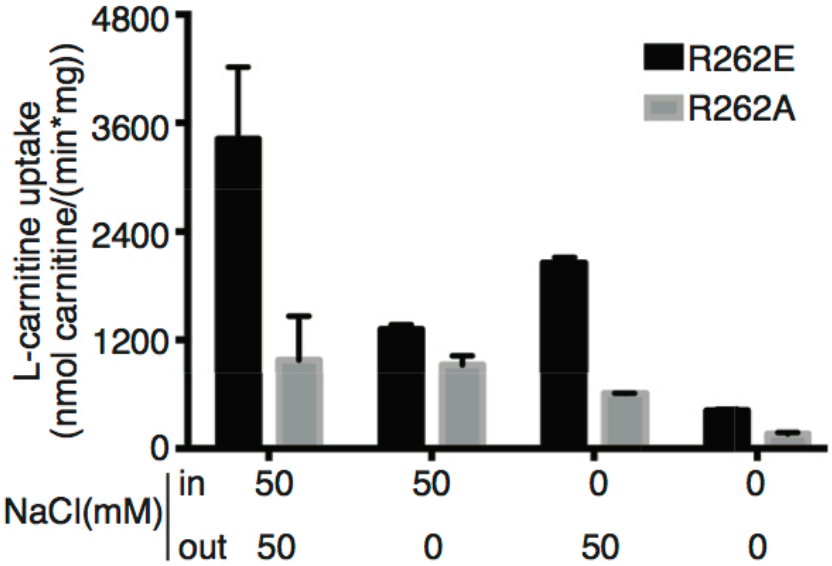

Figure 3.6 Na^+-dependent uptake by R262 mutants under different osmotic conditions
Various combinations of NaCl concentrations were used inside and outside the proteoliposomes to ensure that the observed effects of Na^+ dependency were not due to liposome shrinkage.

Additionally, it was tested whether the Na^+ dependence of these mutants could be saturated. Again, initial uptake rates were measured while the Na^+ concentrations were increased from 0.1 to 100 mM outside the proteoliposomes. Uptake kinetics revealed an apparent K_m (Na^+) of 0.45 ± 0.1 mM for R262E and 0.70 ± 0.2 mM for R262A (Fig 3.7). This indicates much higher Na^+ affinities of the CaiT mutants when compared to the Na^+ affinity of the Na^+-dependent symporter BetP (K_m = 3.8 ± 0.9mM) (Khafizov *et al*, 2012).

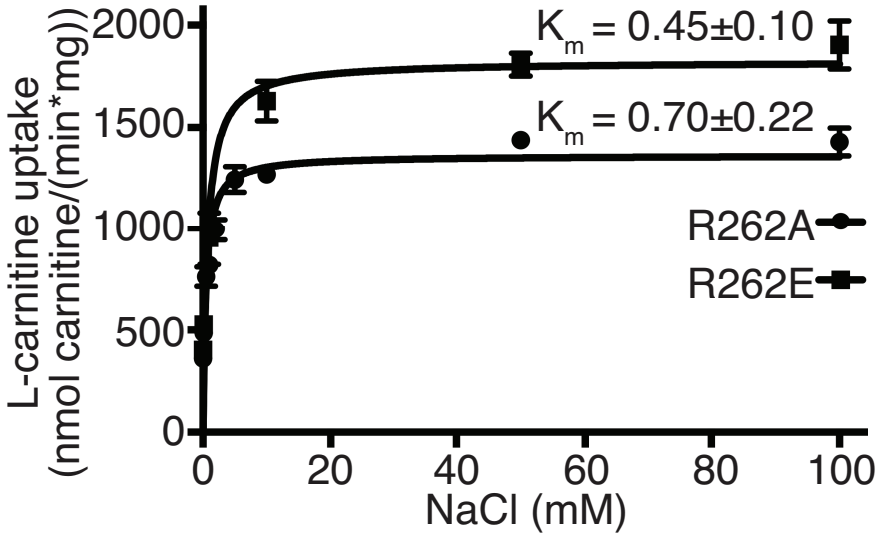

Figure 3.7 Na^+ dependence of R262 mutants can be saturated

Initial uptake rates by R262 mutants were measured, while the Na^+ concentration was increased from 0.1 to 100 mM.

3.1.3 Electrogenic transport of R262 mutants

Substrate transport by the sodium-coupled symporters LeuT and BetP is known to be electrogenic. Previous work has shown that CaiT is electroneutral, as transport activity is ion-independent (Jung, 2002). Moreover, the substrates L-carnitine and γ-butyrobetaine are zwitterionic but uncharged at physiological pH. Since R262 mutations made CaiT Na^+-dependent, it was tested whether these mutants could also transport sodium. This was addressed by monitoring the transport rates of the mutants in the presence of an inside-negative membrane potential. Proteoliposomes were preloaded with 10 mM γ-butyrobetaine and 50 mM KCl (inside-negative), followed by the addition of 1 μM valinomycin and 50 mM NaCl to the external medium. For both mutants, R262A and R262E, addition of valinomycin resulted in a 30–40% increase in uptake activity. In contrast, addition of valinomycin had no effect on the activity of the wild type (Fig 3.8). These data suggest that R262 mutants transport substrate in an electrogenic manner.

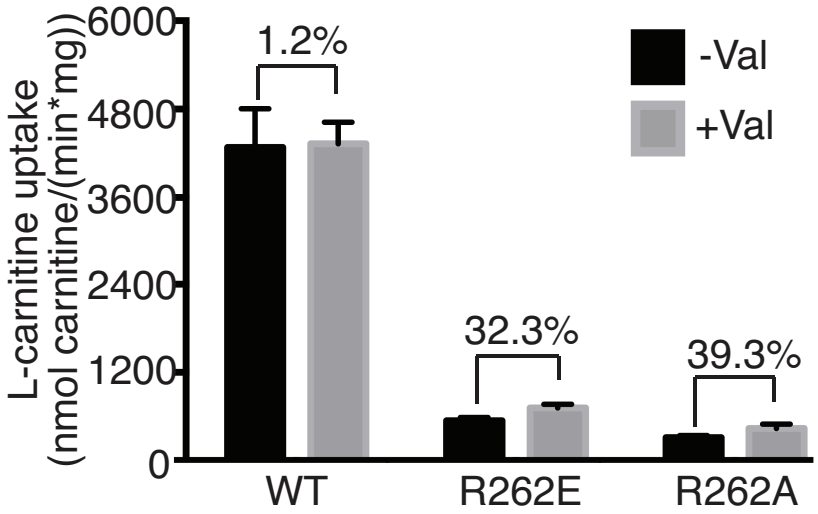

Figure 3.8 Initial [^{14}C] L-carnitine uptake rates of wild type, R262E, and R262A in the absence or presence of valinomycin

Proteoliposomes were preloaded with 50 mM KCl, and 50 mM NaCl and 1 μM valinomycin were added to the external buffer to create an inside-negative potential. A 30–40% increase in uptake activity is observed for both R262A and R262E in the presence of a membrane potential.

3.1.4 Transport kinetics of R262 mutants

The transport kinetics of these mutants was tested in the presence of Na^+. The L-carnitine concentration was varied from 0.3 to 60 μM in the presence of NaCl and initial uptake rates were determined. Wild type and the mutant transport kinetics were obtained from plotting the data and fitting Michealis-Menten-Kinetics. As expected, K_m and K_{cat} values obtained for mutant proteins are significantly reduced when compared to the wild type (Fig 3.9, Table 3.1).

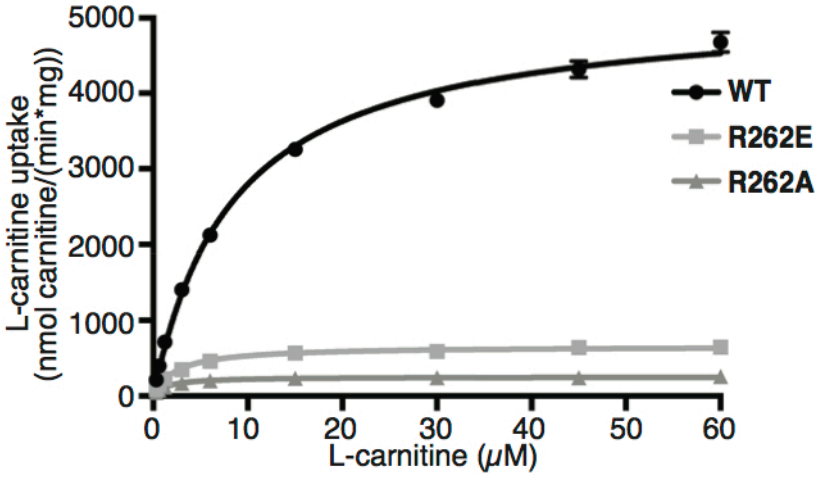

Figure 3.9 Transport kinetics of PmCaiT wild type and R262 mutants

The proteoliposomes were preloaded with 10mM L-carnitine. L-carnitine counter flow was measured by varying the concentration of [^{14}C] L-carnitine from 0.3 to 60 μM outside the proteoliposomes. The kinetics of mutant proteins was measured in the presence of 50mM NaCl both inside and outside the proteoliposomes.

Table 3.1 Kinetic parameters of the wild type and R262 mutants

The kinetic parameters were measured using L-carnitine uptake assays performed in the presence of 50mM NaCl.

	K_m (μM)	Vmax (nmol Car/min*mg)	K_{cat} (sec^{-1})
Wildtype	8.5 ± 0.36	5172 ± 61.8	4.9
R262E	2.4 ± 0.21	660.4 ± 12.8	0.6
R262A	1.4 ± 0.08	254.5 ± 3.07	0.24

3.1.5 Role of R262 in substrate binding - Fluorescent substrate binding measurements of R262 mutants

To test the influence of R262 on substrate binding, tryptophan fluorescence binding assays were performed with R262A and R262E incorporated into liposomes. The binding assays revealed that the apparent substrate binding affinities of the R262

mutants are almost 10-fold lower compared to wild type (Table 3.2). Remarkably, addition of NaCl increased substrate binding of the R262 mutants (Fig 3.10), whereas the wild type protein showed no significant change (Table 3.2), highlighting the influence of Na^+ on substrate binding in R262 mutants. The low affinity of the mutants clearly suggests a role for R262 in substrate binding and explains the effect of the R262 mutations on the transport activity of CaiT.

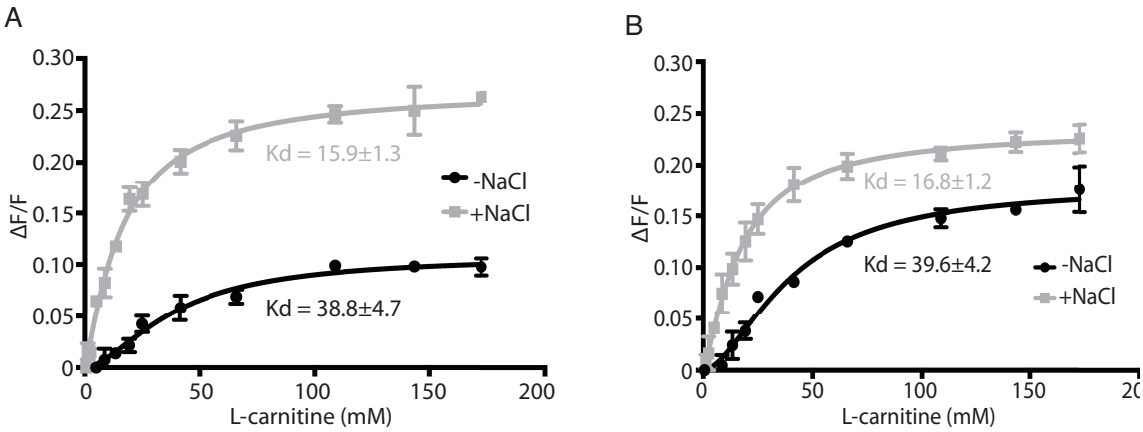

Figure 3.10 Tryptophan fluorescence-based substrate-binding assay with R262E

The increase in tryptophan fluorescence with rising L-carnitine concentration was monitored in the absence and presence of 50 mM NaCl. The relative increase in fluorescence was plotted using a one-site binding model to obtain the apparent K_d values for substrate binding.

Table 3.2 Dissociation constants of the wild type and R262 mutants

The values were obtained from tryptophan fluorescence substrate-binding experiments with L-carnitine in the absence and presence of 50mM NaCl.

	Apparent K_d (mM)	
	-Na^+	**+Na^+**
PmCaiT wild type	3.63 ± 0.4	3.79 ± 0.35
PmCaiT R262E	38.75 ± 4.7	15.9 ± 1.3
PmCaiT R262A	39.6 ± 4.2	16.8 ± 1.2

3.1.6 Crystal structures of R262 mutants in the presence of monovalent cations

3.1.6.1 Crystal structure of R262E

Weakening the affinity of Na^+ binding at the Na2 site was proposed to drive the conformational equilibrium of LeuT fold transporters towards an inward-open state, as the mutation would mimic a sodium ion leaving the binding site (Watanabe *et al*, 2010; Krishnamurthy & Gouaux, 2012; Perez *et al*, 2012). Therefore, it was interesting to see how the R262 mutation in CaiT affects the protein conformation. Moreover, the structure of R262E version of CaiT could further increase our understanding of the Na^+-dependence in R262 mutants. Towards this end, both R262A and R262E forms of CaiT were crystallized. Crystals were grown in a similar condition as the wild type but in the presence of NaCl with the intent of identifying the Na^+ binding site in these mutants. The crystal structure of PmCaiT R262E mutant was determined at 3.3Å resolution by molecular replacement using wild type PmCaiT as the search model (Table 3.3).

The structure is in a substrate-bound inward-open conformation and does not show major structural changes when compared to the available wild type structures (rmsd, 0.37 Å for apo-PmCaiT and 0.64 Å for substrate-bound EcCaiT) (Fig. 3.11A).

The substrate-bound crystal structure of R262E provided us with unique insights into the role of R262 and the unwound part of helix TM1' in substrate binding. The glutamate introduced at position 262 forms strong polar interactions with residues in the unwound helix of TM1' similar to R262 in the wild type protein, whereas the conformation of TM1' remains essentially unchanged (Fig 3.11B). The central substrate-binding site showed density for a substrate while the periplasmic binding pocket observed in EcCaiT structure was empty. Interestingly, the substrate in R262E structure is rotated by about 90° compared to γ-butyrobetaine in the previously reported substrate-bound *E. coli* structure (Fig 3.11B) (Schulze *et al*, 2010). In this orientation, the carboxyl group of γ-butyrobetaine forms polar contacts with the unwound part of TM1'. These polar contacts between the substrate and the TM1'

unwound stretch are seen in BetP, but not in the CaiT structures obtained thus far (Schulze *et al*, 2010; Perez *et al*, 2012). In CaiT R262E crystal structure, these interactions include hydrogen bonds between the substrate and the backbone carbonyl of S98 and a weak interaction with the sidechain hydroxyl group of S101. In this orientation, the trimethyl ammonium head group of γ-butyrobetaine fits perfectly into the tryptophan box constituted by W323, W324, and W147 (Fig 3.11 B, C). Notably, the W323 sidechain is rotated by around 90° in contrast to the substrate-bound *E. coli* structure to accommodate the substrate in the present orientation (Fig 3.11B). The interaction between the unwound part of TM1' and the substrate, together with the known role of R262 in the stabilization of the unwound stretch of helix TM1' (Schulze *et al*, 2010) and the tryptophan fluorescence binding measurements suggest an indirect role for R262 in substrate binding.

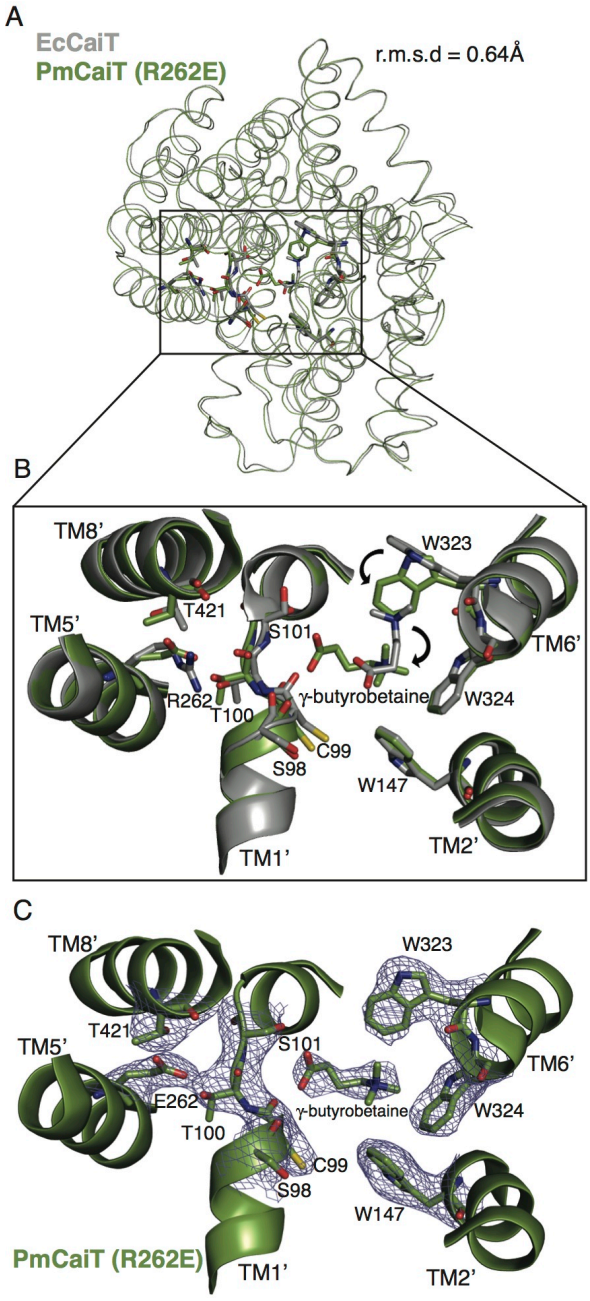

Figure 3.11 Substrate binding in CaiT R262E structure

(A) Superimposition of EcCaiT (chain A) and PmCaiT R262E (PDB codes 2WSW and 4M8J, respectively) reveals an rmsd of 0.64 Å. (B) The central substrate-binding site in the PmCaiT R262E structure with a bound γ-butyrobetaine superimposed on the substrate-bound EcCaiT structure. In the R262E mutant, the substrate has rotated by about 90° compared with the wild type structure. In addition, W323 has reoriented into a position suitable to accommodate the substrate in this new orientation. The trimethyl ammonium head group of the substrate is coordinated by the tryptophan box from TM6' and TM2', whereas the carboxyl group of the substrate is interacting with the backbone carbonyl of S98 in the

unwound TM1' helix. The glutamate at position 262 establishes a hydrogen bond to the unwound TM1' helix. E262 together with T421 from TM8' stabilizes the unwound stretch similar to Arg262 in the wild type structure. (C) 2Fo-Fc map of the central binding site contoured at 1.0 σ.

3.1.6.2 *Crystal structure of R262A in complex with Rb^+*

Lack of electron density for sodium ion at the Na2 site in CaiT R262 mutant structure could be attributed to the low resolution of the structure (3.3 Å) in combination with the weak scattering of the sodium ion. To locate the Na^+ binding site, anomalous scatterers such as Thallium (Tl^+) or Rubidium (Rb^+) were used in co-crystallization trials with CaiT R262 mutants in an attempt to obtain an unambiguous electron density at the Na2 site. The Na^+ dependent mutants of CaiT were co-crystallized in the presence of rubidium chloride. Diffraction data was collected at the rubidium absorption edge. One of the crystals of R262A mutant diffracted to 2.7 Å. The structure obtained after molecular replacement with wild type PmCaiT showed a difference density at the central binding site (Fig 3.12) (Table 3.3). The density was spherical, unlike the bi-lobed density usually observed for the substrates. This indicated that the rubidium ion used in the co-crystallization trials was bound at the central binding pocket of PmCaiT, well coordinated by the tryptophan box (W323, W324 and W147) through cation-π interactions (Fig 3.12). However, there was no detectable ion density close to the Na2 site.

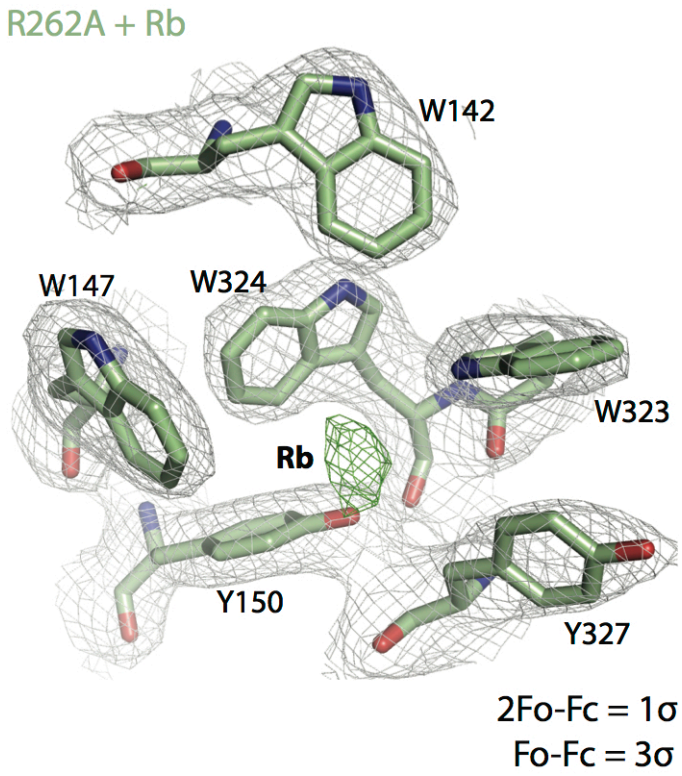

Figure 3.12 Central substrate binding site of R262A + Rb^+ structure

The amino acid sidechain densities are from the 2Fo-Fc map at 1σ while the difference density in green corresponds to the Fo-Fc map at 3σ. The Rubidium ion is well coordinated by the sidechains of W323, W324, W147 and Y150.

3.1.6.3 Crystal structure of R262E in complex with Tl^+

Co-crystallization with Tl^+ was attempted since the ionic radius of Tl^+ (1.02 Å, 6-coordinate; 1.12 Å 8-coordinate) is comparable to that of Na^+ (1.16 Å 6-coordinate; 1.32 Å 8-coordinate). Thallium chloride had been previously used to identify the sodium-binding site of Glt_{Ph} (Boudker *et al*, 2007) and PaNhaP (Wöhlert *et al*, 2013). Due to the higher number of electrons Tl^+ is a much stronger scatterer than Rb^+. Crystals of CaiT R262E were grown in the presence of 1mM of Tl^+. The crystals diffracted to 3.5 Å and the structure was determined using the PmCaiT wild type structure as a search model in molecular replacement (Table 3.3). The structure revealed an anomalous density at the central binding site that is prominent even at 5σ of the Fo-Fc map (Fig 3.13). Similar to the Rb^+ bound R262A structure; R262-Tl^+ structure also has no extra density at the Na2 site. The tryptophan box of the central

substrate-binding site coordinates Tl^+ through cation-π interactions. It appears that in both the Rb^+-bound R262A and Tl^+-bound R262E structures, the binding of the cation at the central binding site was favored due to cation-π interactions with the tryptophan box, which is most likely a non-specific interaction.

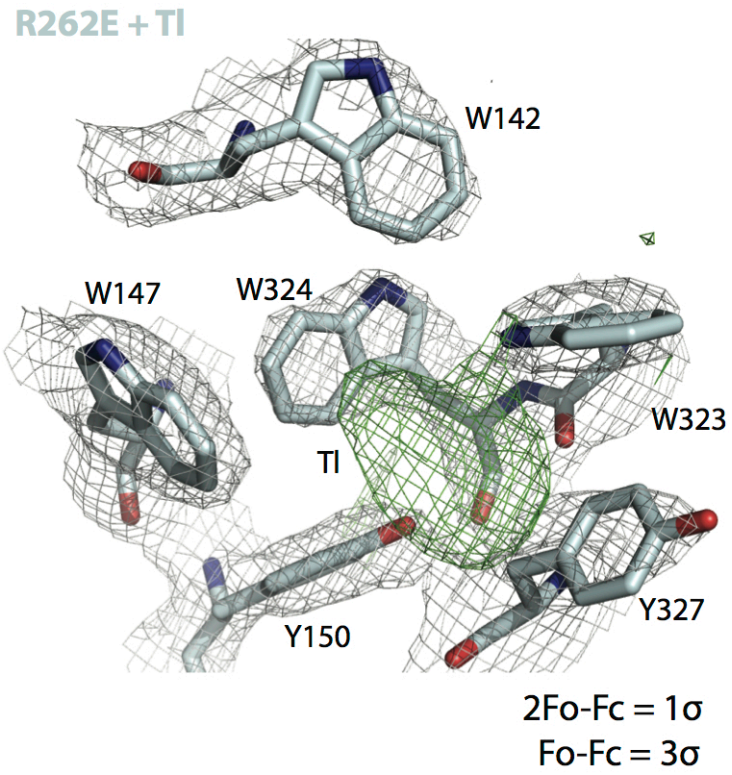

Figure 3.13 Central substrate binding site of R262E + Tl^+ structure

The amino acid sidechain densities in grey are from the 2Fo-Fc map contoured at 1σ while the green density corresponds to Fo-Fc map at 3σ.

Table 3.3 Data collection and refinement statistics for R262 mutants

Data collection	4M8J (R262E)	R262A + Rb^+	R262E + Tl^+
Space group	R3:H	R3:H	R3:H
Cell dimensions			
a, b, c (Å)	129.1,129.1, 160.7	129.5 129.5 160.69	129.2 129.2 161.8
α, β, γ (°)	90, 90, 120	90 90 120	90 90 120
Resolution (Å)	45.90 (3.55 - 3.29)	45.99 (2.798 - 2.7)	46.01 (3.211 - 3.1)
Unique reflections	15128 (3065)	27524 (2721)	18219 (1801)
$I/\sigma I$	5.6 (2.0)	11.58 (2.18)	12.97 (2.99)
Completeness	99.5 (97.9)	99.89 (99.23)	99.76 (100.00)

Refinement			
Protein residues	495	503	496
Number of atoms	3904	3976	3918
Protein	3893	3974	3917
Ligand	10	1	1
Water	1	1	0
R_{work}/R_{free} (%)	23.59/25.70	23.97/28.43	21.12/24.05
Ramachandran favoured (%)	93.7	90	87
Ramachandran outliers (%)	0.4	1	2.6
r.m.s.d. bonds (Å)	0.003	0.009	0.008
r.m.s.d angles (°)	0.800	1.24	1.24
Average B factors			
Protein	53.5	63.60	62.90
Solvent	16.9	65.40	NA

3.1.7 Role of R262 in the transport mechanism of CaiT

In Na^+-dependent transporters, the initial step leading from an outward fully loaded state to an inward state is the hydration of the Na2 site. Na^+ dissociation from the Na2 site facilitates conformational changes, mostly mediated by the unwound, flexible part of TM1' (Watanabe *et al*, 2010; Krishnamurthy & Gouaux, 2012; Perez *et al*, 2012). Since all crystal structures of CaiT are in inward-open conformations with or without bound substrate (CiS and Ci respectively), it is not clear whether a similar mechanism mediated by R262 occurs in CaiT. For a better insight into the dynamics of the Na2 site of CaiT, the closed and the outward-open conformations of CaiT were modeled (Fig 3.14), using the corresponding BetP structures as templates (Perez *et al*, 2012).

The conformational changes leading to the different states of the transporter involve mainly the helices lining the substrate pathway, which leads to the opening or closing of the periplasmic or cytoplasmic pathway, similar to that observed in BetP. Remarkably, R262 occupied different positions in these modeled conformations, each being stabilized by a separate set of hydrogen bonds (Fig 3.14). In the inward-open conformation (Ci), R262 interacted with the sidechains of T100 from TM1', S259 from TM5', and T421 from TM8', as well as the backbone carbonyls of S259 and T263 from TM5'. In contrast, in the modeled closed state (Cc), R262 had long-

distance interactions with the sidechains of S266 from TM5′ and T100 in the unwound part of TM1′. An additional weak interaction was formed to the backbone carbonyl of A97 in this stretch. In the outward-open conformation (Ce), R262 interacts with sidechains of S101 from TM1′ and S266 from TM5′, as well as with the backbone carbonyl of S101. It appears that the displacement of R262 sidechain plays a critical role in regulating the flexibility of TM1′ through alternating interactions. This in turn induces conformational changes in the protein facilitating substrate transport.

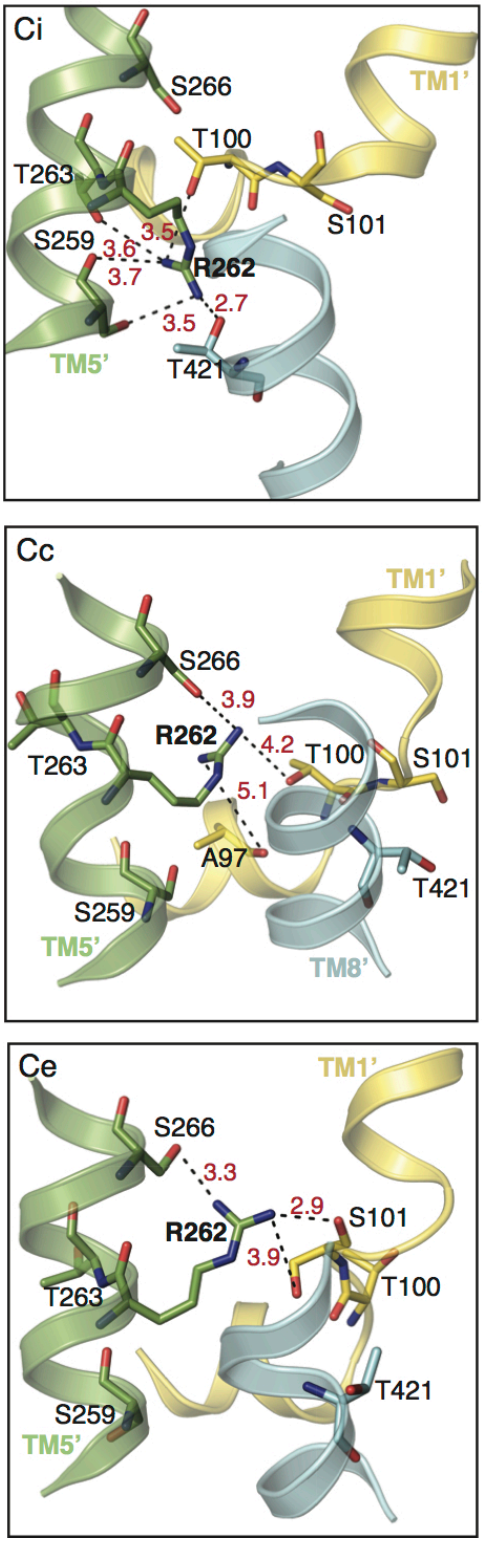

Figure 3.14 Alternating interactions of R262 in different conformations of CaiT

Orientation of R262 in three different conformations of PmCaiT. The inward-open conformation (CiS) is the published CaiT structure (Schulze *et al*, 2010), whereas the closed (Cc) and outward-open (Ce) conformations are modeled based on the crystal structures of

BetP in the corresponding conformations. R262 sidechain oscillates, making and breaking a number of hydrogen bonds, while the transporter moves from the inward-open via the closed state to the outward-open state and then back to the inward-open state. Black dashed lines indicate hydrogen bonds, with bond distances in Å shown in red.

On the basis of the previously described CaiT crystal structures, the residues coordinating R262 during its proposed oscillation cycle were not expected to have a functional role in substrate transport. Therefore, measuring the transport activity of mutants in which these residues had been changed could support the proposed arginine oscillation model. Therefore, residues interacting with R262 in the various CaiT conformations were mutated to alanines. These single mutants were reconstituted into liposomes and their L-carnitine uptake activity was measured. In agreement with the model, all mutants showed a significantly reduced transport activity compared with wild type (Fig 3.15).

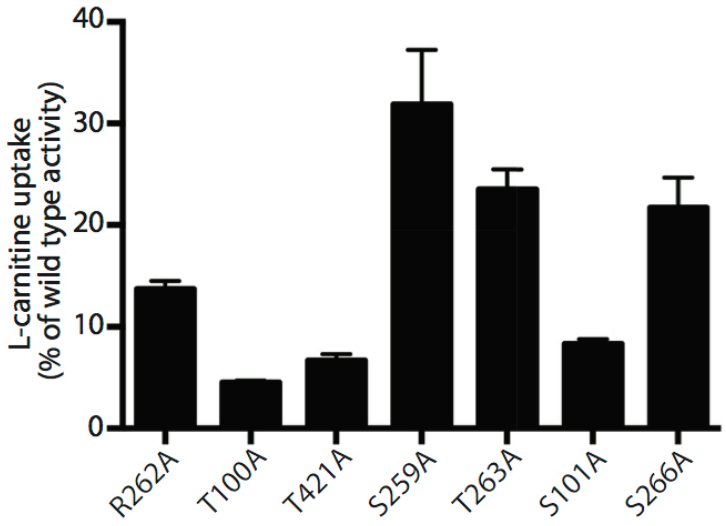

Figure 3.15 Transport activity of mutants of the Na2 site in CaiT

Residues forming hydrogen bonds to R262 in the wild type structure or the two models were mutated to alanine, and transport activity was measured in the presence of 50 mM NaCl. The initial rates of uptake were plotted as a percentage of wild type activity.

It is plausible that in R262 mutants, some of these residues coordinate a Na^+, which would contribute to their Na^+ dependence. To test this, substrate uptake assays were performed on these mutants in the background of R262A. Although

R262A/T100A was still Na^+-dependent, the overall transport activity was much lower than that of R262A alone. This implies that the sidechain of T100 is not crucial for coordinating a Na^+ but still plays a role in substrate translocation. However, the double mutant R262A/T421A completely lost its sodium dependence, suggesting a critical role for T421 in the coordination of Na^+ in the R262 mutants (Fig 3.16A). Interestingly, T421 from TM8' is highly conserved in other LeuT-type transporters (Fig 3.16B), where it is directly involved in Na2 coordination. Mutation of the corresponding residue T467 in BetP affected betaine uptake activity and resulted in significantly increased K_m and K_d in comparison with wild type (Khafizov *et al*, 2012).

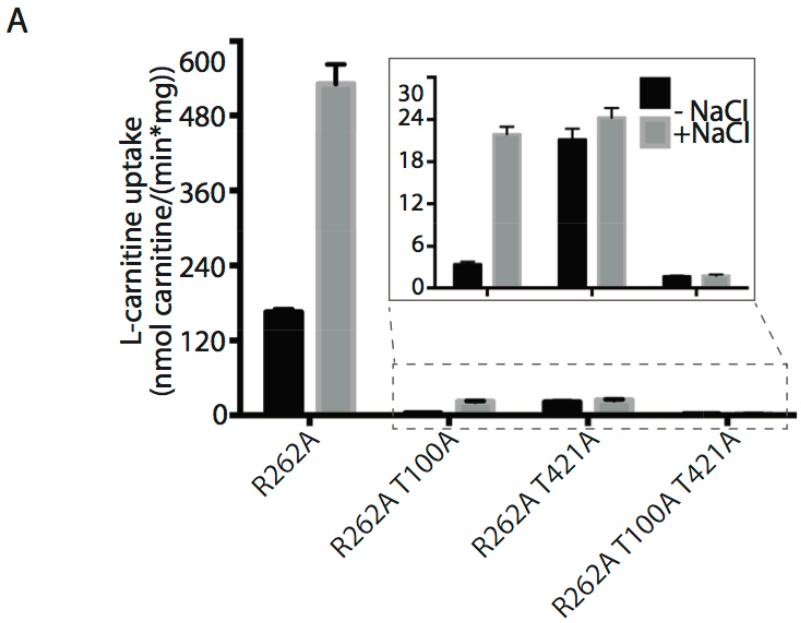

B

```
                                  421
CaiT   403 LST-ATMWGFFILCFIATVTLINACSYTLAMST 434
BetP   449 GGQ-IMGIIAMILLGTFFITSADSASTVMGTMS 480
GadC   289 TVR-VISALLLLGVLAEIASWIVGPSRGMYVTA 320
MhP1   294 VSIpXAILFQVFVLLATWSTNPAANLLSPAYTL 326
LeuT   336 GGT-FLGFLWFFLLFFAGLTSSIAIMQPMIAFL 367
SGLT   350 -----VKGVVFAALAAAIVSSLASMLNSTATIF 377
```

Figure 3.16 Na^+ dependence and sequence conservation of Na2 site in CaiT

(A) Uptake activity of TM1' unwound helix mutants in combination with the R262A mutation in the presence or absence of 50 mM NaCl. (B) Structure-based sequence alignment of TM8'. The alignment of amino acid sequence of TM8' helices from various LeuT-type transporters shows conservation of Thr/Ser residues corresponding to T421 in CaiT. Threonine and serine residues are highlighted in orange, and the black arrow shows the highly conserved Thr/Ser involved in Na2 binding.

These experiments suggest that T100, S101, S259, T263, S266, and T421 are involved in coordinating R262 by stabilizing it in various positions in the course of the transport cycle. It still remains to be seen how exactly this changes the protein conformation, which requires crystal structures in new conformations.

3.2 Biochemical and structural characterization of M331 mutants

The sulphur atom of M331 makes a hydrogen bond with the carboxyl group of γ-butyrobetaine in the EcCaiT structure and hence was proposed to mimic the role of Na1. However, it was shown that mutating M331 to valine, the equivalent residue in BetP, does not make CaiT Na^+ dependent (Schulze *et al*, 2010). A recent biochemical and structural analysis of LeuT fold transporters revealed that the position or even the presence of Na1 is not conserved in this family of transporters. In fact, extensive bioinformatic, biochemical and molecular dynamics studies were required to assign the location of Na1 site in BetP (Khafizov *et al*, 2012).

One feature of EcCaiT crystal structures that set CaiT apart from LeuT and BetP is that the residues of the unwound region from TM1' that is known to play a critical part in ligand binding and transport (Boudker & Verdon, 2010) did not interact directly with the substrate. In addition to M331, the highly conserved tryptophan box, present in all BCCT transporters, interacts through cation-π interactions with the trimethyl ammonium head group of γ-butyrobetaine. Since this aromatic box is known to coordinate several compounds all carrying a trimethyl group (betaine, choline, acetylcholine), it was interesting to know how the substrate specificity is

defined in CaiT. It was proposed that the length of the substrate (distance between the trimethylammonium group and the carboxylate) could be crucial in defining the substrate specificity in CaiT, since both L-carnitine and γ-butyrobetaine are identical except for the presence of a hydroxyl group in L-carnitine (Jung, 2002). Also CaiT does not transport smaller substrates with similar functional groups.

3.2.1 Substrate specificity in M331 mutants

To understand the role of M331 in CaiT, it was replaced by glutamate or lysine or arginine. All the mutants could still be expressed and purified similar to wild type (Fig 3.17).

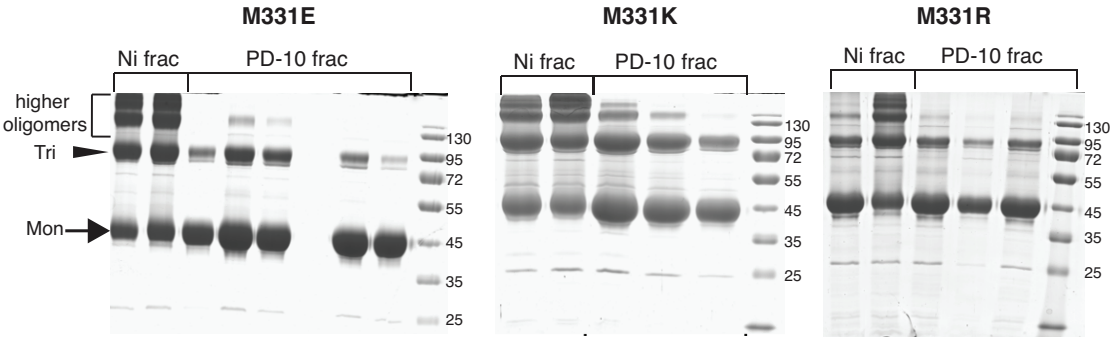

Figure 3.17 SDS-PAGE gel showing purification of M331 mutants

Fractions from the Ni^{2+}-chelating sepharose beads using imidazole elution and PD-10 desalting columns are shown. The monomer is indicated with an arrow, the trimer with an arrowhead. Higher oligomers are also indicated. The CaiT monomer runs at 45kDa in the SDS gel.

M331E and M331K mutants along with PmCaiT wild type were reconstituted into liposomes made from *E. coli* Polar Lipids. Transport assays using reconstituted protein revealed the decrease of substrate transport activity of the mutants in comparison to the wild type protein (Fig 3.18). M331E showed about 10% activity in comparison to wild type while M331K was almost inactive, underscoring the importance of M331 in substrate binding/ transport.

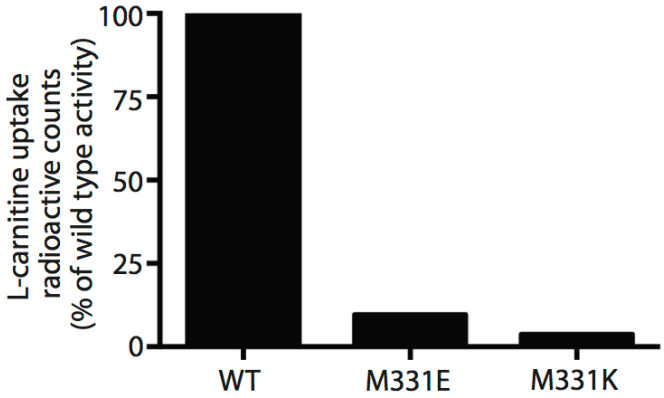

Figure 3.18 Uptake activity assay of M331 mutants in liposomes

Radioactive L-carnitine uptake activity of M331E and M331K were measured and compared with wild type activity. The steady state uptake rates are plotted relative to wild type activity.

The substrate specificity of two CaiT mutants, M331E and M331K were tested in an exit counterflow assay. In this assay, 10 mM non-radioactive substrates like L-carnitine, γ-butyrobetaine and smaller substrates like betaine or choline were added to the external buffer during steady state of uptake. The wild type protein was clearly specific for its substrates L-carnitine and γ-butyrobetaine as indicated by the drop in the amount of radioactive L-carnitine upon adding these substrates to the external buffer (Fig 3.19A). M331E, though showed low uptake activity, was still highly specific for L-carnitine and γ-butyrobetaine (Fig 3.19B). It is interesting to note that M331E showed a slight drop in radioactive L-carnitine over a longer time period following the addition of betaine, indicating slight specificity of M331E for betaine. In spite of being almost inactive, M331K showed specificity for L-carnitine and γ-butyrobetaine and the uptake activity continued in the presence of high concentrations of betaine and choline (Fig 3.19C).

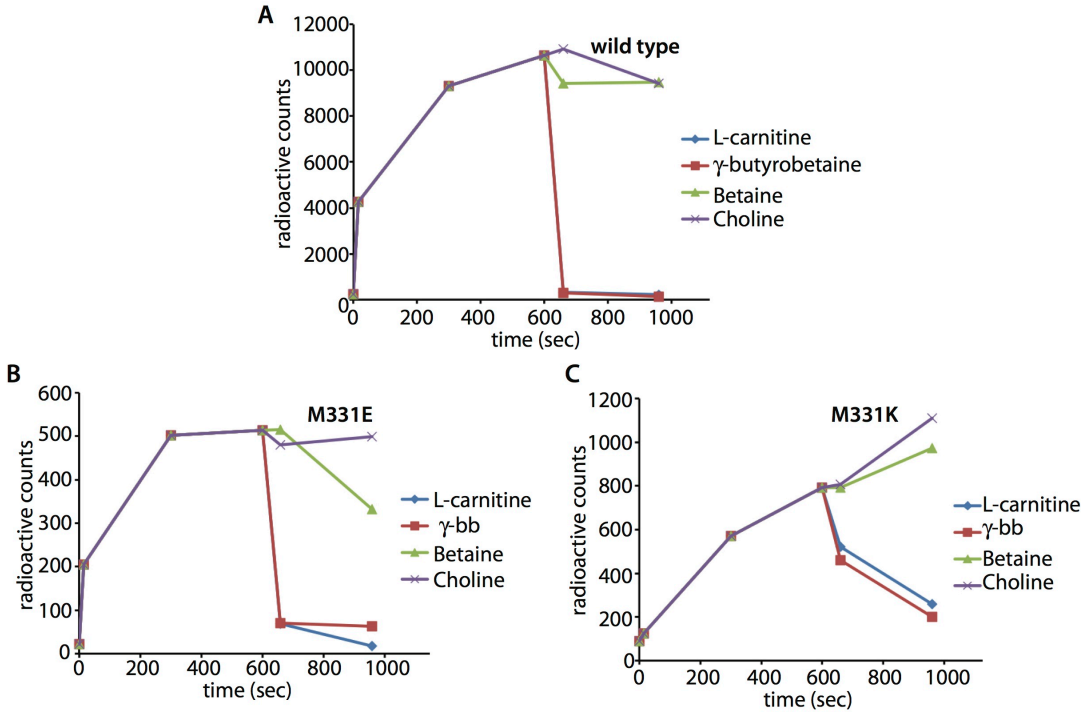

Figure 3.19 Exit counterflow assay for testing substrate specificity of M331 mutants

The non-radioactive substrates were added once the uptake rate plateaued (at 10 minutes time point). Uptake activities of M331E and M331K are much less compared to the wild type activity. γ-bb stands for γ-butyrobetaine.

As observed from the transport assays, M331 did not play a significant role in defining the specificity of the substrate in CaiT. It is possible that the unwound stretch of TM1' could be more important in substrate recognition in CaiT, as it was seen to interact with the substrate in our R262E crystal structure. It has been shown that this stretch is responsible for substrate specificity in BetP where mutating a glycine to an aspartate (G153D) altered the substrate specificity from betaine to choline (Perez *et al*, 2011).

3.2.2 Crystal structure of M331E

Since M331E had a drastically reduced substrate uptake rate in comparison to wild type, it was crystallized in order to see how the protein conformation was affected due to the mutation. Crystals grew in similar conditions as the wild type protein. One of the crystals diffracted to about 2.3 Å. The structure was solved by molecular replacement using the PmCaiT wild type structure (Table 3.4). The protein was in an

inside open conformation with a difference density for the substrate at the central binding site (Fig 3.20A), while the periplasmic binding site appeared empty. The density clearly corresponded to a substrate molecule in its bimodal shape. Interestingly, the substrate was bound in a different orientation compared to the substrate-bound in the EcCaiT structure. In this orientation the major cation-π interaction is with W142, W147 and W324 in contrast to other substrate-bound structures in CaiT where W323 plays the major role in substrate coordination. Hence, W323 remained in the same orientation as in the substrate-free PmCaiT structure and did not rotate to accommodate the substrate as in the EcCaiT structure (Fig 3.20B).

Interestingly, the electron density in CaiT M331E structure corresponds to a L-carnitine molecule, which has an extra hydroxyl group in comparison to γ-butyrobetaine, thus making it the first CaiT structure with bound L-carnitine (Fig 3.20C). Placing γ-butyrobetaine in the central binding site led to unoccupied difference density in the next round of refinement. However, since the hydroxyl group of the L-carnitine did not specifically interact with the protein, it is not clear how CaiT distinguishes between L-carnitine and γ-butyrobetaine.

Introduction of a glutamate at position 331 led to an additional interaction between TM1' and TM6'. E331 from TM6' now forms a hydrogen bond interaction with S98, pulling TM1' by approximately 1 Å towards TM6' (Fig 3.20B). However this does not narrow the cytoplasmic cavity and the bound substrate at the central binding site is solvent-accessible from the cytoplasm.

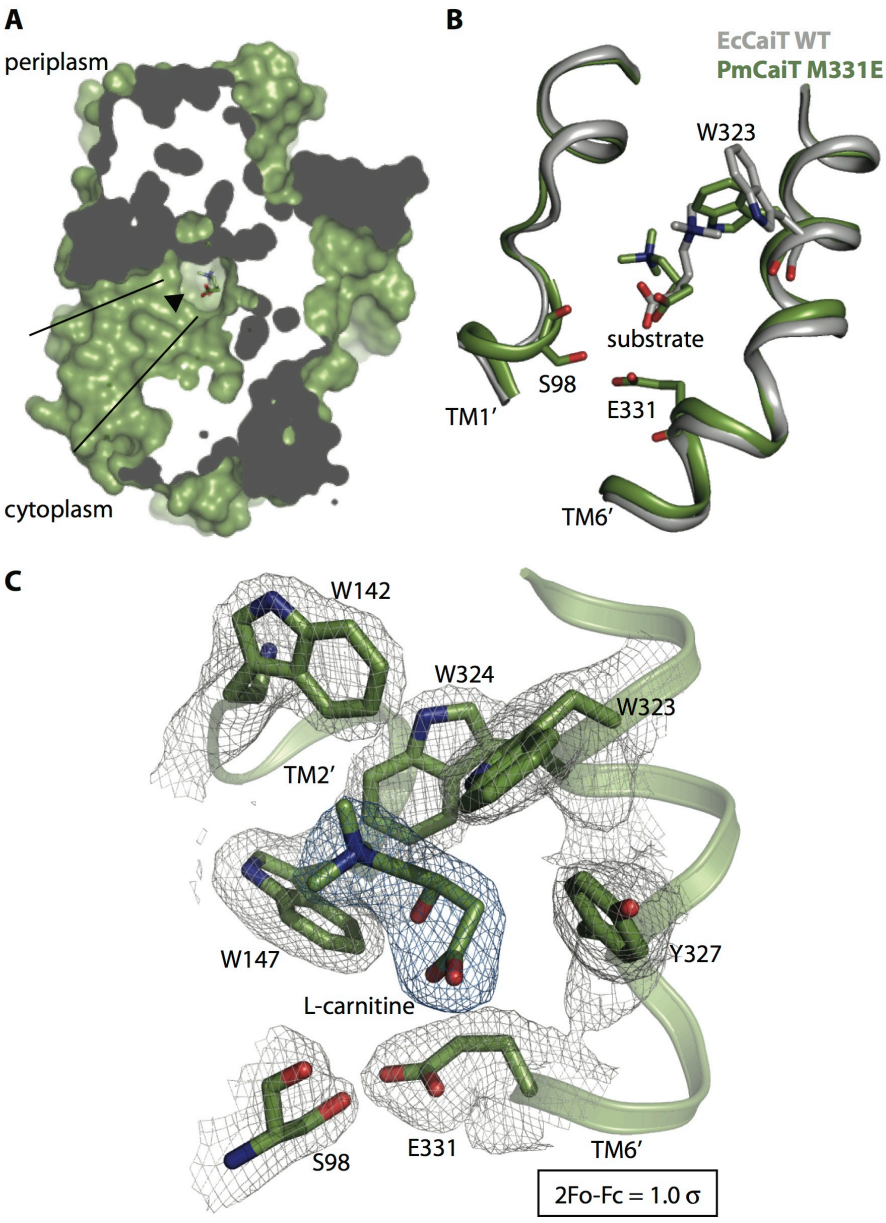

Figure 3.20 Crystal structure of M331E

(A) The mutant M331E is in an inward-open conformation. The substrate in the central binding pocket is accessible from the cytoplasm as shown by the arrowhead and the two black lines. (B) E331 from TM6′ coordinates with S98 from TM1′ pulling the helix closer. W323 rotates by almost 90° in comparison to the substrate-bound EcCaiT structure. (C) 2Fo-Fc map contoured at 1.0 σ showing densities of residues involved in substrate binding at the central binding site. The density of the substrate is shown in blue for clarity.

3.2.3 Crystal structure of M331K

The M331K crystal structure was determined at 3.2 Å resolution. The protein crystallized with two monomers from two different trimers in the asymmetric unit. The structure was solved by molecular replacement with the PmCaiT wild type structure as the search model. The two monomers were refined in the absence of non-crystallographic symmetry (NCS) restraints, considering the possibility that the two monomers could be in different conformations (Table 3.4). Both monomers superimpose with an rmsd of 0.6 Å. There was difference density in the central binding pocket of both monomers, which could not be clearly assigned to any molecule. Interestingly the only noticeable difference between chain A and chain B is in the orientation of residues on TM6'. W323 of both chains have rotated by almost 90° compared to each other (Fig 3.21). Despite being in various rotamer states in different structures, Y327 from TM6' forms hydrogen bond interaction with TM3' (S204) in all mutant structures. However, the density for Y327 is not well resolved in chain A of M331K structure and hence was replaced with an alanine during model building (Fig 3.21A). In both chains K331 forms hydrogen bond with S98 as also seen in M331E structure. However, the density for lysine was poor, as it is long, flexible and exposed to the solvent. It is possible that the interaction between TM1' and TM6' observed in the crystal structures is responsible for the low uptake activity seen in M331E and M331K mutants.

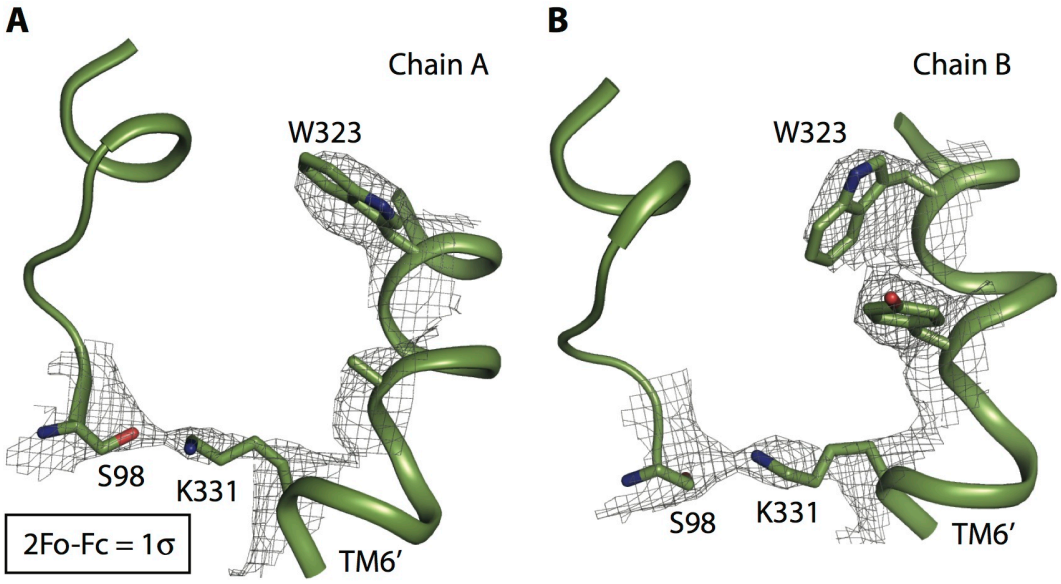

Figure 3.21 Central binding site of M331K mutant

(A) Electron densities contoured at 1σ are shown for selective residues from TM1' and TM6' of chain A. Density for Y327 is not well resolved (B) W323 is rotated by around 90° in chain B compared to chain A. A continuous network between S98 and K331 is observed in both chains, indicating hydrogen bonding between the two residues.

Table 3.4 Data collection and refinement statistics for M331 mutants

Data collection	M331E	M331K
Space group	R3:H	R3:H
Cell dimensions		
a, b, c (Å)	129.55 129.55 159.97	130.2 130.2 321.66
α, β, γ (°)	90, 90, 120	90, 90, 120
Resolution (Å)	24.56 (2.38-2.3)	46.16 (3.31 - 3.2)
Unique reflections	43988 (4434)	33256 (3347)
$I/\sigma I$	8.59 (1.76)	8.75 (1.20)
Completeness	98.96 (99.91)	99.15 (99.70)
Refinement		
Protein residues	510	1016
Number of atoms	4033	8017
Protein	4005	8017
Ligand	11	0
Water	17	0
R_{work}/R_{free} (%)	25.53/29.28	24.31/31.09
Ramachandran favoured (%)	89	76
Ramachandran outliers (%)	2.8	6.4
r.m.s.d. bonds (Å)	0.017	0.009

r.m.s.d angles (°)	1.58	1.4
Average B factors		
Protein	41.70	61.10
Solvent	37.90	NA

3.3 Alternating access in CaiT – towards crystallizing CaiT in an outward-open conformation

In order to understand how a transporter functions, it is crucial to capture the various conformational changes that it undergoes during a transport cycle. All the wild type (*E. coli* and *Proteus mirabilis*) and mutants forms of CaiT discussed so far have crystallized in an inward-open conformation. The presence (saturating amounts) or absence of a substrate during purification and crystallization did not affect the conformational state of the protein. Irrespective of the presence of a substrate, CaiT always crystallized in an inward-open state. Since this conformation seemed to be the low energy state of the transporter, it was imperative to force CaiT to crystallize in a different conformation, preferably outward-open, to understand the alternating access mechanism in this antiporter. Various approaches that were tried in this regard are discussed below.

3.3.1 Altering crystal contacts in CaiT: Structure of PmCaiT ΔN construct

In the crystal structure of wild type PmCaiT, the N-terminal region including a part of the His-tag of one monomer interacts with the periplasmic side of the neighboring monomer (Fig 3.23A). All the mutant and wild type crystal structures determined thus far showed similar crystal packing, raising a possibility that these crystal contacts favor the crystallization of the inward-open molecules. A truncated version of the protein missing the first eight residues (referred to as ΔN) was designed to alter the crystal contacts and to test if the protein still crystallizes in an inward-open conformation. The new construct was cloned into a pET15-b plasmid with Nde1-Xho1 restriction sites and transformed into BL21-pLysS cells for expression. A small-scale expression trial confirmed that the protein could be expressed in large

quantities similar to the wild type full-length protein (Fig 3.22). The protein was then purified in large scale using the same protocol as for the full-length CaiT. The protein obtained after Ni^{2+} affinity purification was passed through a PD-10 desalting column to remove imidazole before setting up crystallization plates.

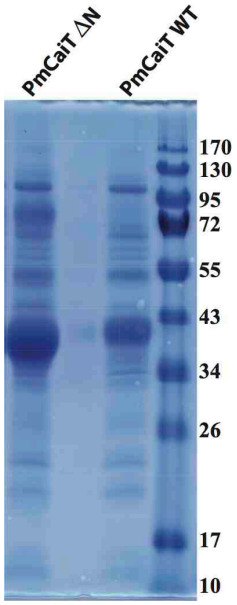

Figure 3.22 Small-scale expression test of PmCaiTΔN

Coomassie-stained SDS gel of PmCaiTΔN expressing bacterial membrane. For comparison, membranes of overexpressed PmCaiT wild type was also loaded. The PmCaiTΔN runs slightly faster than the wild type due to the deletion of eight residues from the N-terminus.

Assuming altered crystallization behavior from the wild type, extensive sparse matrix crystallization screening was performed with PmCaiTΔN. The protein crystallized in several new conditions. Out of 60 crystals measured at the Swiss Light Source, 9 crystals diffracted to a resolution better than 4.0Å. A crystal that was grown in 0.1M $LiSO_4$, 0.1 M glycine pH 9.3 and 30% PEG400 diffracted to a resolution of 3.3Å. Interestingly, PmCaiTΔN crystallized in the P63 space group, while PmCaiT wild type usually crystallizes in the H3 space group. The structure was solved by molecular replacement using PmCaiT wild type structure (PDB: 2WSW) as the search model. Iterative model building in COOT and refinement using Phenix were performed to complete the model (Table 3.5).

Table 3.5 Data collection and refinement statistics for PmCaiT ΔN

Data collection	**PmCaiT ΔN**
Space group	P63
Cell dimensions	
a, b, c (Å)	133.96 133.96 86.13
α, β, γ (°)	90, 90, 120
Unique reflections	12236 (1214)
Resolution (Å)	43.85 (3.52-3.4)
$I/\sigma I$	11.06 (2.62)
Completeness	99.97 (99.84)
Refinement	
Protein residues	495
Number of atoms	3914
Protein	3914
Ligand	0
Water	0
R_{work}/R_{free} (%)	20.26/26.48
Ramachandram favored (%)	84
Ramachandran outliers (%)	2.6
r.m.s.d. bonds (Å)	0.009
r.m.s.d angles (°)	1.32
Average B factors	
Protein	67.10
Solvent	NA

Though both the wild type and ΔN crystal of CaiT had one monomer per asymmetric unit, the unit cell parameters as well as the crystal packing of the ΔN structure were different from that of the wild type protein (Fig 3.23). In the wild type structure each CaiT molecule makes contacts with a neighboring molecule in the crystal both on the periplasmic and the cytoplasmic side (Fig 3.23 A). In addition to this, in the wild type structure, the N-terminus of the neighboring protomer forms extensive contacts with the groove in the periplasmic side (shown in red) and loops L4' and L8' from the central protomer packs against L3' and TM10' of the symmetry related protomer. However in ΔN structure each monomer makes crystal contacts with four monomers, each from a different trimer. Two of them are on the periplasmic side and two on the cytoplasmic side (Fig 3.23B). Residues from L8' and TM2' contact L9' and TM3' from the symmetry-related protomers.

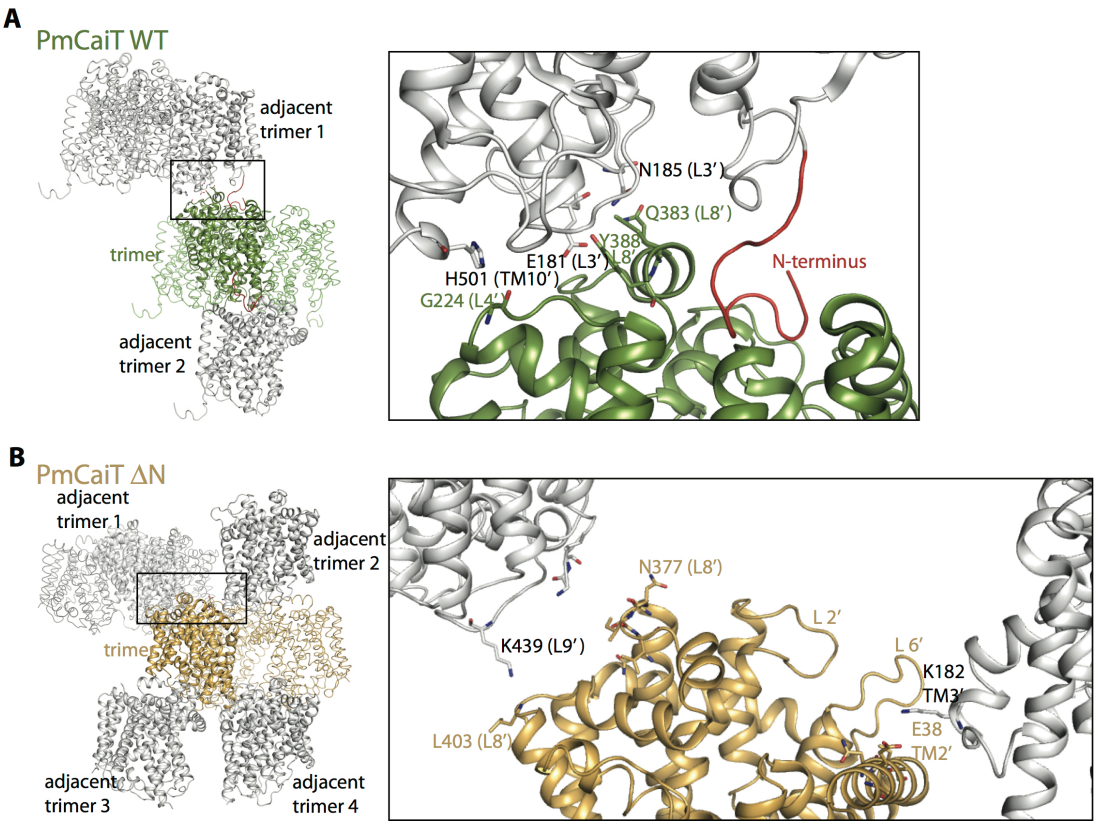

Figure 3.23 Comparison of crystal packing in PmCaiT wild type and ΔN structures

(A) The trimer in focus from PmCaiT wild type is shown in green while the repetitive units (adjacent trimer 1 and 2) are shown in grey. The complete trimer of adjacent trimer 1 is shown for reference while only the monomer from 'adjacent trimer 2' is shown for clarity. Each monomer of the central trimer (green) forms crystal contacts to one monomer each from adjacent trimer 1 and 2. (B) For the ΔN structure, the central trimer is shown in gold. The symmetry related trimers are shown in grey. The complete trimer of adjacent trimer 1 is shown for reference. Each monomer makes crystal contacts with four monomers all from different trimers (adjacent trimer 1, 2, 3 and 4). The insets show a detailed view of the residues involved in crystal packing. The major residues involved in crystal contacts are labeled. Molecules shown in ribbon illustrations (in green and gold color) are part of the biological trimer.

Despite having new unit cell parameters and different crystal contacts, the ΔN structure adopted an inward-open conformation similar to wild type. The ΔN monomer and the wild type structures superimpose with an overall rmsd of 0.45 and do not reveal any significant movement of helices (Fig 3.24). Two loop regions, L6' and L9' show an rmsd of 1Å when both structures are compared. L9' is involved in crystal contacts in the ΔN structure (Fig 3.24). Similar to the wild type structure, the

ΔN structure does not have any substrate-bound at the central or the external binding site.

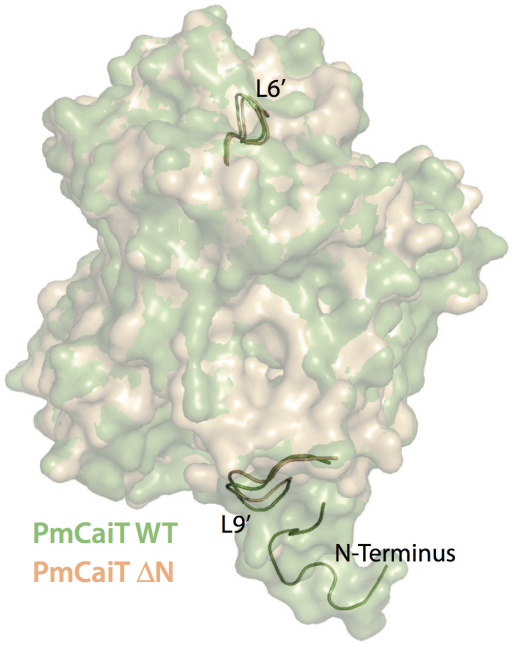

Figure 3.24 Superposition of PmCaiT wild type and PmCaiT ΔN

Wild type is shown in green and ΔN in orange. Only the regions (loops) that show an rmsd > 1Å are shown in cartoon representation. The rest of the structure is shown in transparent surface view.

3.3.2 Disrupting the hydrogen bond network around E111 – Structure of Y115Q

The strong hydrogen bond network centered around E111 (E111 site) that is on the periplasmic side of the protein, holds the helices of the bundle domain tightly together, especially TM1', TM2' and TM6' (Fig 3.25). It is possible that this strong hydrogen bond network helps to stabilize CaiT in the inward-open conformation. Mutating E111 to alanine was shown to make the protein unstable and the mutant runs as a monomer on a blue native gel (Schulze, 2011). The idea was to introduce mutations that would weaken the hydrogen bond network at the E111 site without making the transporter unstable. To achieve this, several of the hydrogen network residues at the E111 site were mutated mostly into comparable polar amino acids (Table 3.6).

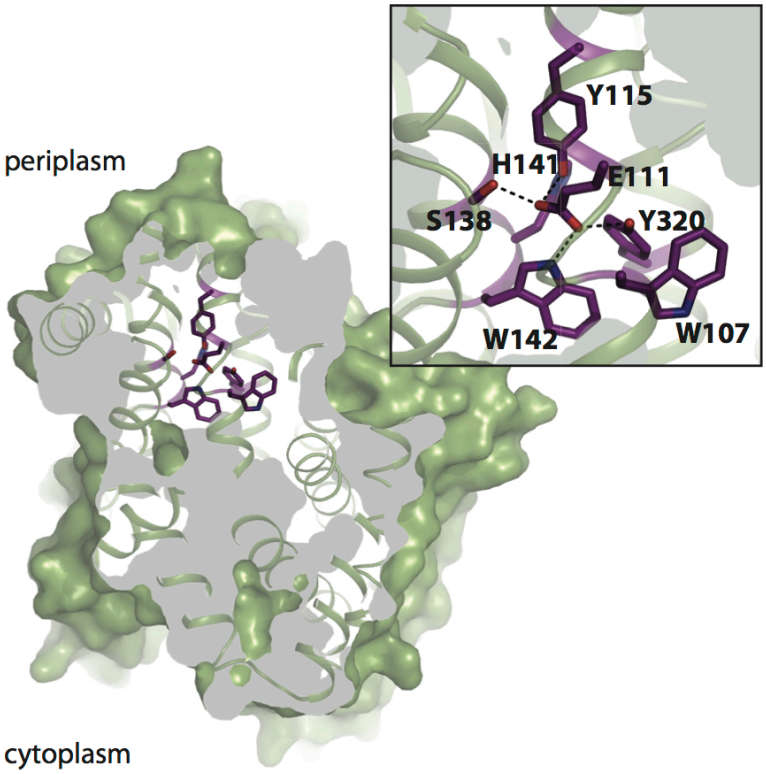

Figure 3.25 Hydrogen bond network around E111 in PmCaiT wild type structure

A slice through the PmCaiT wild type structure shows the hydrogen bond that holds together the bundle domain in the periplasmic side. The central binding site is open to the cytoplasm. Inset shows details of the hydrogen bond network centered on E111.

The mutants E111D, E111Q, Y115Q, Y320Q and H141N were purified similar to PmCaiT wild type (Table 3.6). E111D, H141N and Y320Q proved difficult to purify, probably because these mutations make CaiT unstable. On the other hand both E111Q and Y115Q could be purified and crystallized. However only the crystals of Y115Q diffracted to high resolution. The structure of the Y115Q mutant was determined at 2.45Å using molecular replacement with PmCaiT wild type as search model (Table 3.7).

Table 3.6 Mutants designed for the E111 site.

The table shows the outcome of purification and crystallization trials on the mutants generated around the E111 network.

Expression	Purification	Crystallization	Diffraction
E111D	✗	✗	✗
E111Q	✔	✔	✗
Y115Q	✔	✔	✔
H141N	✗	✗	✗
Y320Q	✗	✗	✗

Table 3.7 Data collection and refinement statistics for Y115Q

Data collection	**Y115Q**
Space group	R3:H
Cell dimensions	
a, b, c (Å)	130.95 130.95 158
α, β, γ (°)	90, 90, 120
Unique reflections	37111 (3705)
Resolution (Å)	46.06 (2.54-2.45)
$I/\sigma I$	11.78 (2.47)
Completeness	99.85 (99.25)
Refinement	
Protein residues	503
Number of atoms	3978
Protein	3977
Ligand	0
Water	1
R_{work}/R_{free} (%)	24.81/29.15
Ramachandran favored (%)	95
Ramachandran outliers (%)	0.2
r.m.s.d. bonds (Å)	0.009
r.m.s.d angles (°)	1.19
Average B-factors	
Protein	63.70
Solvent	45.40

The structure of PmCaiT Y115Q was very similar to the wild type structure with the central substrate-binding site accessible to the cytoplasm and with no major movement of helices. In contrast to the wild type structure where Y115 forms hydrogen bond with E111, Q115 in the mutant structure points away from the

hydrogen bond network around E111 (Fig 3.26). Interestingly, in the Y115Q mutant structure, a water molecule appears near E111 and participates in the hydrogen bond network at the E111 site. E111 maintains its interaction with W142, Y120 and S138 as in wild type. However the water molecule now takes over the role of Y115 and bridges the coordination between E111 and H141. Interestingly the sidechain of Y320 has moved by almost 2.3Å in Y115Q structure and is only involved in a weak interaction with E111 compared to the wild type structure (Fig 3.26).

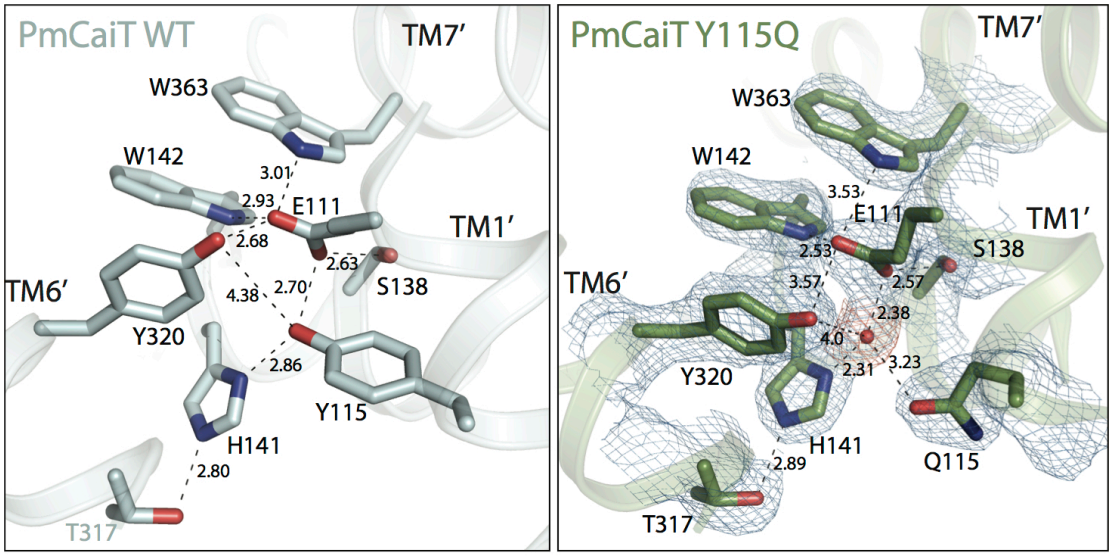

Figure 3.26 Comparison of PmCaiT wild type and Y115Q mutant structures

All the residues involved in hydrogen bond interactions in the wild type are involved in this network in the mutant structure as well. While Y115 coordinates E111, Q115 points away and forms a hydrogen bond with a water molecule. 2Fo-Fc map at 1.0σ with the densities of the sidechains involved are shown for Y115Q structure. The 2Fo-Fc map for the water molecule, shown in red for clarity, is contoured at 1.5σ.

In the Y115Q mutant structure, Y320 moves a bit closer to the water molecule and has a weakened interaction with E111 when compared to the wild type structure. This movement of Y320 (displacement of 2.6 Å and a rotation of 26°) is accompanied by a significant rotation (67°) of W107 sidechain form TM1'. Remarkably, the movement of Y320 and W107 results in the opening of a channel from the periplasm to the central binding site (Fig 3.27). However, the channel does not appear wide enough for the substrate to pass through.

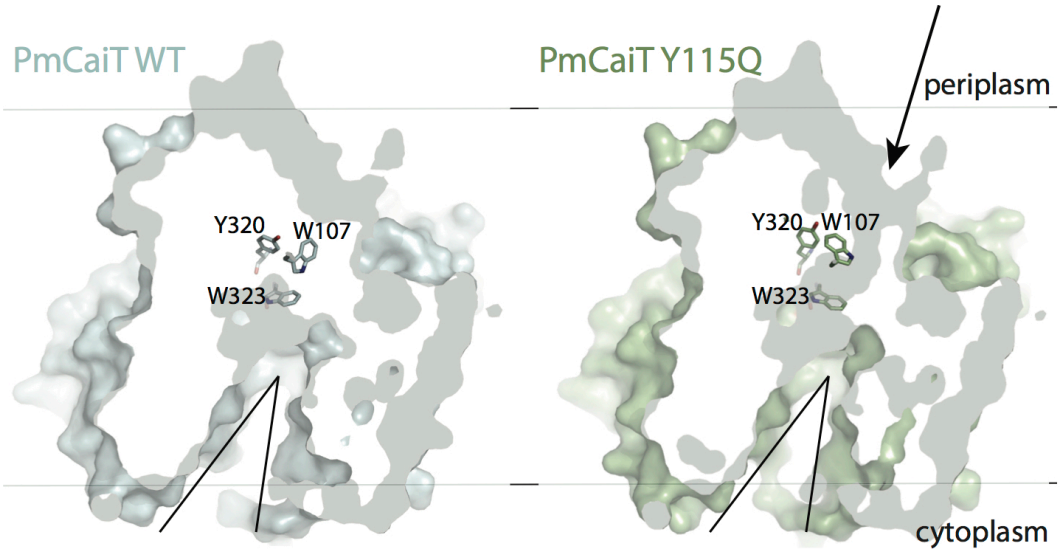

Figure 3.27 Opening of the periplasmic cavity in Y115Q crystal structure

(A) The wild type is open to the cytoplasm while W107 is seen to be blocking access to the central substrate-binding site from outside. (B) Rotation of the W107 sidechain opened the substrate-binding site to the periplasm as indicated by the arrow. The black lines show the accessibility of the central substrate-binding site to cytoplasm.

Perturbing the hydrogen bond network around E111 indeed led to an outside-open state with a continuous channel extending from the periplamic to the cytoplasmic side. Since the substrate seems to be accessible from both cytoplasm and periplasm, it remains to be seen if this signifies a bona fide transition state of the transporter or an artifact forced by the mutation. Interestingly, Y157, the equivalent residue in BetP remains unchanged in both inward-open and outward-open crystal structures. Transport activity assays with Y115Q reconstituted into liposomes could show if the transporter is functional or locked in a conformation that is seen in the crystal structure.

3.3.3 Weakening Na2 site - Crystal structure of T100A/T421A

The transition of a LeuT fold transporter from outward to inward-open state is triggered by the hydration of the Na2 site followed by Na2 release. Extrapolating the principles of this mechanism, the Na2 site was weakened to favor successful

crystallization of LeuT, in an inward-open state (Krishnamurthy & Gouaux, 2012). Applying a similar strategy for CaiT, the hydrogen-bonding network around R262, the equivalent of Na2 in LeuT and BetP, was modified. The residues coordinating R262 in the crystal structure, T100A from TM1' and T421A from TM8' in the inward-open state, were mutated. These mutations in the Na2 site could favor a different orientation of R262 as predicted by our modeling studies (Fig 3.14). This could result in the shift of conformational equilibrium of CaiT towards the outward-open state.

A double mutant T100A/T421A made in the ΔN PmCaiT background (because of its better expression) was purified. Out of the several crystallization conditions screened, the best crystal that diffracted to a resolution of 2.75 Å was crystallized in 23% PEG-400, 100mM $CaAc_2$ and 100mM HEPES at pH 7.0. Two datasets from a single crystal were scaled together for better data quality and completeness. The mutant crystals belonged to the P63 space group similar to wild type ΔN (Table 3.8).

Table 3.8 Data collection and refinement statistics PmCaiT ΔN T100A/T421A

Data collection	**T100A/T421A**
Space group	P63
Cell dimensions	
a, b, c (Å)	134.855 134.855 87.282
α, β, γ (°)	90 90 120
Unique reflections	22382 (2204)
Resolution (Å)	44.14 (2.9 – 2.8)
$I/\sigma I$	23.71 (1.99)
Completeness	99.90 (99.06)
Refinement	
Protein residues	496
Number of atoms	3906
Protein	3905
Ligand	0
Water	1
R_{work}/R_{free} (%)	21.88/26.00
Ramachandran favored (%)	90
Ramachandran outliers (%)	1.6
r.m.s.d. bonds (Å)	0.009
r.m.s.d angles (°)	1.21
Average B-factors	
Protein	70.60
Solvent	45.70

The structure was in an inward-open conformation with no major differences in comparison to wild type ΔN. Interestingly, TM5' harboring R262, had moved by almost 2Å, further opening the cytoplasmic pathway (Fig 3.28). It would be interesting to see whether the wild type CaiT undergoes this movement of TM5' using Electron Paramagnetic Resonance (EPR) spectroscopy.

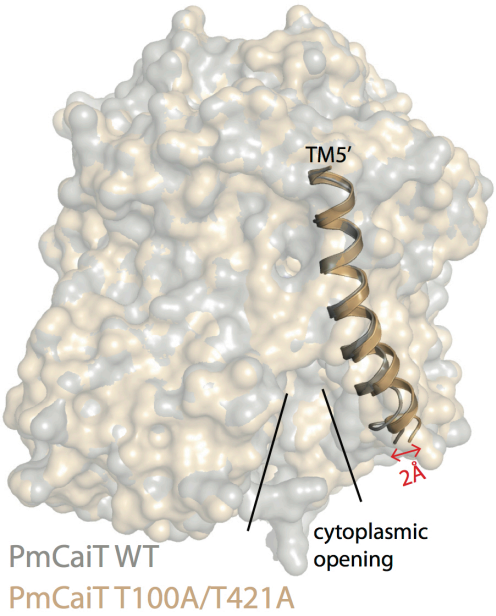

Figure 3.28 Superimposition of PmCaiT wild type and T100A/T421A structures

The overall rmsd of both structures is around 0.45Å. The major difference between the two structures is the movement of TM5' harboring R262 by approximately 2Å. This movement further widens the cytoplasmic pathway. Rest of the protein is shown in surface view.

In contrast to the wildype structure, where several neighboring residues tightly coordinate R262 (average B-factor of 74.37 for R262 sidechain), it was more flexible (average B-factor 96) in the T100A/T421A structure and had less resolved electron density. In this structure, R262 forms a hydrogen bond with the backbone carbonyl of A100 from the unwound stretch in TM1' (Fig 3.29). The loss of the strong R262 hydrogen bond network thus makes TM5' more detached from the rest of the protein, resulting in its movement away from the protein core, leading to a further opening of the cytoplasmic cavity.

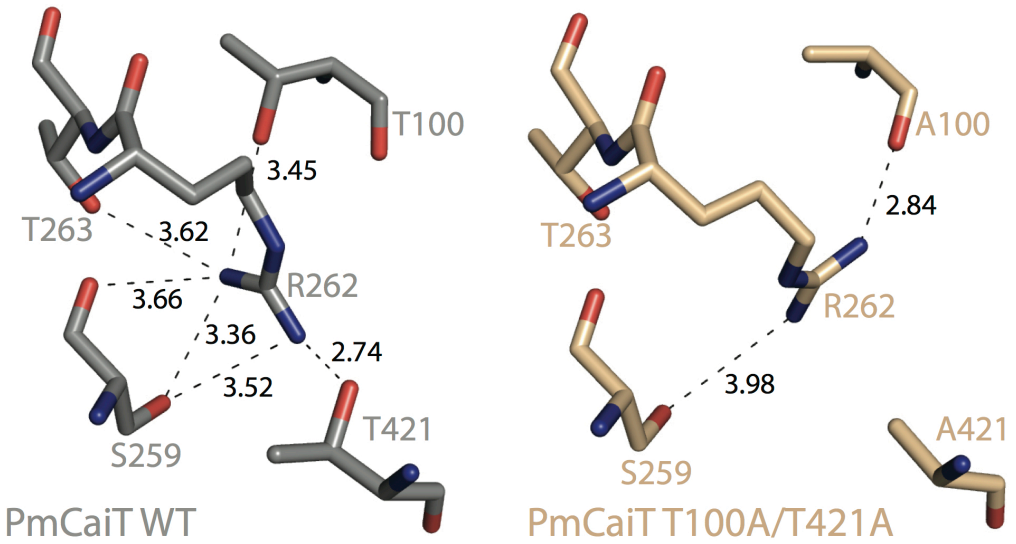

Figure 3.29 Comparison of R262 coordination network in PmCaiT wild type and T100A/T421A structure

While R262 in wild type interacts with several amino acids, the interaction site is quite weakened in T100A/T421A mutant. R262 sidechain in the mutant structure is quite flexible with less resolved density.

4 Discussion

4.1 Second-substrate binding site

A characteristic feature in CaiT is the presence of a second substrate-binding site on the periplasmic side (Schulze *et al*, 2010). Such a binding site has also been predicted for LeuT and since then has been highly debated (Shi *et al*, 2008) (Piscitelli *et al*, 2010) (Zhao *et al*, 2011) (Quick *et al*, 2012). It was proposed that the two substrate-binding sites in CaiT interact allosterically. According to the proposed allosteric model, binding of substrate to the periplasmic site favors substrate binding at the central binding site (Schulze *et al*, 2010). This allosteric behaviour is conferred through a series of small helix movements that propagate from the periplasmic site to the central substrate-binding site that triggers the rotation of the W323 sidechain, allowing the substrate to bind (Schulze *et al*, 2010). Interestingly, this putative periplasmic binding site was empty in all the CaiT structures obtained in this study. There were structures with a substrate-bound at the CBS but with W323 adopting the same conformation as seen for apo PmCaiT (Fig 1.40). It appears from these structures that the substrate occupancy at the periplasmic site is not an absolute requirement to enable substrate binding at the CBS. This observation however does not rule out the possibility of the presence of a periplasmic substrate-binding site or its effect on the transport kinetics in CaiT.

4.2 Lessons from the new crystal structures of CaiT

The mutants of CaiT were designed to destabilize the inward-open state in an attempt to crystallize the outward-facing state in CaiT. Although some transporters readily adopt various conformations in crystals (as seen for BetP), new conformational states have been triggered or forced in the case of transporters like LeuT (to obtain an inward-open state) (Krishnamurthy & Gouaux, 2012) and GltPh (inward-open state) (Reyes *et al*, 2009). Although substrates/ inhibitors are known to

shift the population of transporters from one conformation to another (Klingenberg & Martonosi, 1976), such inhibitors are not known for transporters of the BCCT family. Moreover, substrate-binding in CaiT does not seem to influence a shift in conformational states (Schulze *et al*, 2010).

Interestingly, the various crystal structures of CaiT mutants along with the wild type structures display a gallery of conformational states manifesting changes at the central binding site (Fig 4.1). This mainly included various orientations of the W323 sidechain and the substrate. The interesting features observed from these structures and their probable implications are summarized below

4.2.1 Y115

The Y115Q mutation was designed to destabilize the coordination network that plays a crucial role in holding together the helices TM1', TM2', TM6' and TM7' in the periplasmic side of the protein. Weakening this coordination network was expected to facilitate the stabilization of the outward-open state in CaiT. Introducing the Y115Q mutation altered the strong hydrogen bond network around E111 slightly, which led to the rotation of the sidechains of W107 and Y320. This gating movement led to an opening of a narrow pathway from the periplasm to the central binding site. However, the central binding site remained fully solvent accessible from the cytoplasm, making the occurrence of such a conformation *in vivo* questionable. In summary, PmCaiT Y115Q structure shows a different conformational state from the wild type structures. Whether this is the snapshot of a natural occurring state of the transporter or a direct effect of the introduced mutation can only be answered by further studies including uptake assays of the mutant.

4.2.2 T100A/T421A double mutant

Crystal structures in various conformations of symporters from LeuT and BetP, have helped us to understand how these transporters cycle through various conformations during a substrate transport cycle. Briefly, a transporter is loaded with two sodium ions and a substrate molecule from the periplasmic side. This is followed by the outward to inward-state transition, triggered by the hydration of the Na2 site. This leads to Na2 release followed by the release of the second sodium ion (Na1) and the substrate from the central binding site to the cytoplasm (Krishnamurthy & Gouaux, 2012) (Perez *et al*, 2012).

The T100A/T421A double mutation was designed in an attempt to weaken the Arg262 hydrogen-bonding network. A similar strategy of weakening the Na2 site was previously adopted in LeuT to affect the conformational equilibrium leading to the crystallization of an inward-open state. In the PmCaiT T100AT421A double mutant structure, a slight movement of TM5' was observed, leading to a wider cytoplasmic cavity. It is possible that introducing more stabilizing hydrogen bond interactions around R262 to facilitate the orientation of R262 in the outward-facing state as seen in the model (Fig 3.14) could lead to a different conformational state.

4.2.3 Rb^+ and Tl^+ bound R262 mutants

In the Rb^+ bound and Tl^+ bound CaiT structures, the central substrate-binding site is occupied by these ions, through favorable cation-π interactions between the tryptophan box and the ions themselves. Interestingly, the orientation of the sidechain of W323 is different in the Rb^+ and Tl^+ bound structures (Fig 4.1). This indicates that W323 movement may occur irrespective of the binding of L-carnitine or γ-butyrobetaine at the CBS.

4.2.4 M331E and M331K

The M331E structure has two interesting features. Firstly, a L-carnitine molecule is bound at the central substrate-binding site, making it the only L-carnitine-bound PmCaiT structure. The hydroxyl group of L-carnitine however does not interact with any residue in the protein, neither through backbone nor through sidechain groups. Moreover, the substrate is bound in a novel orientation, making cation-π interactions with tryptophans 142, 147 and 324 instead of W323 as seen in other structures. Both M331E and M331K structures have a common feature: the lysine or glutamate at position 331 forms hydrogen bond interactions with S98 from TM1' (Fig 4.1). The low uptake activity of these two mutant transporters might be arising from this strong interaction.

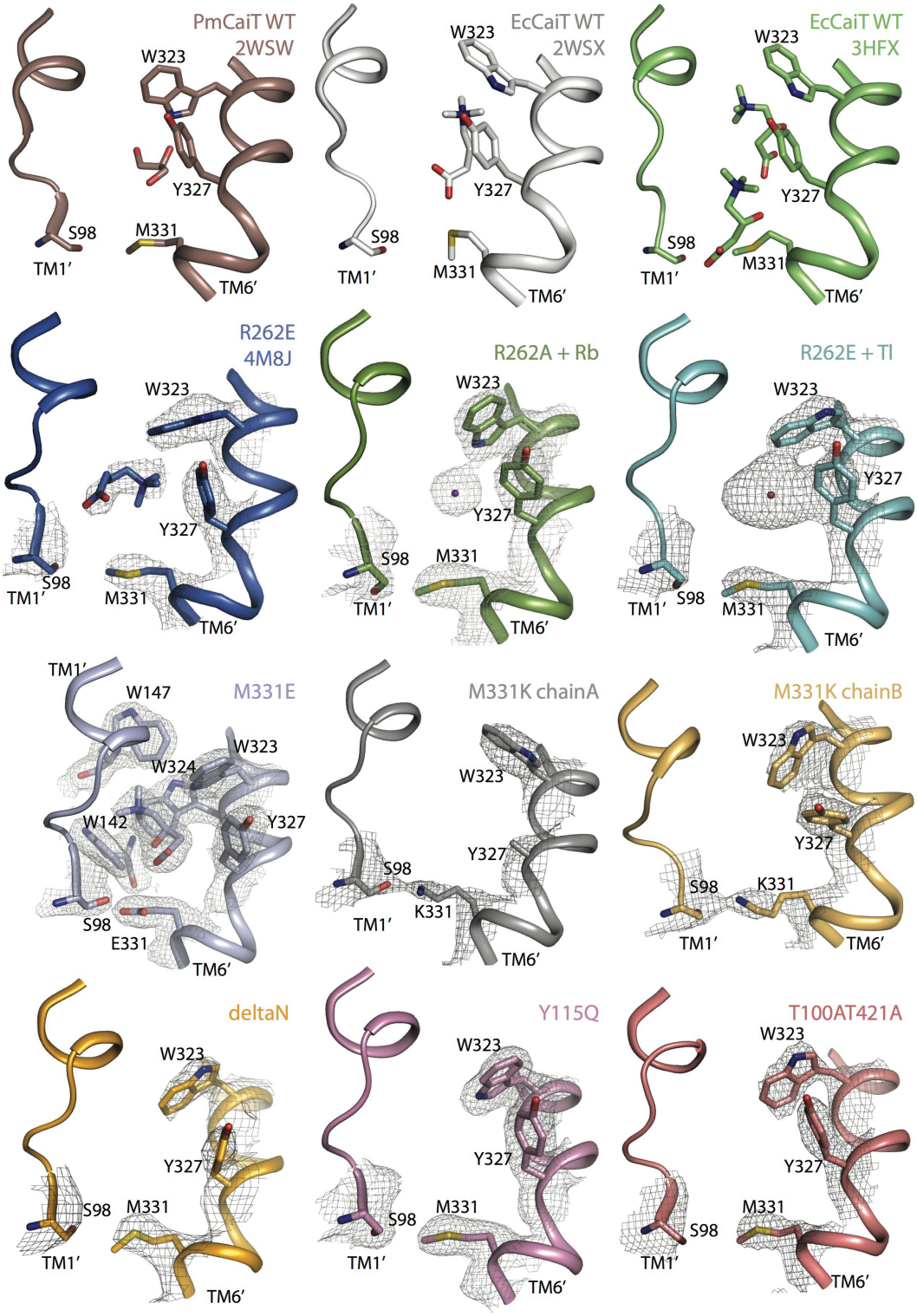

Figure 4.1 The central substrate-binding site of PmCaiT and EcCaiT wild type and the CaiT mutants designed and crystallized in this thesis

Only residues involved in major movements are shown. The 2Fo-Fc density is contoured to a s level of 1.0.

These structures provide us with snapshots of the conformational dynamics occurring at the central substrate-binding site. W323 is highly flexible and the rotamer it adopts could further influence the binding or release of substrate at the central substrate-binding site. However to understand how substrate binding drives conformational change demands a structure of CaiT in other conformations.

4.3 Altering the Electrostatic Component in CaiT- R262 mutants

A second aspect of this research was to investigate the pivot point in the transition of CaiT from outward-open to inward-open state or *vice versa*. The Na2 site is known to be structurally and functionally important in the Na^+-dependent transporters LeuT and BetP to trigger this transition (Yamashita *et al*, 2005; Perez *et al*, 2012). The Na^+-dependent nature of the CaiT mutants R262A and R262E suggests the necessity of a positive charge at the Na2 site for substrate binding and transport. However, structures of the R262 mutants with an ion (Thallium or Rubidium) bound at the Na2 site could not be obtained, probably because Rb^+ and Tl^+ did not fit into the Na2 site, or the central Trp box had higher affinity for them. It is also possible that the inward-open conformation, which is a sodium-releasing state (Krishnamurthy & Gouaux, 2012; Perez *et al*, 2012; Shimamura *et al*, 2010) (Li & Tajkhorshid, 2009), might preclude ion binding at the Na2 site. This is also evident from the inward-open crystal structures of vSGLT, MhP1, LeuT, and BetP, where the Na2 site is empty (Watanabe *et al*, 2010) (Krishnamurthy & Gouaux, 2012; Perez *et al*, 2012; Shimamura *et al*, 2010).

Interestingly, a direct correlation between the electrostatic interactions of an amino acid sidechain and ion-dependence or independence of transport has been observed in the GABA (γ-aminobutyric acid) transporter GAT-1 as well as in LeuT and Tyt1 (Zomot *et al*, 2007). Although the eukaryotic neurotransmitter:sodium symporters including GAT-1 are chloride-dependent, their bacterial counterparts LeuT, Tyt1, and TnaT are chloride-independent. Introduction of a glutamate near the putative Na1 binding site in GAT-1 renders this transporter chloride-independent, whereas the

reciprocal mutations make LeuT and Tyt1 chloride-dependent (Zomot *et al*, 2007; Zhao *et al*, 2009; Kantcheva *et al*, 2013). Similarly, replacement of an aspartate by threonine transformed the light-driven proton pump bacteriorhodopsin into a chloride pump (Sasaki *et al*, 1995). Thus, it could be shown that the electrostatic charge in the Na2 site of a LeuT-type transporter can be changed from that of a positively charged amino acid sidechain to a sodium ion. In contrast, mutating M331 that substitutes for the sodium ion in the Na1 site does not make CaiT Na^+-dependent (Schulze *et al*, 2010).

It can be speculated that CaiT may have evolved into a Na^+- independent transporter from an ancestral Na^+-dependent transporter. A positively charged sidechain in the Na2 site would have been an advantage in making CaiT independent of a second substrate such as Na^+ or H^+. Sodium independence makes sense for the biological role of CaiT, which is to carry out substrate/ product antiport of L-carnitine and γ-butyrobetaine down their concentration gradients (Jung, 2002). Therefore, an additional dependence on a Na^+ gradient would be unnecessarily restrictive without offering a selective advantage. In contrast, this dependence would be a selective disadvantage, as a Na^+ gradient sufficient to drive transport would not normally be available in the intestinal tract, which is the natural habitat of both *E. coli* and *P. mirabilis*.

4.3.1 Implications for the Transport Mechanism

The predicted high pKa of the R262 sidechain suggested that its amino group is not deprotonated during the outward-open to inward-open transition of the transporter. Moreover, our transport assays confirm a previous report that CaiT is not H^+-dependent (Fig 3.1). It was therefore interesting to see whether there is a mechanism in CaiT that mimics the process of Na^+-binding and unbinding that would induce conformational changes through the unwound part of TM1'. The changing hydrogen bond network centered on R262 in the inward-open crystal structure and in our models of the closed and outward-open states suggest an oscillatory

movement of the arginine sidechain (Fig 3.14). We propose that this oscillating mechanism simulates Na^+ binding and unbinding during the transport cycle, thus triggering substrate release, as in LeuT (Krishnamurthy & Gouaux, 2012) (Caplan *et al*, 2008), vSGLT (Watanabe *et al*, 2010), and BetP (Perez *et al*, 2012) (Fig 4.2). Functionally, CaiT does not depend on an ion gradient, as it is involved in L-carnitine/γ-butyrobetaine transport and caters to the cells' need for L-carnitine during anaerobic growth or nutrient starvation. There is a further advantage in a tethered positive charge replacing the functionally equivalent, but more mobile, Na2: Unlike BetP or LeuT, which are symporters, CaiT is an antiporter, and as such can switch between different conformational states only in the substrate-bound form, whereas in symporters, the inside-open to outside-open transition has to take place in the absence of either substrate or Na^+. The energy barrier for these transitions in CaiT is likely to be similar in both directions, as they are both substrate-mediated. This would call for a symmetrical event such as R262 oscillation to control the flexibility of the unwound part of TM1' in both transport directions, in contrast to the Na^+-dependent symporters, where Na^+-mediated conformational changes occur only during the outward-open to inward-open transition.

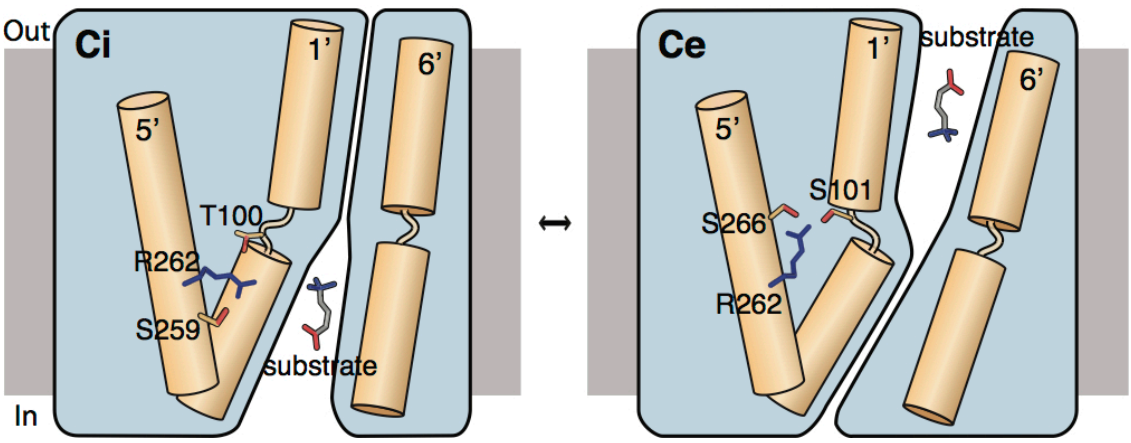

Figure 4.2 Schematic representation of the arginine oscillation model as a mechanism of substrate transport in CaiT

In the inward-open conformation (Ci), R262 interacts with T100 from the unwound part of TM1', as well as with S259 from TM5'. Binding of substrate near the partly unwound TM1' of

> CaiT triggers reorientation of R262, which now coordinates with S101 from TM1' and S266 from TM5'. This is accompanied by the flexing of TM1' and coordinated movements of nearby helices, ultimately resulting in the closing of the cytoplasmic pathway and substrate release into the periplasm (Ce) (Kalayil et al, 2013).

Substrate-induced alternating access for antiporters such as GlpT (Huang *et al*, 2003) or AdiC (Kowalczyk *et al*, 2011) is proposed to be mediated either by a single substrate-binding site or two different sites, respectively. In CaiT, substrate binding is likely to trigger the conformational change by interacting with the unwound region of TM1'. This would affect the hydrogen bond donors available to R262, which in turn would respond by reorienting itself accordingly. This oscillation of R262 is accompanied by the flexing of the unwound part of TM1', as well as the movement of the surrounding TM helices, thus opening and closing the cytoplasmic pathway (Fig 4.2).

In our R262 mutants, the arginine-mediated, substrate-induced conformational changes fail to take place, even though the substrate can bind, albeit with lower affinity (Fig 3.10). This explains the stabilization of a differently oriented substrate in our crystal structure of PmCaiT R262E, a likely intermediate step in the transport cycle, where the carboxyl group of the substrates interacts with the partly unwound TM1' helix (Fig 3.11).

In summary, our biochemical and structural characterization of CaiT and the role of R262 in its transport mechanism illustrates how CaiT evolved to be ion-independent, whereas the mode of conformational changes remains largely conserved across the large APC transporter family. Our results demonstrate that a positively charged amino acid can assume the functional role of the sodium ion in the alternating access transport mechanism. Similar alternating conformations of a charged amino acid sidechain simulating ion binding or dissociation could be operative in other ion-independent transporters.

Chapter II

Expression and purification of the human mitochondrial calcium uniporter

5 Introduction

5.1 Calcium as a second messenger

Second messengers are molecules that relay signals received on cell surface receptors to target molecules within the cell. The calcium ion (Ca^{2+}) is the most versatile and most widely used second messenger as it is involved in the regulation of almost all known cellular functions and reactions (Petersen *et al*, 2005). The first observation that calcium ions could control a physiological event dates back to 1883 when Sydney Ringer added Ca^{2+} to the perfusion buffer of isolated heart cells triggering their contraction (Ringer, 1882a; 1882b; 1883a; 1883b).

The cytosolic concentration of Ca^{2+} is maintained around 100 nM at resting conditions in comparison to 2 mM in the extracellular space (Clapham, 1995). By maintaining a gradient of ~ 10^4 fold across the cell membrane, cells are sensitive to any increase in the cytosolic calcium concentration.

An increase in $[Ca^{2+}]_c$ levels is known to regulate several biological processes including

- Muscle contraction
- Exocytosis
    - Neurotransmitter release at the synapse
    - Hormone secretion (e.g. insulin)
- Activation of T cells and B cells
- Adhesion of cells to the extracellular matrix
- Apoptosis

Unlike other second messengers, prolonged high intracellular calcium levels ($[Ca^{2+}]_c$) can lead to cell death. Since Ca^{2+} cannot be metabolized, cells have developed

numerous binding and transport proteins to tightly regulate the intracellular concentration of calcium. Calmodulin (CaM) is one such binding protein that modulates the levels of intracellular Ca^{2+} levels and is involved in stimulating various signal transduction pathways (Clapham, 2007). In addition to various effector proteins that enable the multitude of downstream Ca^{2+} signaling pathways, Ca^{2+} signals within the cell are spatio-temporally regulated. Several channels and transporters tightly regulate the entry and exit of Ca^{2+} in the cells. These include voltage gated ion channels, Na^{+}/Ca^{2+} exchangers (NCX), ligand-gated channels and the G-protein coupled receptors (GPCRs). In addition there are adenosine tri-phosphate (ATP)-driven pumps like Ca^{2+}-ATPases on the plasma membrane and the ER (Fig 5.1). Organelles like the endoplasmic reticulum (ER), or the sarcoplasmic reticulum (SR) in skeletal muscle function as intracellular reservoir of Ca^{2+}. In addition to the ER or SR, mitochondria are known to act as Ca^{2+} sinks when there is a surge in Ca^{2+} concentration in response to a stimulus.

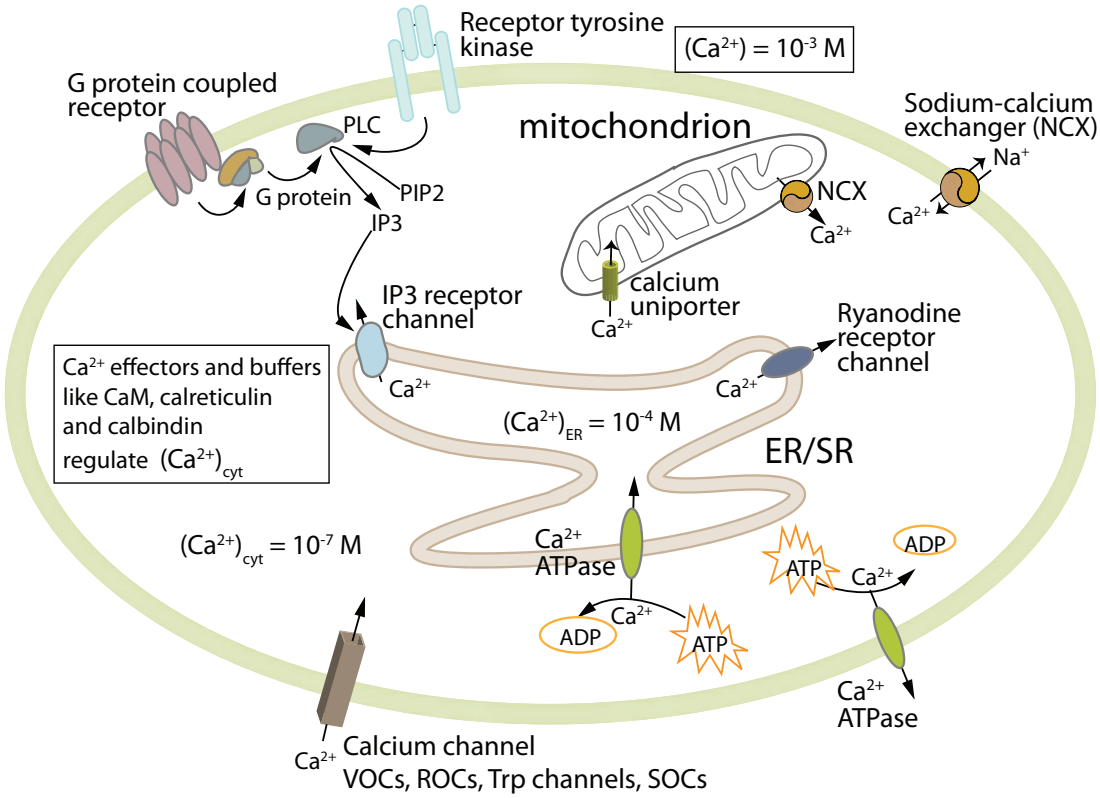

Figure 5.1 Schematic representation of intracellular Ca^{2+} signaling

Ca^{2+} entry into cells can occur through various Ca^{2+} channels like voltage-operated channels

(VOC), receptor-operated channels (ROC), transient receptor potential (Trp) channels, store-operated channels (SOC) etc. The trigger for channel activation varies for each channel and these signals include: binding of an agonist on a GPCR and subsequent release of second messengers, membrane depolarization, depletion of intracellular stores, direct binding of a neurotransmitter or a hormone agonist on ROCs etc. Certain second messengers like inositol 1,4,5-trisphosphate (IP_3) triggers the release of calcium from intracellular stores like the endoplasmic reticulum (ER) through IP_3 receptor channels (IP_3R). The Ca^{2+} pool in the cell is also regulated by Ca^{2+} flowing in and out through the Ca^{2+} -ATPases in PM and ER, Na^{+}-Ca^{2+} exchangers, the Ryanodine receptor channel in ER, or the Ca^{2+} uniporter in mitochondria. Various effectors, buffers and enzymes, bind the Ca^{2+} in the cytosol, thus determining the cellular effect of Ca^{2+} release.

5.2 Role of Calcium in mitochondrial function

Mitochondrial calcium $[Ca^{2+}]_{mt}$ is known to play several important roles for the functioning and survival of the cell. One of the most important effects of mitochondrial calcium accumulation is to regulate ATP production inside the mitochondria. Mitochondrial calcium activates three matrix dehydrogenases, namely pyruvate dehydrogenase (PDH), α-ketoglutarate dehydrogenase (α-KGDH) and isocitrate dehydrogenase (IDH) involved in the tricarboxylic acid (TCA) cycle which is a key part of aerobic respiration (McCormack *et al*, 1990). This activation causes an increase in the activity of the electron transport chain, thereby enhancing ATP synthesis (Jouaville *et al*, 1999). Studies have shown that the most effective signal for the stimulation of cellular respiration is high frequency calcium oscillations occurring in the cytosol and the mitochondrial matrix (Hajnóczky *et al*, 1995). Increasing levels of $[Ca^{2+}]_{mt}$ is also known to impact cell survival. Ca^{2+} overload of mitochondria triggers opening of a high conductance inner mitochondrial membrane channel called the permeability transition pore (PTP). This leads to a rapid collapse in membrane potential and leakage of proapoptotic components from the mitochondrial matrix into the cytoplasm and finally to necrosis or apoptosis (Rizzuto *et al*, 2012). On the other hand, reduced Ca^{2+} levels negatively regulate the TCA cycle, thus activating AMP activated protein kinase (AMPK) and hence autophagy.

5.3 Mitochondria and Calcium uptake – a brief history of the last 50 years

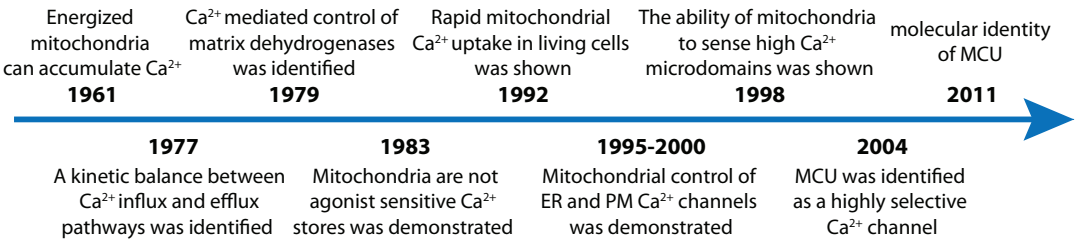

Figure 5.2 Timeline of mitochondrial Ca^{2+} research

ER – Endoplasmic Reticulum, PM - Plasma Membrane, MCU – Mitochondrial Calcium Uniporter. Adapted from (Rizzuto *et al*, 2012).

Several studies in the 1950s have shown that mitochondria, in the presence of calcium, undergo swelling. Since the chemiosmotic theory had not yet been proposed, mitochondrial swelling was attributed to other, incorrect reasons (Carafoli, 2012). Although a study in 1953 made a direct measurement of uptake of Ca^{2+} by heart mitochondria, this was considered an artifact since the low temperature used in this experiment would preclude the possibility of any metabolic activity (SLATER & CLELAND, 1953). It was only well after a decade that mitochondria were first associated with calcium uptake. Isolated rat kidney mitochondria were used to monitor the rapid uptake of large quantities of calcium (Ca^{45} isotope) in respiring mitochondria (Vasington & Murphy, 1961) (H F DeLuca, 1961). It was observed that this uptake is dependent on the presence of ATP, Mg^{2+} and an oxidizable substrate.

Subsequently, it was shown that Ca^{2+} uptake could be driven by imposing a H^+ or K^+ gradient across the mitochondrial membrane, thus proving the electrogenic nature of Ca^{2+} influx (Selwyn *et al*, 1970; SCARPA & Azzone, 1970). This finding could explain calcium uptake simply based on the chemiosmotic theory (MITCHELL, 1966), which was proposed a few years after the discovery of calcium uptake by mitochondria. The chemiosmotic theory ruled out the prevailing concept that a high-energy intermediate is involved in calcium uptake. Although the primary function of

mitochondrial calcium uptake was thought to be in regulating cytosolic calcium levels, in 1972 it was observed that mitochondrial calcium increased the activity of several matrix dehydrogenases involved in the citric acid cycle (Denton *et al*, 1972; McCormack *et al*, 1990). This meant that by activating these enzymes, calcium could in turn effect the ATP production in the mitochondrial matrix.

The basic properties of the calcium uptake system, for example the affinity of mitochondria for calcium, were the subject of many studies that ensued. These studies uncovered a major gap in the hypothesis that the mitochondrial calcium uptake plays a role in regulating the intracellular calcium levels. It was observed that the half maximal rate of calcium uptake by the hypothetical uniporter in the inner mitochondrial membrane was in the micromolar range (SCARPA & P, 1973). This observation together with the known $[Ca^{2+}]_c$ of 100 nM questioned the essential role of mitochondria in the regulation of cytoplasmic Ca^{2+} levels. Consequently, the focus shifted to the ER, which was emerging to be more important for Ca^{2+} regulation.

Rizzuto *et al.* addressed these questions in a landmark article in 1993 (RIZZUTO *et al*, 1993). By using recombinant aequorin (a calcium sensitive photoprotein) targeted to the mitochondria (RIZZUTO *et al*, 1992), the variations in the calcium levels in the mitochondrial matrix ($[Ca^{2+}]_{mt}$) of intact cells could be measured. They observed a sharp increase in $[Ca^{2+}]_{mt}$ in the presence of an agonist such as histamine that is known to mobilize Ca^{2+} from the intracellular stores through IP3 channels. This rapid uptake of cellular mitochondria contradicted previous observations of slow uptake by isolated mitochondria surrounded by submicromolar calcium concentrations (Pietrobon *et al*, 1990) (McCormack *et al*, 1990). The increase observed in mitochondrial calcium was much more rapid and of higher amplitude in comparison to exposing the whole cell to a defined calcium influx. This led to the hypothesis that the rapid calcium uptake system of the mitochondria is sensitive to the origin of increase of cytosolic Ca^{2+} (whether triggered by the calcium release from the intracellular stores or by an influx across plasma membrane) rather than responding to the average intracellular calcium levels. The existence of microdomains of high calcium concentrations between the closely spaced IP3 channels on the ER and

mitochondria could explain the rapid calcium uptake by the mitochondria. Thus the low affinity uptake system in mitochondria could respond to the fluctuating $[Ca^{2+}]_c$ via these high Ca^{2+} concentration clusters around mitochondria. Even though there is a rapid uptake of Ca^{2+} by mitochondria, the rapid dissipation of cytosolic calcium prevents excessive Ca^{2+} accumulation by mitochondria and hence mitochondrial damage.

5.4 Initial characterization of the mitochondrial calcium uniporter, MCU

Although calcium currents had been previously measured with isolated mitochondria, it was important to do the measurements with accurate control of the ion concentrations and voltage gradients across the membrane. This could be achieved by measuring calcium currents from single isolated mitoplasts (mitochondria lacking outer membrane) from COS-7 cells (Kirichok *et al*, 2004). Single-channel recordings on mitoplasts were performed by the patch clamp technique. This led to the observation that there is an inward-rectifying current or I_{MiCa} (mitochondrial calcium current) across the inner membrane in the presence of a potential difference ranging from -160 mV to +80 mV. This current was sensitive to ruthenium 360 (IC_{50} = 2nM) as well as to ruthenium red (IC_{50} = 9nM) and highly selective for calcium in comparison to monovalent cations. However, in the absence of divalent cations, MCU could conduct a Na^+ current, which in turn could be completely abolished in the presence of 100 nM Ca^{2+}. This affinity ensures high Ca^{2+} specificity despite relatively low cytoplasmic Ca^{2+} concentrations.

The mitochondrial calcium uniporter or MCU was seen to produce large currents, comparable to voltage-gated calcium channels. However, while the latter need millimolar calcium concentrations, MCU can achieve similar currents at micromolar cytosolic calcium concentrations. This could be explained by the large electrochemical gradient that exists across the inner membrane of an energized

mitochondrion and the very high open probability of MCU (99% open probability at a membrane potential of -200 mV) (Kirichok *et al*, 2004).

5.5 Molecular identification and characterization of MCU

Almost four decades after its discovery, two studies, using independent approaches, simultaneously identified MCU (formerly annotated as CCDC109A) as the Ca^{2+}-conducting pore of the mitochondrial inner membrane (Baughman *et al*, 2011) (De Stefani *et al*, 2011). Knowledge gathered from prior studies, the most important being the identification of MICU1 (mitochondrial calcium uptake 1) as a component of the mitochondrial uniporter uptake system (Perocchi *et al*, 2010) contributed to identifying this elusive uniporter. One study mainly used co-evolution and co-expression profiles of the candidate genes with MICU1 to successfully identify MCU (Baughman *et al*, 2011). The second study used a bioinformatics approach where known facts on MCU (for e.g. Absence of MCU in Saccharomyces cerevisiae but not in trypanosomes) were used to narrow down MCU from a database of potential mitochondrial membrane proteins called MitoCarta (De Stefani *et al*, 2011). The findings of both studies were mostly in agreement with each other. This discovery rekindled the research on mitochondrial calcium uptake and many researchers have since then flocked to explore the MCU protein.

HeLa cells (both intact and permeabilized) with MCU expression knocked down showed attenuated mitochondrial Ca^{2+} uptake, which could in turn be rescued by expressing the full length MCU cDNA (Baughman *et al*, 2011). MCU silencing did not affect the mitochondrial membrane potential (ϕ_m), basal and uncoupled respiration and the mitochondrial morphology, although Ca^{2+} activation of the TCA cycle was attenuated. Electrophysiology of whole mitoplast later helped to confirm that MCU indeed forms the functional uniporter pore (Chaudhuri *et al*, 2013).

5.5.1 *In vivo* knockdown of MCU in mice

Mice subjected to siRNA mediated *in vivo* silencing of MCU in liver cells showed normal weight gain over a 3-week period, with the liver appearing normal with robust respiratory state transitions observed in isolated mitochondria. However, there was a near complete loss of Ca^{2+} uptake in response to Ca^{2+} pulses in the mitochondria isolated from the knockdown mice (Baughman *et al*, 2011). Studies with MCU knockout (*MCU* $^{-/-}$) mice showed that these mice have severely compromised mitochondrial Ca^{2+} uptake. The basal metabolism remained largely unaffected with the O_2 consumption rate comparable between the wild type and *MCU* $^{-/-}$ mice. Although *MCU* $^{-/-}$ mice could not perform strenuous work, these mice are viable despite defective mitochondrial Ca^{2+} uptake. The mitochondrial matrix of *MCU* $^{-/-}$ mice was found to contain significant amounts of Ca^{2+}, albeit at lower levels when compared to the wild type mice, pointing towards a different but slower Ca^{2+} uptake pathway in the *MCU*$^{-/-}$ cells.

5.5.2 MCU topology and localization

Confocal imaging of GFP-tagged MCU and immunoblotting of the mitochondrial fractions validated the localization of MCU to mitochondria in HeLa cells. Proteinase K digestion tests showed that the N- and C-termini of MCU are facing the mitochondrial matrix (Fig 5.3). Later studies using APEX (ascorbate peroxidase that can be used as an electron microscopy tag) fused to MCU, showed clear staining of mitochondrial matrix but not the intermembrane space, thus confirming that the N- and C-termini of MCU face the matrix space (Martell *et al*, 2012).

A few residues at the highly conserved loop region or DIME motif (Fig 5.3) connecting the two transmembrane helices in MCU were found to be crucial for the activity of the uniporter as the corresponding mutant cDNAs could not rescue Ca^{2+} uptake in MCU-silenced cells. This mutational analysis also helped in pinpointing the DIME motif of MCU as the Ru360 (the most potent inhibitor of Ca^{2+} uptake) binding region.

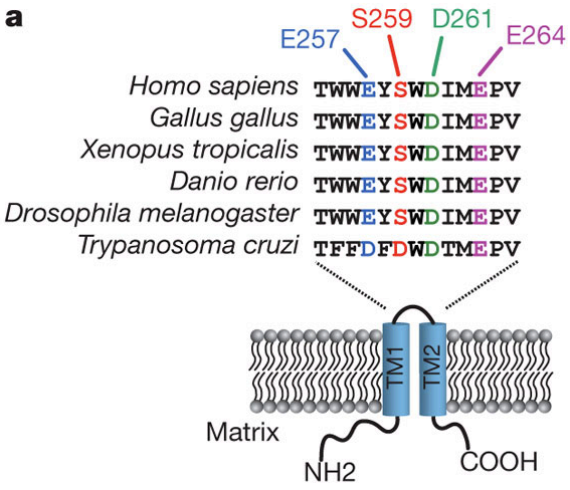

Figure 5.3 Multiple sequence alignment and topology prediction of MCU

Multiple sequence alignment representing the highly conserved MCU linker region (DIME motif) as well as the MCU topology across the inner mitochondrial membrane. (Baughman *et al*, 2011).

5.5.3 Functional assay of reconstituted MCU

HIS-tagged mouse MCU was expressed heterologously in *E. coli* and by using wheat-germ cell-free transcription/ translation (De Stefani *et al*, 2011). The membranes from *E. coli* were solubilized with 2.5% of DDM followed by Nickel affinity purification. The purified protein when reconstituted into planar lipid bilayers showed channel activity. The channel activity could be inhibited in the presence of Ruthenium red/ Gadolinium. Changing the two conserved negatively charged residues (D260 and E263) in the DIME motif into glutamines abolished the channel activity. However, later it was suggested that human MCU is inactive on its own and is functional only in the presence of a protein named EMRE (Sancak *et al*, 2013) (Kovács-Bogdán *et al*, 2014). In order to test this, *S. cerevisiae* that does not possess a mitochondrial calcium uniporter was used as a reconstitution system to identify the minimal genetic element sufficient for human uniporter activity (Kovács-Bogdán *et al*, 2014). Human MCU (hsMCU) when expressed alone in this system could not lead to calcium uptake. However, when hsMCU was expressed in the presence of EMRE, calcium uptake could be detected, which was sensitive to Ru360 and

dependent on membrane potential. Future studies with purified and reconstituted MCU and EMRE should resolve the inconsistent activity reports.

5.6 Is MCU part of a larger complex? Identification of MCU regulators/ interacting proteins

Immunoblots of digitonin-solubilized mitochondria on Blue Native PAGE show that MCU is a part of a large complex of about ~450 kDa (Baughman et al., Nature, 2011; Sancak et al, Science, 2013). Although several regulatory proteins were shown to be associated with MCU by immunoprecipitation studies, evidence for direct interaction of these components with MCU is lacking. On the other hand, co-immunoprecipitation and FRET analysis show that differently tagged MCU interact to form oligomers (Baughman *et al*, 2011; Raffaello *et al*, 2013). Evidence for MCU oligomerization also comes from Blue Native PAGE analysis of purified MCU (Raffaello *et al*, 2013). Hence it remains to be seen whether the large complex of 450 kDa containing MCU corresponds to just a homooligomer or a heterooligomer.

HEK-293T cells stably expressing MCU-FLAG were used to conduct proteomics studies to identify the interacting partners of human MCU. A quantitative mass spectrometry analysis (using stable isotope labeling by amino acids in cell culture/SILAC) of FLAG immunoprecipitate identified a total of 5 mitochondrial proteins (Sancak *et al*, 2013). These included MCU, MICU1 and MICU2 that are known regulators of MCU (Perocchi *et al*, 2010) (Baughman *et al*, 2011; De Stefani *et al*, 2011; Mallilankaraman *et al*, 2012; Hoffman *et al*, 2013; Plovanich *et al*, 2013) (Patron *et al*, 2014; Kamer & Mootha, 2014), MCUb, a paralog of MCU (Raffaello *et al*, 2013) and EMRE (Sancak *et al*, 2013) (Kovács-Bogdán *et al*, 2014). This mass spectrometry study along with a few functional studies of MCU interacting proteins led to a model wherein the human MCU is proposed to exist in a complex comprising of EMRE, MICU1, MICU2 and MCUb. This putative complex was named the 'uniporter complex' (Fig 5.4). Each component of the uniporter complex is proposed to have a specific regulatory role on the activity of MCU. However, it is worth

mentioning that there is no direct evidence for the existence of this complex either *in vivo* or *in vitro*. The schematic below shows the most recent model predicting the composition of the complex.

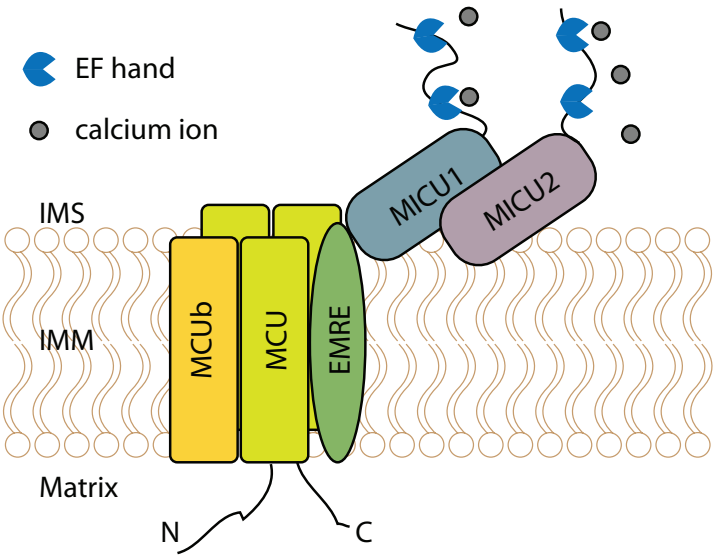

Figure 5.4 Components of the mitochondrial calcium uniporter complex

Mitochondrial calcium uniporter complex with the components identified so far. The protein components are not drawn to scale.

In the following sections, each component of the uniporter complex is reviewed and their effect on mitochondrial calcium uptake is discussed briefly.

5.6.1 Essential MCU regulator (EMRE)

EMRE is a 10-kDa protein with a mitochondrial targeting sequence, a putative transmembrane helix and a C-terminus rich in highly conserved aspartic acid residues (Fig 5.5). It is found only in metazoans, unlike MCU and MICU1 that are present in all major eukaryotic taxa and are ubiquitously expressed in all mammalian tissues. RNAi mediated silencing of EMRE leads to the loss of mitochondrial uptake of calcium, which cannot not be restored by MCU overexpression (Sancak *et al*, 2013).

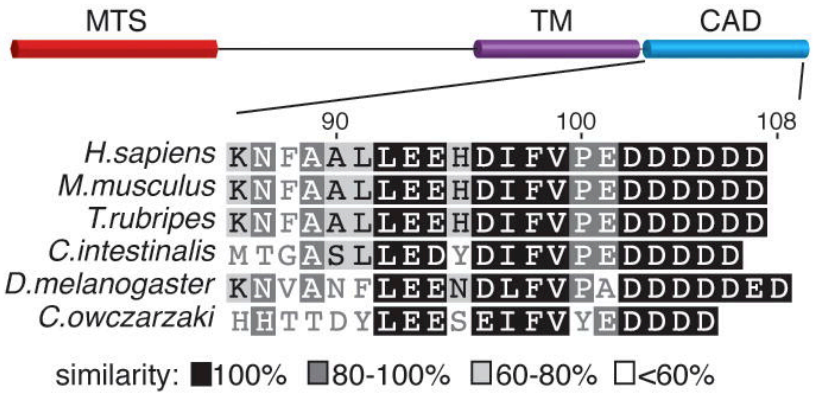

Figure 5.5 Secondary structure prediction of EMRE

The mitochondrial targeting sequence (MTS), the transmembrane helix (TM) and the conserved carboxy terminal acidic tail (CAD) are shown. The CAD domain of EMRE from 6 species was aligned using BLOSUM similarity matrix. (Sancak *et al*, 2013).

Immunoprecipitation studies with cells lacking EMRE show that the interaction between MCU and MICU1/MICU2 is lost and the size of the mitochondrial calcium complex is reduced from ~480 kDa observed for the native complex to ~300 kDa in the knockout cells. Since hsMCU (human MCU) could form high molecular weight oligomers (~300kDa) in the membrane even in the absence of EMRE, it is possible that EMRE is not involved in the oligomerization of MCU but in the function itself.

5.6.2 MCUb

MCUb is a paralog/isogene of MCU (Raffaello *et al*, 2013). Sequence analysis of MCU led to the identification of a related gene CCDC109B, which encodes a protein that shares 50% sequence identity with MCU itself. MCUb is absent in certain organisms like plants, kinetoplastids, nematodes and arthropods, even though they possess MCU. MCUb has two predicted highly conserved transmembrane helices that are separated by a short loop akin to MCU, except that it has key mutations in the DIME motif that are predicted to make the protein non-functional. Hetero-oligomerization of MCU and MCUb was demonstrated by co-immunoprecipitation studies and FRET experiments using differently labeled MCU and MCUb (Raffaello *et al*, 2013). When

co-expressed with MCUb, MCU channel activity is reduced, supporting the hypothesis that MCUb is a dominant negative form of MCU.

Based on mRNA quantification in cells, MCUb expression levels are in general lower than for MCU (Raffaello *et al*, 2013). Also, the MCU/MCUb expression ratio varies widely in human tissues. For e.g. MCUb mRNA has low expression levels in skeletal muscle cells compared to cardiac cells. Interestingly, tissue-dependent variations in mitochondrial calcium uptake have been observed, with a recorded skeletal muscle Ca^{2+} uptake that is 28 fold higher than in cardiac mitoplasts (Fieni *et al*, 2012), corroborating the various expression levels of these two paralogs. Further studies in this direction will lead to a better understanding of the tight regulation of the expression of these two paralogues and will shed light on the tissue specific Ca^{2+} uptake by mitochondria.

5.6.3 Mitochondrial Calcium Uptake 1 and 2 (MICU1 and MICU2)

A combination of bioinformatics and proteomics was used to identify the first component of the mitochondrial uniporter complex namely MICU1 (Mitochondrial Calcium Uptake 1) (Perocchi *et al*, 2010). MICU1 is predicted to contain an N-terminal mitochondrial targeting sequence (mts) and two canonical Ca^{2+}-binding EF hand domains. It is targeted to the intermembrane space along with MICU2, a paralog of MICU1 (Sancak *et al*, 2013) (Plovanich *et al*, 2013). Knockdown of MICU1 did not alter the mitochondrial membrane potential (ϕ_m) or the basal respiration rate confirming that oxidative phosphorylation is intact in MICU1-silenced cells. Exhaustive calcium uptake measurements in cell populations and individual cells using various techniques confirmed the role of MICU1 in mitochondrial calcium handling as well as in coupling cytosolic Ca^{2+} transients and mitochondrial energy metabolism (Baughman *et al*, 2011; Mallilankaraman *et al*, 2012; Hoffman *et al*, 2013). Rescue experiments using cDNA carrying EF hand mutations demonstrated that the EF hands are essential for mitochondrial Ca^{2+} uptake. The presence of these

EF hands led to the proposal that MICU1 could be a Ca^{2+}-sensitive regulator of the uniporter activity (Perocchi *et al*, 2010).

Later studies showed that MICU1 acts as a gatekeeper for MCU-mediated Ca^{2+} uptake, by limiting Ca^{2+} uptake at baseline cytoplasmic $[Ca^{2+}]_c$ levels (Mallilankaraman *et al*, 2012). When the $[Ca^{2+}]_c$ exceed a threshold level, MICU1 releases the inhibition on MCU and Ca^{2+} transport takes place through the uniporter (Csordás *et al*, 2013). Based on the crystal structure of the soluble domain of human MICU1 in the presence and absence of Ca^{2+}, it was proposed that Ca^{2+} binding leads to the disassembly of a hexameric MICU1 (Wang *et al*, 2014). This disassembly of hexameric MICU1 was predicted to release its inhibition on MCU (Wang *et al*, 2014).

5.7 Aim of this work

A surge of research after the discovery of MCU has been successful in the identification and extensive characterization of the mitochondrial calcium uniporter complex. With the identification of key components that regulate calcium uptake by the uniporter, the general picture is that the uniporter complex is far more complex than once anticipated. What is lacking essentially at this point is structural information on the whole complex as well as on its individual components. Advances in this direction could throw light on how the complex assembles (for e.g. stoichiometry), how it operates and regulates its own activity.

The main aim of this study was to determine the crystal structure of the human mitochondrial calcium uniporter. Obtaining any structural information on the uniporter could contribute to our understanding of the Ca^{2+} uptake mechanism. Importantly, large-scale purification of MCU has not been reported in the literature. Though human MCU could be heterologously expressed and purified, the amount of protein obtained was very low (as shown by silver staining and western blots) and is not sufficient for extensive protein characterization (De Stefani *et al*, 2011). Therefore, it is imperative to establish and optimize a recombinant expression and purification method for the human mitochondrial calcium uniporter.

6 Materials

The Methods used in this section of the thesis overlap with the first section. Hence, only the oligonucleotides used specifically in this part of the study are mentioned below (Table 6.1).

6.1.1 Oligonucleotide primers

Table 6.1 Oligonucleotide primers for cloning various MCU constructs

Isoform	Construct	Primer Sequence (5' to 3')	Details
CCDC109A/ Isoform 1	Δmts_56	GACAACCATATGGCTTCGTGGCAGAACCTGGG	FP with Nde1 RS
	Δmts_38	GACAACCATATGGGTGTGTCACGTCATCGCCAG	FP with Nde1 RS
	FL_1	GACAACCATATGGCGGCGGCGG	FP with Nde1 RS
	c191	GACAACCATATGTGTATCGAACAACATCAACTG	FP with Nde1 RS
	c164	GACAACCATATGAAACGCGACCTGCTGAGCCAC	FP with Nde1 RS
	c62	GACAACCATATGGGTGCGGTTTATTGCAGTACC	FP with Nde1 RS
	c291	GTAAGCCTCGAGTCAGTAAACATATTCTTGGCGGGTC	RP with Xho1 RS
	c336	GTAAGCCTCGAGTCAGTCACGCAGACGTTTCAGGTC	RP with Xho1 RS
	sol_233	GTAACCTCGAGTCACGTGGTACGTTTTTCTGCTTTGCG	RP with Xho1 RS
	sol_233	GTAACCTCGAGCGTGGTACGTTTTTCTGCTTTGCG	RP with Xho1 RS + no stop codon for C-term tag
C10042/ Isoform 2	Δmts_56	GACAACCATATGGCCTCTTGGCAGAACCTGGG	FP with Nde1 RS
	Δmts_38	GACAACCATATGGGTGTTTCCCGTCATCGCCA	FP with Nde1 RS
	sol_212	GTAACCTCGAGTCACGTGGTACGTTTTTCGGCTTTGC	RP with Xho1 RS
	sol_212	GTAACCTCGAGCGTGGTACGTTTTTCGGCTTTGC	RP with Xho1 RS + no stop codon for C-term tag
	sol_163	GTAACCTCGAGTCACGGCGGACGAACATGATACGTC	RP with Xho1 RS
CCDC109A/ Isoform 1 + C10042/ Isoform 2	mcu_351	GTAACCTCGAGTCAATCTTTTTCGCCAATTTGACGCAGCG	RP with Xho1 RS
	mcu_351	GTAACCTCGAGATCTTTTTCGCCAATTTGACGCAGCG	RP with Xho1 RS + no stop codon for C-term tag

FP: forward primer; RP – reverse primer; RS – restriction site

7 Results

7.1 Rational design of MCU constructs for expression in *E. coli.*

As shown in the domain architecture scheme (Fig 2.9), MCU is a multi-domain protein and thus needs a rational approach in designing the optimal constructs for expression, purification and crystallization. MCU contains two predicted transmembrane helices flanked by two predicted coiled-coil domains. In addition, MCU also contains a mitochondrial targeting sequence (MTS), a hydrophobic helix and an α/β soluble domain at the N-terminus (Fig 7.1).

MCU is thought to exist as two different isoforms in humans. Isoform 1 is the principal form of the protein that is being studied extensively. Isoform 2 was only detected in a large-scale study at the mRNA level (Ota *et al*, 2004). When compared to MCU isoform 1, isoforms 2 lacks a small stretch of a predicted coiled-coil region N-terminal to the transmembrane helices (Fig 7.1). In this study, I decided to work with both isoforms in order to identify the one better suitable for structural studies. Probable MCU domain boundaries were determined using a combination of secondary structure prediction (Biegert *et al*, 2006) and sensitive domain recognition software (Söding *et al*, 2005). Eight constructs with varying combinations of the predicted domains were designed (Fig 7.1). For cloning these constructs, synthetic genes of the human mcu isoforms 1 (CCDC109A, Uniprot id: Q8NE86-1) and 2 (ORF42, Uniprot id: Q8NE86-2) were purchased from Genscript, with codons optimized for expression in *E. coli*. Each gene was sub-cloned from the pUC57 vector into the pET15-b vector with Nde1 and Xho1 restriction sites. All eight constructs contained an N terminal thrombin cleavable site to remove the hexa-histidine tag.

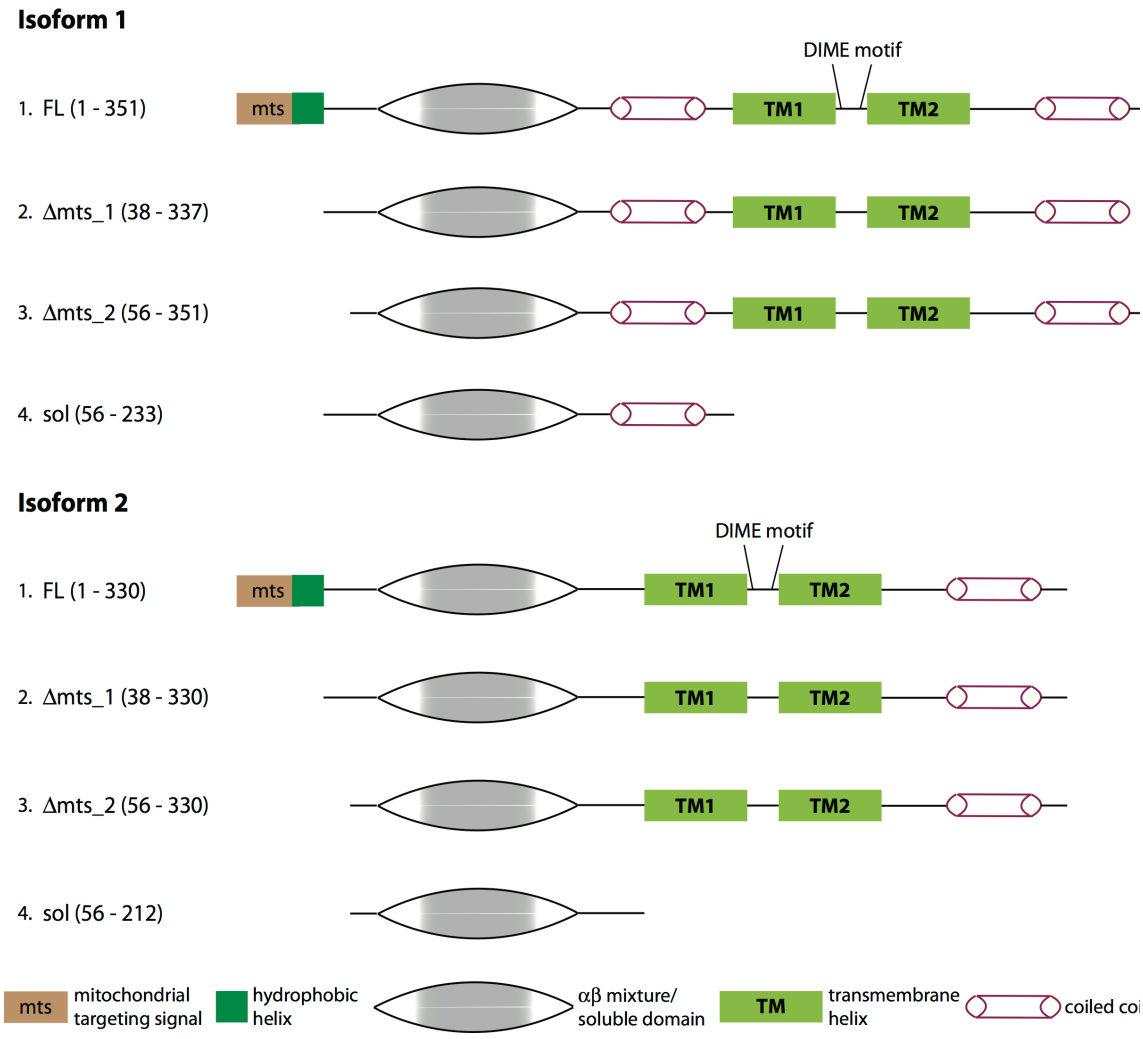

Figure 7.1 Putative domain architecture and construct design for MCU isoforms 1 and 2

For both isoforms the following constructs were designed and cloned into pET15-b vector. 1. Full-length protein (isoform 1: 1-351 and isoform 2: 1-330), 2. Construct lacking mitochondrial-targeting sequence (Δmts_1; isoform 1: 38-337 and isoform 2: 38-330), 3. Construct lacking MTS and the N-terminal hydrophobic helix (Δmts_2; isoform 1: 56-351 and isoform 2: 56-330), 4. Soluble domain (isoform 1: 56-233 and isoform 2: 56-212).

7.2 Expression tests of Δmts and soluble domain constructs of mcu

7.2.1 Δmts_2 constructs comprising membrane-spanning region

The plasmids were transformed into BL21-pLysS cells for expression. Cells were grown in 100ml of TB media to an OD_{600} of 0.6-0.9 at 37°C and expression was

induced with 0.5mM IPTG at 30°C. The overexpression of Δmts_2 from isoform 1 (56-351) and isoform 2 (56-330) could be detected when bacterial cells were loaded in the gels (Fig 7.2A). Cells were harvested and resuspended in lysis buffer containing 50mM HEPES, 200mM NaCl, 1mM TCEP, 1mg/ml lysozyme, 1 tablet of protease inhibitor cocktail (EDTA free, Roche), 1mM PMSF and DNase. The cells in lysis buffer were incubated for 30 minutes on ice. The crude cell lysate was centrifuged to remove cell debris (10,000g, 4°C, 30min) and the supernatant was subjected to high-speed centrifugation (125,000g, 4°C, 60 min) to obtain the membrane fractions. The membranes were homogenized and solubilized overnight in solubilization buffer containing 25mM HEPES, 50mM NaCl, 1mM TCEP, 10% Glycerol and 2% DDM. The membranes were centrifuged again to remove detergent-insoluble material. Samples were run on an SDS-PAGE gel followed by Western blotting (Fig 7.2B).

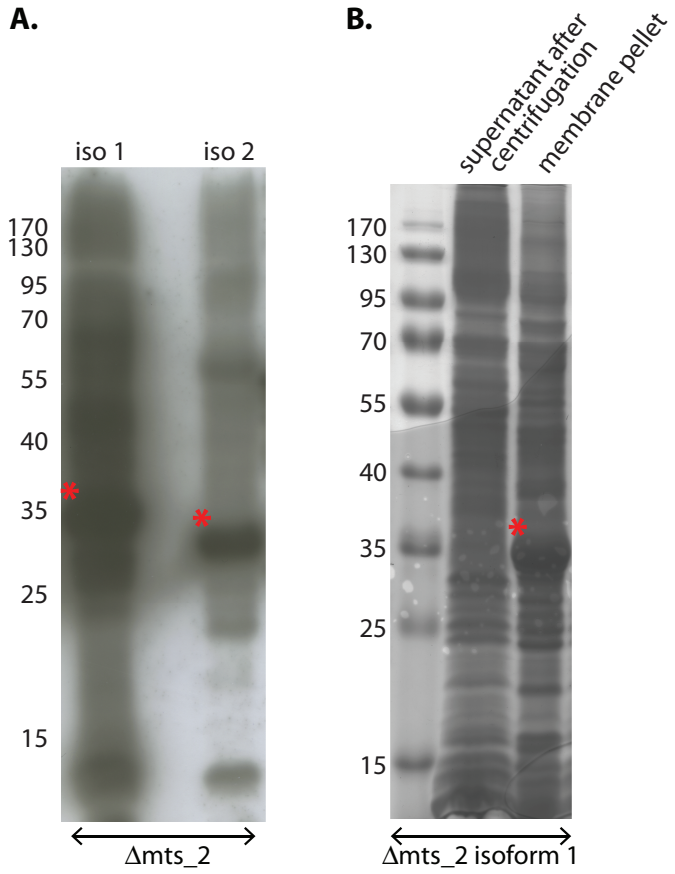

Figure 7.2 Small-scale expression/ purification of Δmts_2 constructs

(A) Western blot of whole cells of Δmts_2 from isoform 1 and 2 loaded on an SDS gel and blotted using anti-His antibody. Isoform 1 Δmts has a molecular weight of 36.7 kDa together

with the tag while isoform 2 Δmts is 33.8 kDa. A red asterisk indicates the suspected protein bands. (B) Solubilization of Δmts_2 from isoform 1 using 2% DDM. Most of the protein remained in the unsolubilized membrane fraction and is marked by a red asterisk.

7.2.2 Soluble domain of isoform 1

The cells were grown, induced for expression and lysed similar to full-length protein and Δmts constructs. After lysis, the crude cell lysate was centrifuged at 50,000g for 30 min at 4°C to remove cell debris. During soluble domain purification, composition of binding and elution buffers was kept the same as in Δmts construct purification but without the detergent. The cleared cell lysate was then incubated with Ni^{2+}-chelating sepharose beads. After extensive washing, the protein bound to beads was eluted in fractions using 200mM imidazole. Eluted proteins and the remaining Ni^{2+}-beads were analyzed on SDS-PAGE (Fig 7.3). Coomassie staining of SDS gels and Western blotting using anti-HIS antibody clearly showed that the MCU soluble domain is expressed and can be enriched using affinity beads. However, a large fraction of the MCU soluble domain remained bound to the beads even after elution with 200mM imidazole indicating a possible non-specific binding to the the Ni^{2+} beads (Fig 7.3).

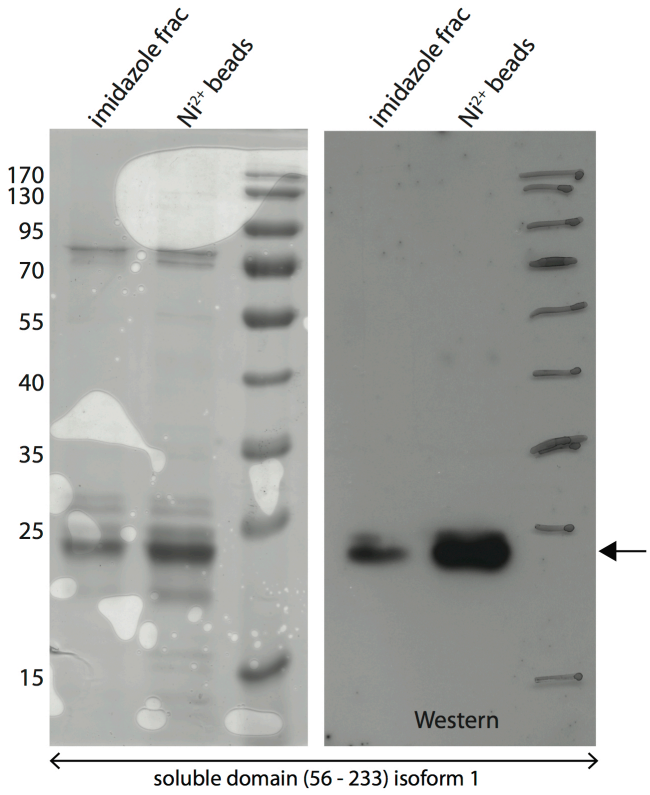

Figure 7.3 Small-scale expression/ purification of the soluble domain of isoform 1

Small-scale purifications of the soluble domain (56-233) of isoform 1. Protein is detectable in the imidazole elution fraction and also in a fraction containing Ni^{2+} beads. The expected molecular weight (protein + hexa-His-tag) is 22.6 kDa. An arrow indicates the expected protein band in the SDS gel as well as the Western blot.

7.3 Large-scale purification of the soluble domain of isoform 1

Although the main aim of this project is to obtain structural information on the whole protein including the transmembrane domains, attempts were also made to obtain structural information on the soluble domain. Towards this end, the soluble domain was expressed and purified on a large scale. The expression plasmid containing the soluble domain of isoform 1 was transformed into BL21-pLysS cells for expression. Cells were inoculated in 9 liters of TB or LB media and grown to an OD_{600} of 1.0 at 37°C. Cells were then induced for expression with 0.5mM IPTG at 18°C and grown overnight.

Cells were harvested and the cell pellet was homogenized in lysis buffer (1ml lysis buffer for each gram of cell pellet) containing 50mM Tris pH 7.5, 200mM NaCl, 1mM TCEP, 10% Glycerol, 3 tablets of protease inhibitor cocktail (EDTA free from Roche), 1mM PMSF and DNase. The cells were lysed using a microfluidizer and the crude cell lysate was centrifuged at low speed (10,000g, for 20 min at 4°C) to remove cell debris. The supernatant containing 20mM imidazole was applied to a 5ml HisTrap column (Ni^{2+} Sepharose from GE Healthcare) at 4°C. After washing with at least 10 CV of binding buffer containing 20mM imidazole, the protein was eluted with a concentration gradient of 20 to 225mM Imidazole over 30 CV of buffer (Fig 7.4A). The eluted fractions were pooled and loaded on an anion-exchange column (Mono Q). While the protein of interest was in the flowthrough, impurities bound to the Mono Q column (Fig 7.4B). The flowthrough of the Mono Q was concentrated and loaded on a size-exclusion column (Superdex 200 Increase 10/300). The protein of interest eluted as a monomer in a single homogenous peak (Fig 7.4C). Samples from various stages of the purification were analyzed using SDS-PAGE (Fig 7.4C). The protein after size-exclusion chromatography showed >90% purity as judged from the coomassie stained SDS gel.

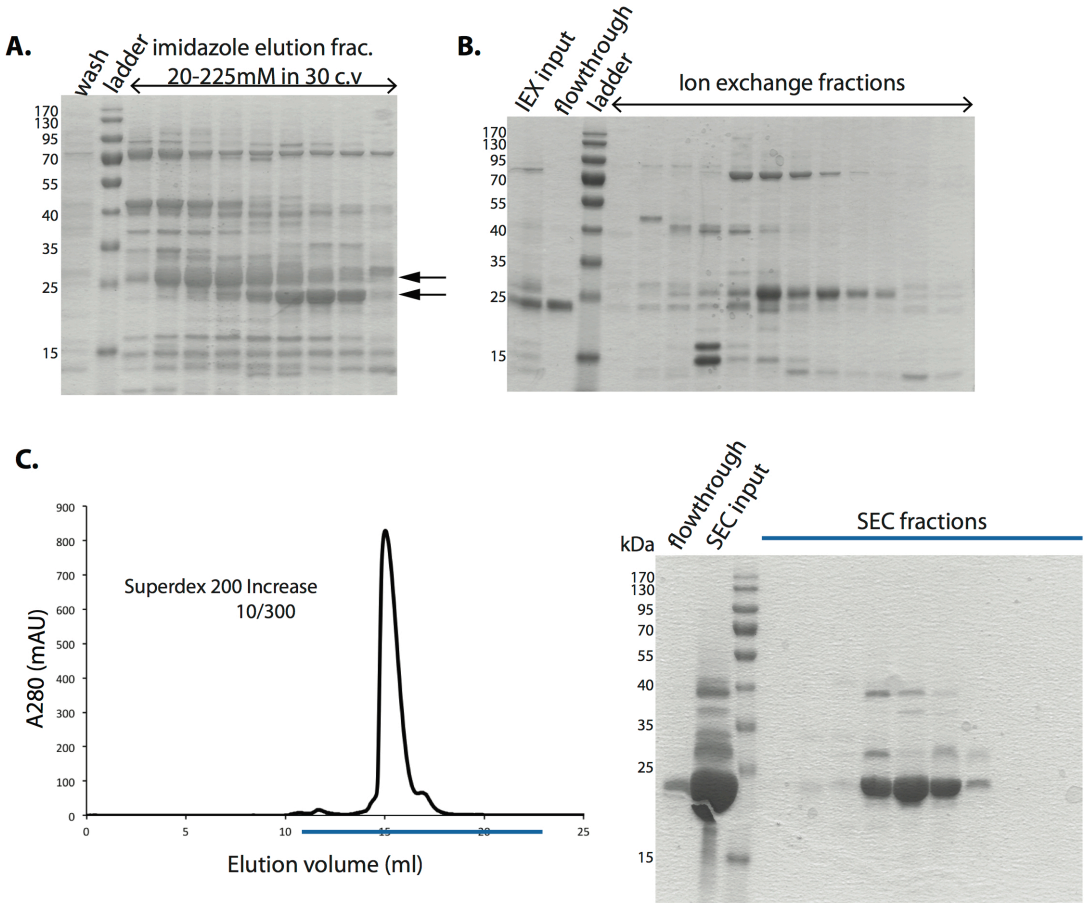

Figure 7.4 Large-scale purification of isoform 1 soluble domain

(A) Nickel affinity purification of isoform 1 soluble domain 56-233 using an imidazole linear gradient of 20 to 225mM over 150ml in order to separate the bands indicated by the arrows. (B) The elution fractions were pooled and loaded on an ion exchange column (IEX, mono Q). The flowthrough contained the protein of interest while the impurities bound to the column. (C) Size-exclusion chromatography of the concentrated flowthrough from IEX. The fractions from the Superdex 200 column were loaded on an SDS gel.

The purified protein was concentrated to 10 mg/ml and attempts were made to crystallize the protein using commercially available sparse matrix screens. Crystallization plates were set up at 18°C and 4°C. However, no crystals were obtained. Meanwhile, I worked on solubilizing and purifying the larger constructs of MCU with the membrane-spanning domain.

7.4 Detergent solubilization tests of Δmts_1 constructs of isoform 1 and isoform 2

As seen during expression tests (Fig 7.2), MCU Δmts_1 of isoform 1 and isoform 2 could be expressed in *E. coli* but were not getting solubilized using 2% DDM. Therefore, several detergents were used in solubilization tests to extract these proteins from the membrane. Several commonly used non-ionic (maltosides and glucosides) as well as zwitter-ionic detergents were tested. A few ionic detergents like SDS were also used as a control.

Membranes of Δmts_2 construct of MCU isoform 1 (56-351) and Δmts_1 construct of MCU isoform 2 (38-330) were isolated from small-scale cultures and were resuspended in 50mM HEPES, 200mM NaCl, 2mM TCEP and 20% Glycerol (2X solubilization buffer). To accurately measure the concentration of the protein in the membrane fraction, serial dilutions of the membrane fractions were made and the concentration of each dilution was measured using the BCA assay and a BSA standard calibration curve. To 480 µl of 0.5-1 mg/ml membranes, various detergents to a final concentration of 2% were added. Water was added to this mixture to make up the final volume to 960 µl. These solutions were kept overnight at 4°C on a rotary shaker. Afterwards, high-speed centrifugation was carried out to separate solubilized membrane from the insoluble material. The soluble fractions obtained using various detergents were loaded an SDS gel, blotted onto a nitrocellulose membrane and probed using anti-HIS antibody (Fig 7.5). Samples were also collected before the high-speed centrifugation step. These samples served as a control to assess the total amount of protein present in the membrane and the efficiency of protein extraction from the membrane by each detergent.

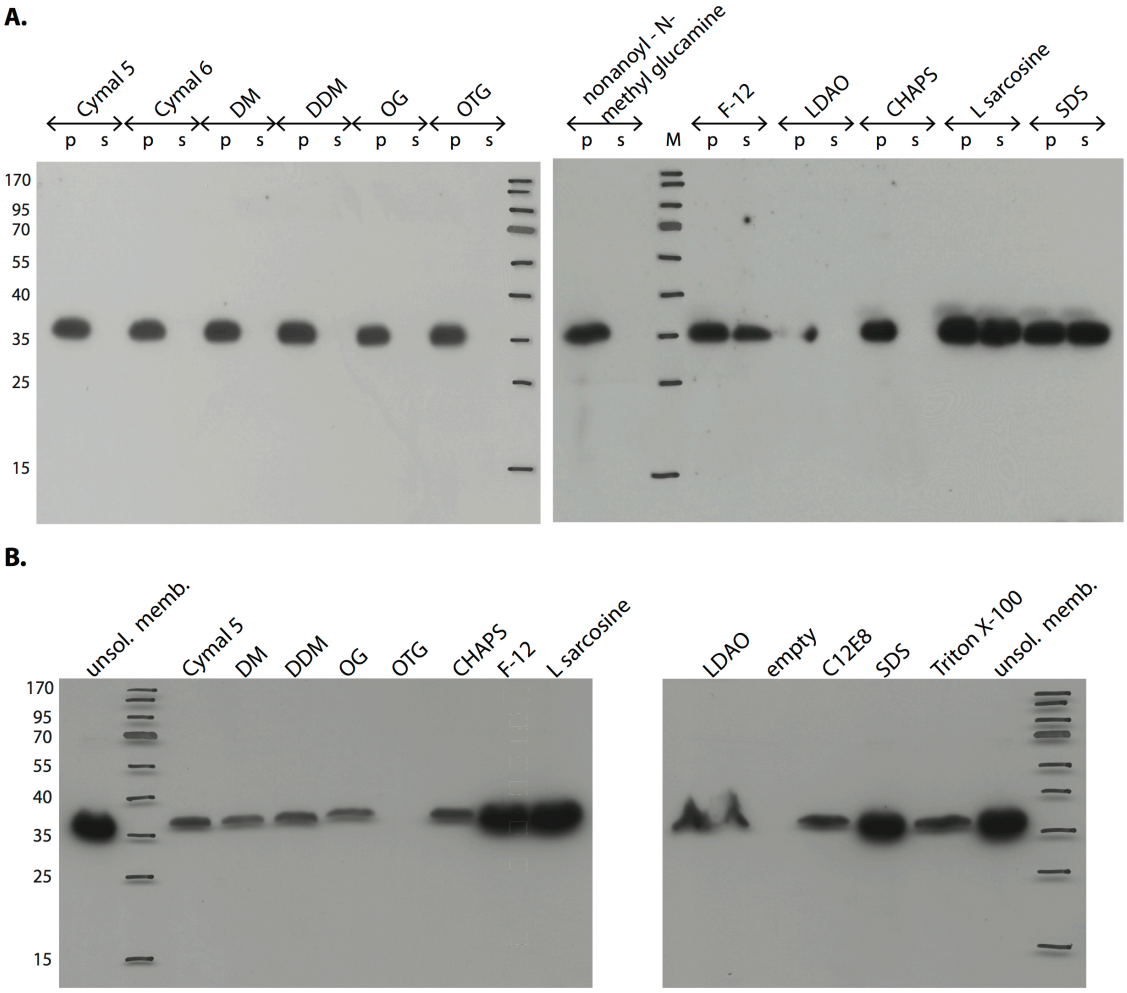

Figure 7.5 Detergent solubilization of Δmts isoform 1 and 2

(A) Soluble (s) and insoluble (p) membrane fractions of Δmts_1 construct of isoform2 (38-330). The overexpressed/solubilized protein has an expected molecular weight of 36 kDa (including the hexa-His-tag). (B) Western blot of Δmts_2 construct of isoform1 (56-351) membranes solubilized using various detergents. Here, only the supernatant after solubilization was loaded on an SDS gel and blotted with an anti His-antibody. Only one unsolubilized membrane sample (unsol. memb.) was loaded on each gel to compare the amount of protein in membrane before solubilization. The expected molecular weight is 36.7kDa (including the hexa-His tag).

The results indicate that for both Δmts constructs 2% Foscholine-12 (Fos-12) works best to solubilize the protein out of the membranes. Interestingly, for Δmts_2 construct of isoform1, partial solubilization was also achieved using Cymal-5, DM, DDM, OG, LDAO and $C_{12}E_8$ (Fig 7.5). It is not clear if this difference in solubilization for both isoforms arises from the difference in construct design or due to slight

variations in protein concentration in the membrane for both preparations, which in turn can influence the efficiency of the solubilization. From this analysis Fos-12 was chosen as the detergent of choice. Further experiments were planned to optimize the detergent concentration and the detergent:membrane ratio to yield optimal solubilization conditions.

7.4.1 Optimizing the solubilization of the Δmts construct

Although Foscholine-12 is a lipid-like detergent and has been successfully used for protein structure determination (NMR as well as X ray crystallography (Kefala *et al*, 2010; Hwang *et al*, 2002; Oxenoid & Chou, 2005), it is considered harsh due to its zwitterionic nature. It was therefore important to test various concentrations of Foscholine-12 (Fos-12) for solubilization of the Δmts containing membranes. The idea is that the optimal concentration of Fos-12 should extract mcu from the membranes efficiently without unfolding the protein's native state. Towards this end several concentrations of Fos-12 (Critical Micelle Concentration or CMC: 0.0475 %) were used (Fig 2.14). The final membrane protein concentration used was 0.5 mg/ml.

Additionally, shorter and longer chain versions of Fos-12, namely Fos-10 (CMC: 0.35%) and Fos-14 (CMC: 0.005%) were also tested for their ability to solubilize the membranes (Fig 2.14A). Due to its high CMC, Fos-10 can be easily removed (*e.g*. by dialysis), at later stages of purification if required. This was one of the reasons why Fos-10 was tested. Fos-14 on the other hand is the harshest of the three detergents and it is difficult to exchange at later steps. However, Fos-14 may stabilize the protein because of its longer hydrophobic chain. Western blot analysis of solubilized membrane fractions showed that both detergents, Fos-10 and Fos-14, could solubilize the protein. Of all the tested detergents and concentrations, Fos-12 seemed the most efficient in solubilizing the proteins (Fig 7.6A). Since 0.5% of Fos-12 appeared to solubilize the protein as efficiently as 2% Fos-12, lower concentrations

were tested as well (Fig 7.6B). While 0.1% could partially solubilize the protein, a concentration of 0.05% Fos-12 was not enough to solubilize the protein.

In order to test if the HIS-tagged Δmts MCU proteins solubilized using Fos-12 can be enriched using Ni^{2+} -chelating sepharose beads, the supernatant of the Fos-12 solubilization was pooled and incubated with Ni^{2+} beads. After washing the beads with wash buffer (50mM HEPES, 150 mM NaCl, 1 mM TCEP, 10% Glycerol, 15 mM Imidazole, 0.2% Fos-12), the protein was eluted using the same buffer containing 500mM imidazole (Fig: 7.6B). Samples were analyzed using SDS PAGE followed by Western blotting. Only a small fraction of MCU was found in the flowthrough, indicating efficient binding of the His tagged MCU to the Ni^{2+} beads. Most of the protein bound to the beads could be eluted with 500mM imidazole, though some protein still remained bound (Fig 7.6B).

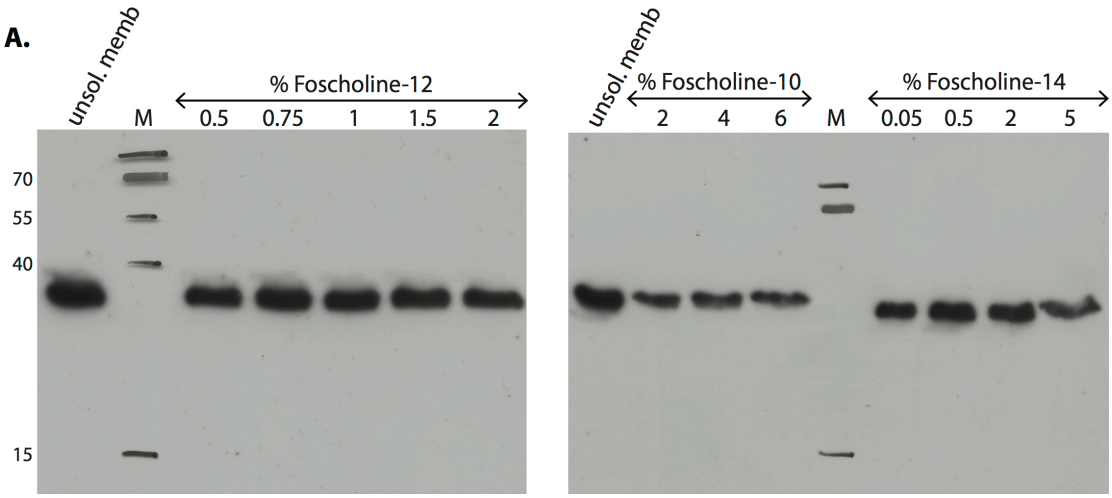

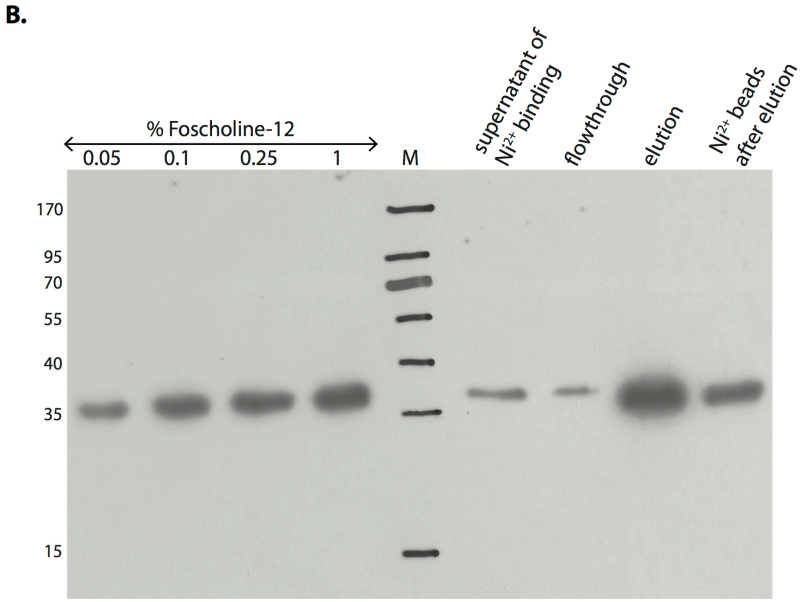

Figure 7.6 Detergent solubilization and purification of Δmts_1 construct of isoform 1

(A) Western blot of Δmts_2 of isoform 1 (56-351) membranes solubilized using various concentrations of Fos-12. The expected molecular weight is 36.7kDa (including the hexa-His-tag). On the right side is a gel showing membranes solubilized using various concentrations of Fos-10 and Fos-14. (B) Lower concentrations of Fos-12 were tested for solubilization. Also small scale Nickel affinity purification of MCU shows successful elution of the protein from the Ni^{2+} beads Δmts_2 isoform 1.

7.5 Purification of Δmts_1 and Δmts_2 constructs of isoform 1

Since Δmts constructs of both isoform 1 and isoform 2 were expressing well, isoform 1 was chosen as the major candidate as it was the most studied one and had an extra domain compared to isoform 2. To scale up the previous solubilization experiment using Fos-12 and to compare the yield and the stability of different Δmts constructs of MCU, a medium-scale purification of Δmts_1 and Δmts_2 constructs of MCU isoform 1 was performed (Fig 7.7A). The plasmids were transformed into BL21-pLysS cells for expression. Cells were grown in 300ml of TB or LB media to an OD_{600} of 0.6-0.9 at 37 ^{0}C and expression was induced with 0.5mM IPTG at 30 ^{0}C.

Cells were harvested and the cell pellet was homogenized in lysis buffer containing 50mM sodium phosphate pH 7.0, 300mM NaCl, 1mM TCEP, 10% Glycerol, protease

inhibitor cocktail (EDTA free, Roche), 1mM PMSF and DNase. The cells were lysed by sonication and the resulting suspension was centrifuged (17,000g, 35 min, 4°C) to remove cell debris and the supernatant was subjected to high-speed centrifugation (125,000g, 60min, 4°C) to obtain the membrane fractions. The membranes were homogenized using a potter-douncer in 2X solubilization buffer containing 100mM NaP pH 7.0, 400mM NaCl, 2mM TCEP, 20% Glycerol. The membranes were solubilized with 2% Fos-12 overnight at 4°C. The insoluble material was removed by ultracentrifugation. The supernatant containing 10mM imidazole was incubated with Talon Co^{2+} beads for 1 hour at 4°C. After washing with at least 10 CV of binding buffer (50mM NaP pH 7.0, 250mM NaCl, 1mM TCEP, 10% Glycerol, 0.15% Fos-12 and 10mM Imidazole), the protein was eluted with 150mM imidazole in binding buffer (Fig 7.7B). The elution fractions for both the constructs mostly contain the protein of interest. Curiously, a small fraction of degraded protein can be detected, migrating slightly faster on the SDS PAGE gel (marked with a red asterisk). Attempts to crystallize both the purified constructs did not succeed. Given that the two purified proteins were prone to degradation, it was evident that the designed constructs are not optimal. Therefore, the construct boundaries must be redefined to obtain more stable proteins suitable for crystallization.

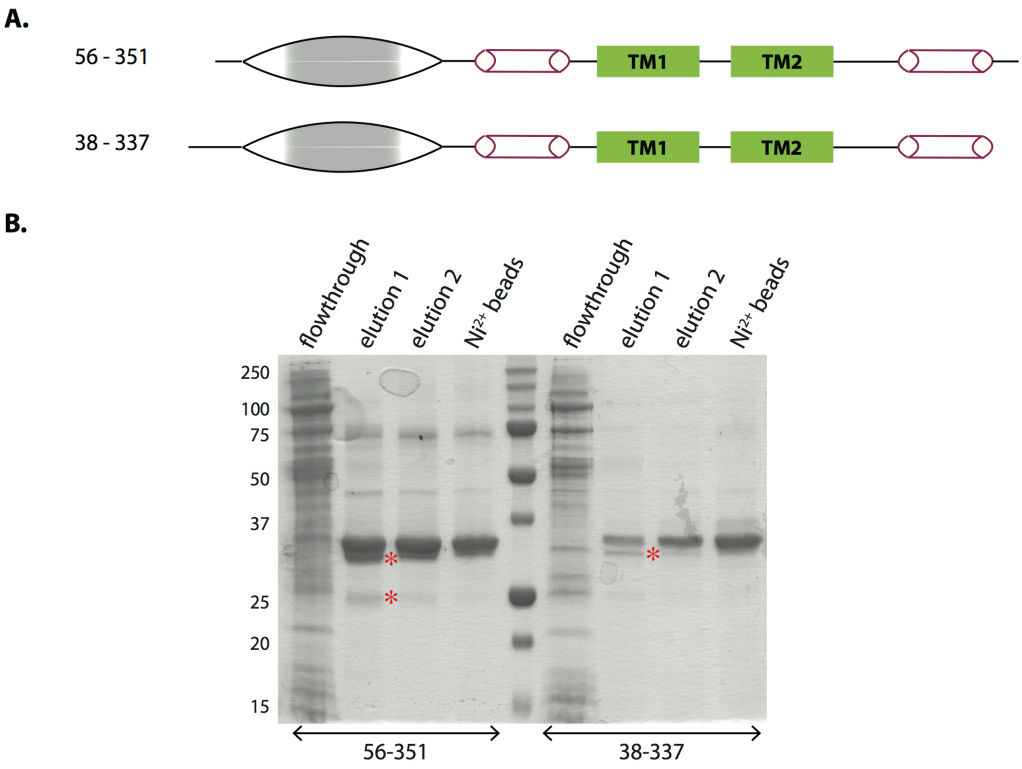

Figure 7.7 Purification of isoform 1 Δmts_1 and Δmts_2

(A) The constructs used for purification. These constructs had N-terminal and C-Terminal truncations lacking the flexible regions at both ends and thus were expected to yield a stable product. (B) SDS gel showing fractions from a medium-scale purification of the Δmts constructs. Δmts_1 had a molecular weight of 37.2 kDa and Δmts_2 36.7 kDa with the hexa-His-tag. The red stars indicate possible degradation products of both constructs.

7.6 Identification of a stable construct for purification and crystallization – using mass-spectrometry, secondary structure prediction and expression tests

The two Δmts constructs mentioned in the previous section underwent proteolytic cleavage (red asterisk, Fig 7.7B), indicating the presence of unstructured regions either at the N- or C-termini of the protein. In order to identify the final product of degradation, the bands from the SDS gel corresponding to the degradation product were subjected to LC-MS (Liquid chromatography-mass spectrometry) analysis at the Mass Spectrometry facility at the Max-Planck Institute for Biophysics. The bands were cut out from the SDS gel (Fig 7.8) and digested with trypsin or chymotrypsin or both. The peptide sequence coverage obtained by protease digestion was mapped

to identify the stable construct of mcu isoform 1 (Fig 7.9). Combining the LC-MS results and the secondary structure prediction, a new construct (C62-336) that included the soluble α/β –domain, the coiled coils as well as the transmembrane domain was designed.

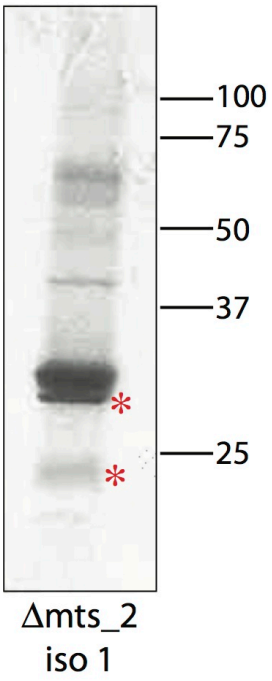

Figure 7.8 Degradation of isoform 1 Δmts_2

Purified protein was run on an SDS gel. The bands marked by the two red asterisks were cut out and subjected to LC_MS analysis.

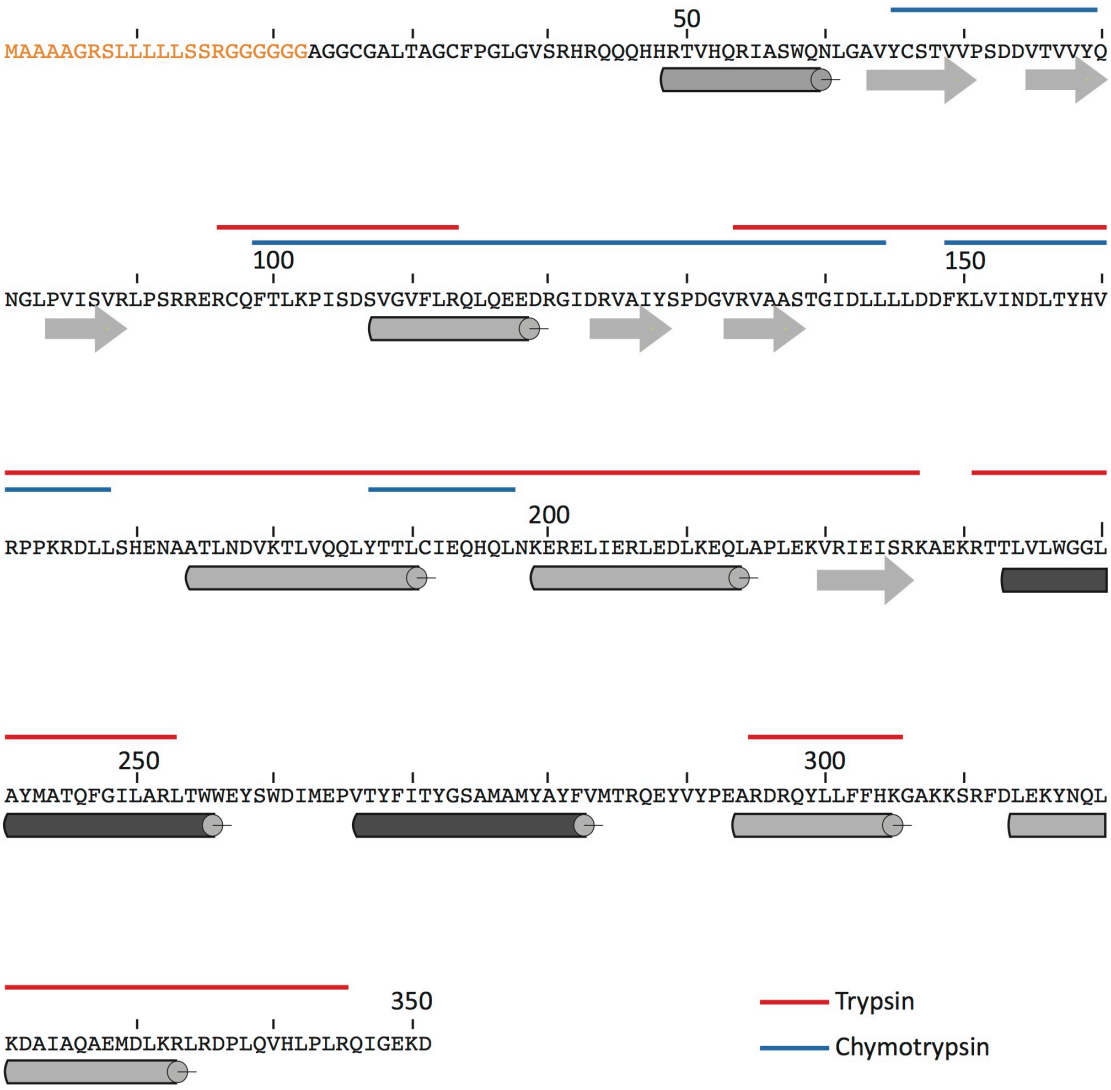

Figure 7.9 Secondary structure prediction and peptide coverage of isoform1

α -helices and β -sheets are shown as cylinders and arrows, respectively. The mitochondrial targeting signal at the N-terminus, which is cleaved in the mature protein is shown in orange. The dark colored helices indicate the transmembrane domain. The peptides cleaved by trypsin and chymotrypsin are color coded in red and blue, respectively, and are shown above the amino acid sequence.

In addition to C62-336, several smaller constructs were also designed based just on the secondary structure prediction, expecting better expression and more stable protein. These constructs are listed below.

C191-291

The shortest construct designed for expression is C191-291. According to the secondary structure prediction (psipred), this construct consists only of the two transmembrane helices and a predicted coiled coil region at the N-terminus. This construct was designed to contain only the functional core of the molecule lacking the soluble α/β domain and also the flexible N- and C- termini (Fig 7.10A).

C164-291

This construct is similar to c191-291 except for a slightly longer N-terminal region predicted to contain an additional helix.

C62-291

C62-291 contains the soluble α/β domain at the N-terminus but is truncated at the C-terminus immediately after the transmembrane domain.

C38-291

This construct is comparable to C62-291 except that it contains an additional hydrophobic helix at the N-terminus.

These constructs were all cloned into a pET15-b vector using Nde1 and Xho1 restriction sites. The small-scale expression and purification was performed for these constructs as explained before for the constructs 56-351 and 38-337. Of all the constructs purified, the best expression was observed for C62-336 (Fig 7.10B). Since the construct C62-336 also appeared to be stable, in concurrence with the mass spectrometry data, it was chosen for further large-scale purification and crystallization studies.

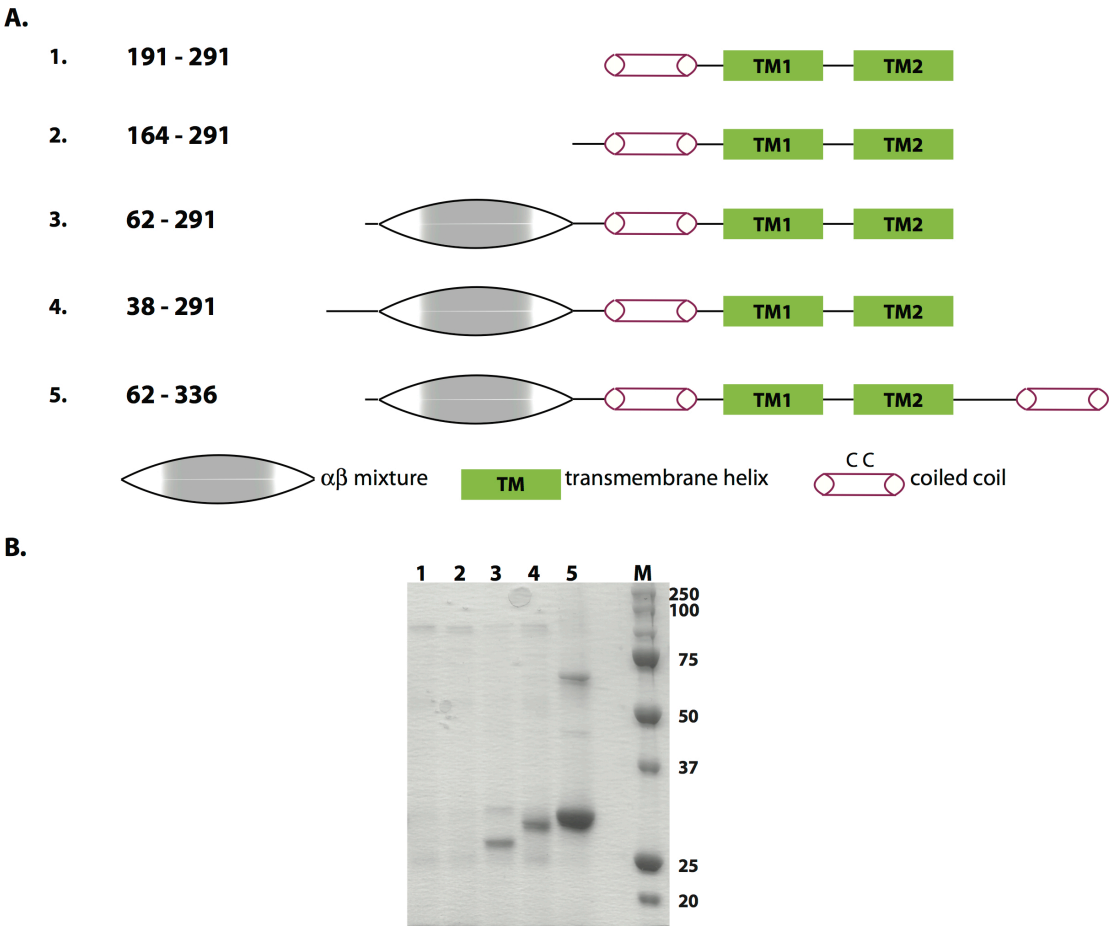

Figure 7.10 Design and expression test of MCU constructs for purification and crystallization

(A) The new constructs designed for purification and crystallization. These constructs had N-terminal or C-Terminal truncations and were expected to yield a more stable product. (B) Small-scale purification of the constructs. The lanes indicate the imidazole elution fraction from Talon Co^{2+} beads and the numbers on top of the lanes correspond to the construct numbering shown in A.

7.7 Large-scale purification of isoform 1 Δmts (62-336)

After optimizing the solubilization tests of the new Δmts construct of isoform 1 mcu, a large-scale purification was performed to get enough protein for crystallization experiments. 12 liters of 2*YT media was inoculated with the starter culture of *E. coli* transformed with the pET15b-C62-336 construct. Cells were grown at 37°C to an $O.D_{600}$ of 0.7. The temperature was then lowered to 30°C and protein expression was induced with 0.5mM IPTG for 4 hours.

Cells were harvested and the cell pellet was homogenized in 25mM HEPES and 200mM NaCl to a final volume of 150ml (approximately 4ml per gram of cell pellet) and frozen at -20°C. The thawing induces lysis of *E. coli* pLys cells. Afterwards, 50ml of 4X lysis buffer was added to result in a final concentration of 25mM HEPES pH 7.0, 200mM NaCl, 0.5mM TCEP, 10% Glycerol, protease inhibitor cocktail (EDTA free, Roche). To immediately digest the DNA, DNase was added, which leads to a less viscous solution. The cells were homogenized using a potter-douncer, filtered and passed three times through a microfluidizer at 60psi for complete lysis. The lysed cells were spun first at low speed (10,000g, 30 min, 4°C) to removes the cell debris and then at high speed (125,000g, 120 min, 4°C to isolate the membrane. The membranes were homogenized in 2X buffer containing 100mM HEPES, 400mM NaCl, 2mM TCEP and 20% Glycerol. The membrane concentration was estimated to be about 25mg/ml using the BCA assay. Aliquots of 20ml membrane fractions were snap frozen and stored at -80°C prior to purification.

Membranes were solubilized in 2% Fos-choline overnight at 4°C. The insoluble membrane material was removed by high-speed centrifugation (125,000g, 60min, 4°C). After adding imidazole to a final concentration of 10mM, the supernatant was incubated with pre-equilibrated Talon beads (binding buffer: 50mM HEPES, 200mM NaCl, 1mM TCEP, 10% glycerol, 0.2% F-12 and 10mM Imidazole). The column was then washed extensively with the binding buffer (at least 25 CV) and the protein was eluted in steps using binding buffer containing varying amounts of Imidazole (25mM, 50mM 150mM and 500mM). The elution fractions were run on an SDS gel (Fig 7.11A). Elution fractions corresponding to 50, 150 and 500mM Imidazole concentrations appeared pure and contained large amounts of the protein of interest. These fractions were pooled and concentrated. Since the protein is predicted to be a tetramer, which would be more than 140 kDa with the detergent micelle, a 100kDa cut-off centrifugal filter (vivaspin) was used. 500µl of the concentrated protein at 20mg/ml was injected onto a Superdex-200 Increase 10/300 column, which was pre-equilibriated with 25mM HEPES, 150mM NaCl, 1mM TCEP, 0.1% F-12. Unfortunately, the protein eluted mostly in the void volume (Fig 7.11B). Two smaller, overlapping peaks followed at 11 ml and 12 ml. It is possible that the

aggregation was caused due to the very high protein concentration injected onto the SEC column. In order to try to reverse the aggregation, the elution fractions were pooled and diluted 4-fold into the size exclusion buffer with excess salt and glycerol (500mM NaCl and 5% glycerol) and incubated for several hours. 500µl of this diluted sample was run on the Superdex 200 column. This process of dilution with a buffer containing high salt and glycerol failed to reverse the aggregation (Fig 7.11B inset).

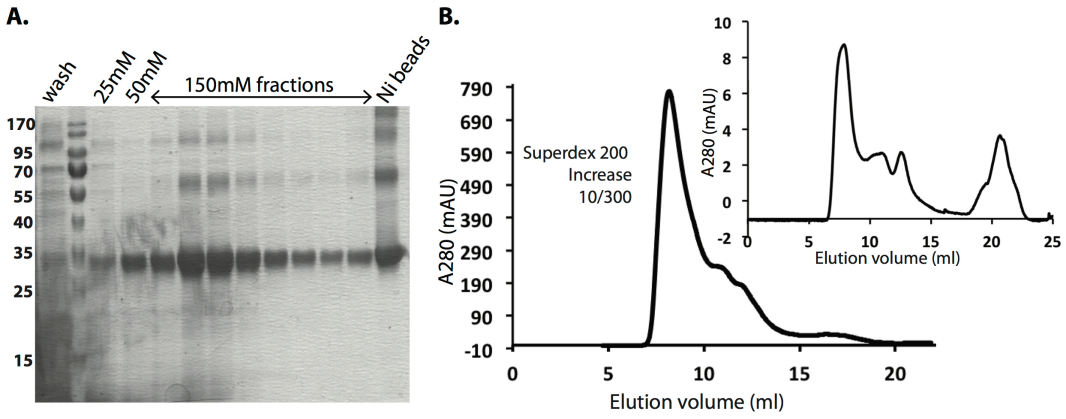

Figure 7.11 Purification of isoform 1 Δmts (62-336)

(A) Talon affinity purification showing imidazole elution. The protein molecular weight is 34.4 kDa with the His-tag (B) Gel filtration profile from a Superdex 200 Increase 10/300 column. The major peak is at 8.2ml. The inset shows the SEC profile of the eluted protein diluted and incubated for several hours in the presence of excess salt and glycerol.

Despite the non-homogeneity of the protein sample obtained, it was set up for crystallization screening. It is possible that the protein was undergoing ordered aggregation, which could aid in nucleation during the crystallization process.

To address the aggregation issue, a second purification was performed during which the eluted protein fractions after the affinity column step (Fig 7.12A) were only concentrated to about 5mg/ml (2ml). This sample was then injected onto a Superdex 200 16/60 column, which could provide a better separation of multiple peaks. The protein eluted in two major peaks (Fig 7.12B), where the first peak (elution volume: 42.8ml) corresponds to the void volume. The second peak (elution volume: 60.3 ml) corresponded to the predicted tetramer MCU. The fractions of the second peak

were pooled and concentrated in a 100kDa cut off centrifugal filter to 5mg/ml. The protein was then used for crystallization setups.

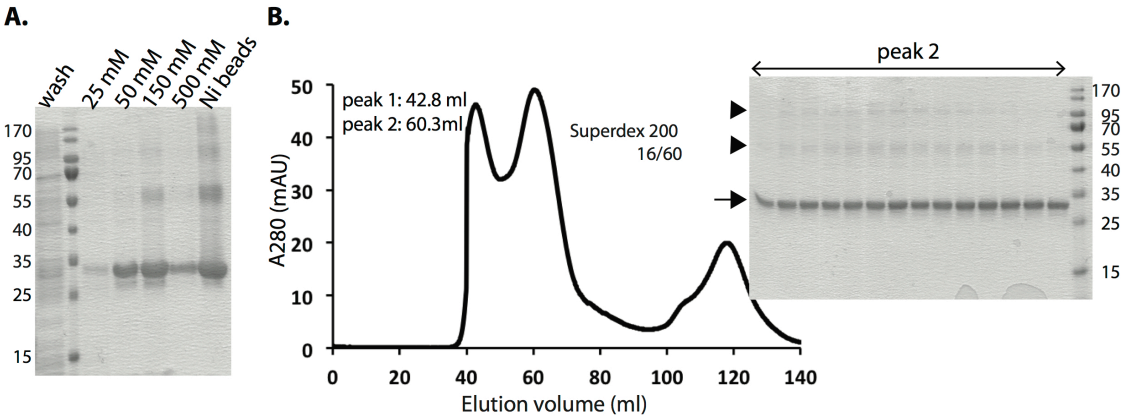

Figure 7.12 Optimized purification of isoform 1 Δmts (62-336)

(A) Talon affinity purification showing imidazole elution fractions. (B) Gel filtration profile from a Superdex 200 16/60 column. The elution volumes of the two major peaks are indicated. An SDS gel shows the fractions from peak2, which were pooled and concentrated for crystallization. The arrow points to the MCU monomer while the arrowheads could correspond to higher oligomers of the protein.

7.8 Crystallization of the mcu isoform 1 Δmts (62 – 336)

Initial crystallization trials were done in 96-well plates and hundreds of precipitants from the commercially available crystallization screens were tested. Most of the drops precipitated. This was expected given the fact that the protein was aggregating or rather prone to aggregation.

Interestingly, several small and big crystals appeared in these drops in a span of 4-8 weeks (Fig 7.13A). In order to confirm that these crystals were of MCU, a few crystals were fished, thoroughly washed in stabilizing solution, run on an SDS gel and subsequently silver stained. Purified mcu was run as a control (Fig 7.13B). The sample from washed crystals migrated at approximately 100 kDa (MCU construct size is 34.4 kDa with the tag) indicating that the crystals were formed by another protein that has co-purified with MCU.

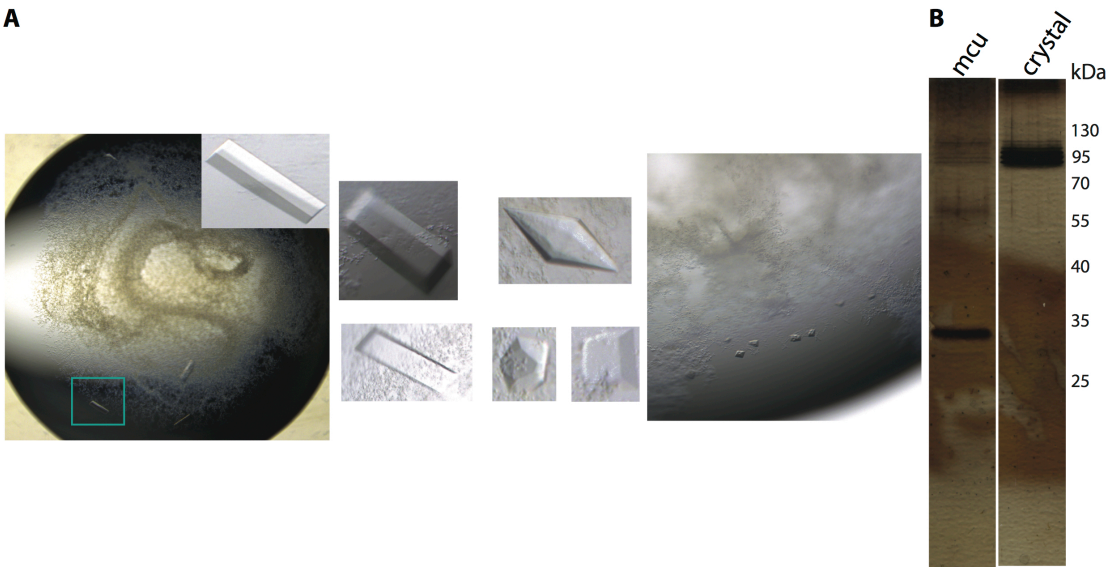

Figure 7.13 Crystallization trials of the purified isoform 1 Δmts (62-336)

(A) Crystals with various morphologies grew in a few conditions. (B) Silver staining of thoroughly washed and subsequently dissolved crystals show a band at approximately 100 kDa while purified mcu runs close to 35 kDa.

Nonetheless, diffraction data from these crystals were collected. Comparison of the space group and the unit cell constants of the crystals along with parameters available in the PDB database revealed that the impurity crystallized is most probably AcrB. AcrB is a common contaminant in membrane protein purifications when *E. coli* is used as expression host. It is known to crystallize easily even when present in minute quantities in the sample. Overall, it is obvious that purified MCU is not stable and is prone to aggregation. The expression system, solubilization and purification procedures of MCU have to be entirely revamped. More detergents and their combinations with lipids have to be tested in order to solubilize and stabilize MCU.

8 Discussion

8.1 Stabilizing mitochondrial calcium uniporter for structural studies

Due to their hydrophobic nature and intrinsic instability, membrane proteins are difficult to isolate and study. Structural studies on membrane proteins pose an even greater challenge, as it demands pure and correctly folded protein in milligram quantities. Therefore, optimizing the expression and purification of a membrane protein is crucial in obtaining its structural information. Attempts to express and purify the human Mitochondrial Calcium Uniporter (MCU) in this work led to the successful isolation of large quantities of the protein. But, it is evident from the elution profile of the Δmts constructs of MCU in size-exclusion chromatography (Results, Fig. 2.19 and Fig 2.20) that the obtained protein is to a large extent aggregated. Crystallization trials with this protein sample have so far been unsuccessful. For subsequent structural studies on MCU, it is imperative to further optimize the solubilization and purification procedure to obtain large quantities of correctly folded pure protein. Below, I discuss some of the strategies that could be tried to obtain stable MCU.

8.1.1 Expression host

A major bottleneck in studying a membrane protein is difficulty in overexpressing them recombinantly. Membrane proteins that were the forerunners in having their structures determined are the ones that occur abundantly in the native membrane (Tate, 2001). These include bacteriorhodopsin (Henderson & Unwin, 1975) (Luecke *et al*, 1999), photosynthetic reactions centre (Deisenhofer *et al*, 1985), H^+-ATPase (Kühlbrandt *et al*, 1998), F1Fo-ATPase (Stock *et al*, 1999), aquaporin (Murata *et al*, 2000), G protein-coupled receptor rhodopsin (Palczewski *et al*, 2000), Ca^{2+}-ATPase (Toyoshima *et al*, 2000). Abundance in the native source circumvents the need to

establish an expression system and ensures the preservation of the protein's functional fold during isolation. However most integral membrane proteins occur in low copy numbers in cells (He *et al*, 2014), which make their isolation from the native source difficult. Some eukaryotic membrane protein structures like the voltage-dependent potassium channels have been obtained by expressing the proteins in heterologous expression systems like baculovirus-infected insect cells (Long *et al*, 2005). Among the recombinantly expressed eukaryotic proteins that yielded structural information, five were expressed in *E. coli*, 20 in yeast, 35 in insect cells and three in mammalian cells (He *et al*, 2014). Out of the five eukaryotic proteins recombinantly expressed in *E. coli*, two are mammalian membrane proteins. One is a human 5-lipoxygenase-Activating Protein whose structure was solved by X-ray crystallography (Ferguson *et al*, 2007). The other protein is the mouse mitochondrial uncoupling protein 2 (UCP2) whose structure was determined using Nuclear magnetic resonance (NMR) spectroscopy (Berardi *et al*, 2011).

The low success rate of eukaryotic membrane protein expression in bacteria is attributed to different t-RNA codon usage, the lack of essential lipids and molecular chaperons that aid in protein folding. In addition, post-translational modifications that are required for correct membrane insertion, folding and function of the protein are also absent in *E. coli* (He *et al*, 2014). Interestingly, the results presented in this thesis show that the human MCU gene could be expressed very well in *E. coli.* This could be attributed to the *E. coli* codon optimization done on the MCU gene. In addition to being expressed, MCU protein was successfully incorporated into the *E. coli* plasma membrane. This is typically a bottleneck in the case of majority of mammalian membrane proteins expressed in *E. coli*. One of the reasons for large amounts of overexpressed MCU getting incorporated into the *E. coli* membrane may be the similarity in the lipid composition of *E. coli* plasma membrane and the inner mitochondrial membrane (Osman *et al*, 2011). Although the initial MCU constructs overexpressed in *E. coli* showed degradation, expression of a new construct spanning residues 62 to 336, which was designed considering the secondary structure prediction information and mass spectrometry data, yielded a stable MCU product. However, the purified MCU showed signs of aggregation/misfolding.

Therefore, an alternate eukaryotic expression host might help overcome this problem. However, there are several alternate strategies that could be tested to stabilize the MCU expressed in *E. coli*. Those strategies are described below.

8.1.2 Detergent/lipid screening

Solubilization tests on various constructs containing the membrane-spanning domain identified the lipid like detergent foscholine-12 to be the most efficient in extracting MCU from the *E. coli* membrane. Foscholine is known to be a "harsh" detergent due to its zwitterionic head group. It solubilizes most proteins from the membrane presumably by denaturing. However, Foscholine had been successfully used in extracting proteins like the human vomeronasal type 1 receptor 1 (Corin *et al*, 2011) and a bacterial homologue of the calcium-cation antiporter CAX^{CK31} (Ridilla *et al*, 2012). Both proteins were obtained in a fully functional and correctly folded state. The crystal structure of the *E. coli* mechanosensitive channel MscS was obtained by using Fos-14 for solubilizing the protein from the membrane and during the purification procedure (Bass *et al*, 2002) (Wang *et al*, 2008). Foscholine-12 has also been successfully used for the extraction of outer membrane proteins like OmpF (Outer membrane protein F) (Kefala *et al*, 2010), whose structure was solved using X-ray crystallography. Other examples of Foscholine-12 extracted proteins include PagP (PhoPQ activated outer membrane enzyme) (Hwang *et al*, 2002) and human phospholamban (Oxenoid & Chou, 2005). The structures of these two proteins were determined using NMR spectroscopy. Fos-12 has also been shown to be important for the refolding of misfolded Diacyl glycerol kinase (Gorzelle *et al*, 1999).

In one of the purifications of MCU 62-336 using Fos-12, the proteins did not elute in the void volume during size-exclusion chromatography (Fig 8.1). It is noteworthy that the amount of protein used in this case was substantially lower when compared to the other size-exclusion chromatography runs where majority of the proteins eluted in the void volume (Results, Fig 7.11B). It is possible that Fos-12 does not denature

MCU but the tendency of the protein to aggregate depends on the protein concentration, which could be controlled by fine-tuning the purification conditions.

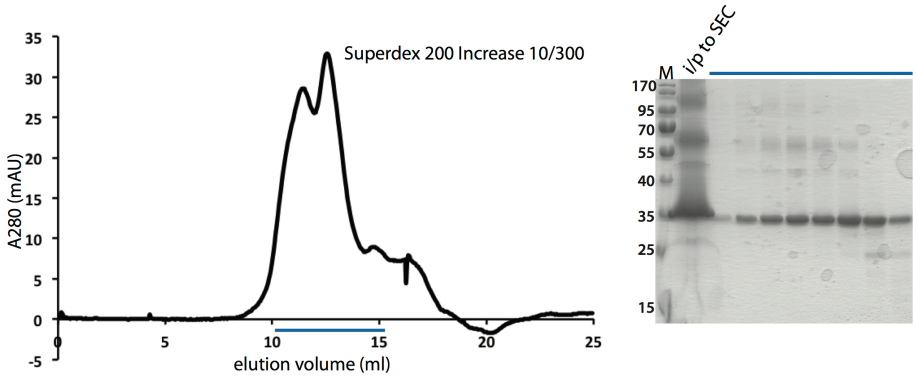

Figure 8.1 Elution profile of Δmts (62-336) at low protein concentrations

Size exclusion chromatography profile of mcu 62-336 from a Superdex 200 Increase 10/300 column. There are two peaks at elution volumes corresponding to 11.5 and 12.5 ml. The blue line indicates the elution fractions run on an SDS gel. i/p to SEC denotes the protein injected onto the size exclusion column.

Nevertheless, it is important to identify conditions in which the protein is stable at even higher concentrations that are required for crystallization. Towards this direction, two lipids/lipid-like molecules were used as additives in combination with detergents to test the effect on solubilizing MCU. These include cholesteryl hemisuccinate (CHS, generally used as a substitute for cholesterol) and cardiolipin (CL, a lipid usually found in the inner mitochondrial membrane where MCU is localized).

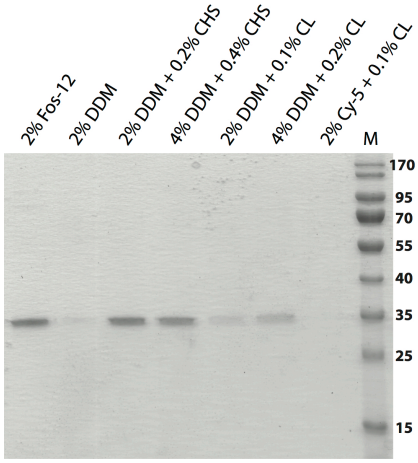

Figure 8.2 Solubilization tests of Δmts (62-336) using detergent/ lipid combinations
Various detergents and combination of detergents with lipids/ lipid like molecules were used.

The amount of Δmts (62-336) solubilized by 2% DDM in combination with 0.2% CHS is comparable to that of Fos-12 and is significantly higher than the amount of solubilized Δmts obtained using only 2% DDM (Fig 2.23). Although, CL in combination with Cy-5 (Cymal-5) did not solubilize Δmts, CL in combination with DDM was successful. From this experiment, CHS in combination with DDM appeared to be the most efficient in solubilizing MCU. Hence this was used in large-scale Δmts purification. Unfortunately, purification of Δmts (62-336) using a combination of DDM and CHS led to the protein eluting in the void volume of both Superdex 200 and Superose 6 columns (Fig 8.3).

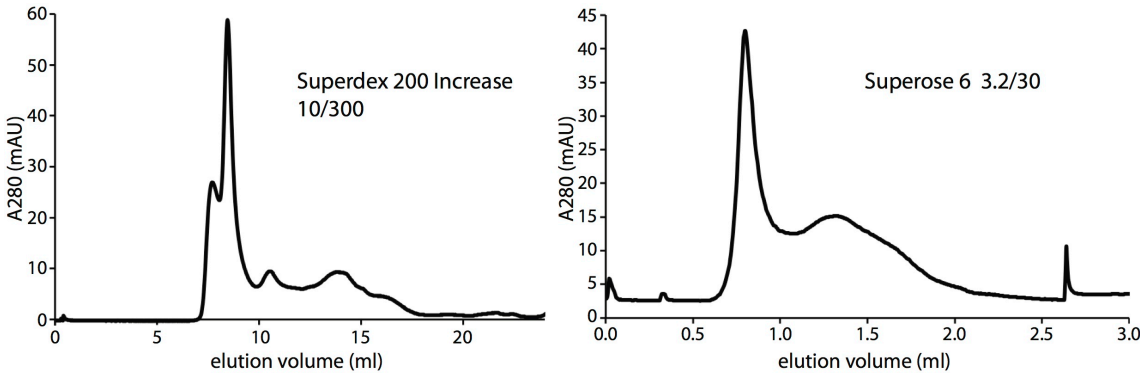

Figure 8.3 Size-exclusion chromatography profile of Δmts (62-336) in DDM-CHS

Size exclusion chromatography profile of DDM-CHS solubilized mcu 62-336 from a Superdex 200 Increase 10/300 column and Superose 6 3.2/30 column. Majority of the protein elutes in the void volumes of both the columns.

A large number of conditions including buffers and detergents need to be tested to optimize the MCU protein purification. For this purpose, GFP tagged MCU may be expressed in *E. coli* and a large number of conditions can be screened to isolate it from the membrane. The elution profile (monitored by GFP fluorescence) of the solubilized protein on a size-exclusion chromatography can be used to identify the conditions in which the protein is homogenous and non-aggregated. This circumvents the need for a long purification procedure for each of the conditions to be tested and thus allows large-scale screening.

8.1.3 Stabilizing MCU by adding other components of the uniporter complex

Another way of increasing the stability of MCU is by co-expressing it with its potential interacting partners in the mitochondrial uniporter complex. However, most of the interaction data obtained so far on the complex is based on co-immunoprecipitation studies, which do not necessarily indicate direct protein-protein interactions. Interestingly, a recent study has shown that the human MCU heterologously expressed in yeast needs the presence of EMRE to act as a functional channel (Kovács-Bogdán *et al*, 2014). This makes MCU-EMRE the core unit of the uniporter complex that is indispensable for Ca^{2+} uptake. Given that the effect of EMRE on MCU was shown in an organism lacking the uniporter complex, the direct interaction between MCU and EMRE is very likely. Co-expressing MCU and EMRE could lead to a more stable heterodimer that is suitable for crystallization studies and structure determination.

8.2 Electron microscopy of the mitochondrial uniporter complex

Recent advancements in cryo-electron microscopy (cryo-EM) have made it possible to obtain high-resolution structures of complex molecules (Kühlbrandt, 2014a) (Kühlbrandt, 2014b). For example, the new direct electron detectors and image processing software have enabled solving the structure of a small, asymmetric complex like γ-secretase (Lu *et al*, 2014) with a molecular weight of only 170 kDa. The uniporter itself could prove to be too small to be detected in cryo-EM since even as a predicted tetramer, its molecular weight is about 140 kDa. However, the MCU-EMRE complex, depending on the stoichiometry of the MCU-EMRE association, could be an interesting target for EM study.

Another exciting front of this project is to obtain structural information on the whole uniporter complex constituted by MCU, MCUb, EMRE, MICU1 and MICU2. The complex is expected to be about ~480 kDa according to the native PAGE analysis of the isolated complex (Sancak *et al*, 2013), which makes it a good candidate for single particle cryo-EM. Towards this end the uniporter complex has to be isolated from native sources that are enriched in mitochondria like bovine brain, liver and heart. One probable way of isolating the complex is to subject the isolated inner mitochondrial membrane fraction to a linear sucrose gradient centrifugation and probe the resulting fractions for MCU using a monoclonal antibody. Several ranges of linear and step gradients have to be tried to arrive at the optimal procedure for the isolation of the mitochondrial uniporter complex. Another method would be to overexpress all the components of this complex in yeast or insect cells with an affinity tag on one of the component proteins. The whole mitochondrial calcium uniporter complex has been successfully isolated by stable expression of MCU-FLAG in HEK-293T cells followed by affinity purification (Sancak *et al*, 2013). This approach has been successfully performed for γ-secretase (Lu *et al*, 2014) where different components of the γ-secretase (all differently tagged) were co-expressed from a single vector in HEK-293F cells. Once homogenous uniporter complex is obtained, it would be exciting and challenging to do the structural characterization by cryo-EM.

9 References

Bass RB, Strop P, Barclay M & Rees DC (2002) Crystal structure of Escherichia coli MscS, a voltage-modulated and mechanosensitive channel. *Science* **298:** 1582–1587

Baughman JM, Perocchi F, Girgis HS, Plovanich M, Belcher-Timme CA, Sancak Y, Bao XR, Strittmatter L, Goldberger O, Bogorad RL, Koteliansky V & Mootha VK (2011) Integrative genomics identifies MCU as an essential component of the mitochondrial calcium uniporter. *Nature* **476:** 341–345

Berardi MJ, Shih WM, Harrison SC & Chou JJ (2011) Mitochondrial uncoupling protein 2 structure determined by NMR molecular fragment searching. *Nature* **476:** 109–113

Berk A, Krieger M, Darnell J & Lodish H (2003) Mcgill Lodish 5e Package - Molecular Cell Biology + Mcgill Activation Code W H Freeman & Company

Biegert A, Mayer C, Remmert M, Söding J & Lupas AN (2006) The MPI Bioinformatics Toolkit for protein sequence analysis. *Nucleic Acids Res.* **34:** W335–9

Boudker O & Verdon G (2010) Structural perspectives on secondary active transporters. *Trends Pharmacol. Sci.* **31:** 418–426

Boudker O, Ryan RM, Yernool D, Shimamoto K & Gouaux E (2007) Coupling substrate and ion binding to extracellular gate of a sodium-dependent aspartate transporter. *Nature* **445:** 387–393

Caplan DA, Subbotina JO & Noskov SY (2008) Molecular mechanism of ion-ion and ion-substrate coupling in the Na+-dependent leucine transporter LeuT. *Biophysical Journal* **95:** 4613–4621

Carafoli E (2012) The interplay of mitochondria with calcium: an historical appraisal. *Cell Calcium* **52:** 1–8

Chaudhuri D, Sancak Y, Mootha VK & Clapham DE (2013) MCU encodes the pore conducting mitochondrial calcium currents. *Elife* **2:** e00704

Clapham DE (1995) Calcium signaling. *Cell* **80:** 259–268

Clapham DE (2007) Calcium signaling. *Cell* **131:** 1047–1058

Corin K, Baaske P, Geissler S, Wienken CJ, Duhr S, Braun D & Zhang S (2011) Structure and function analyses of the purified GPCR human vomeronasal type 1 receptor 1. *Sci Rep* **1:** 172

Csordás G, Golenár T, Seifert EL, Kamer KJ, Sancak Y, Perocchi F, Moffat C, Weaver D, la Fuente Perez de S, Bogorad R, Koteliansky V, Adijanto J, Mootha VK &

Hajnóczky G (2013) MICU1 controls both the threshold and cooperative activation of the mitochondrial Ca^{2+} uniporter. *Cell Metab.* **17:** 976–987

De Stefani D, Raffaello A, Teardo E, Szabò I & Rizzuto R (2011) A forty-kilodalton protein of the inner membrane is the mitochondrial calcium uniporter. *Nature* **476:** 336–340

Deisenhofer J, Epp O, Miki K, Huber R & Michel H (1985) Structure of the protein subunits in the photosynthetic reaction centre of Rhodopseudomonas viridis at 3Å resolution. *Nature* **318:** 618–624

Denton RM, Randle PJ & Martin BR (1972) Stimulation by calcium ions of pyruvate dehydrogenase phosphate phosphatase. *Biochem. J.* **128:** 161–163

Doyle DA, Cabral JM, Pfuetzner RA, Kuo AL, Gulbis JM, Cohen SL, Chait BT & MacKinnon R (1998) The structure of the potassium channel: Molecular basis of K+ conduction and selectivity. *Science* **280:** 69–77

Eichler K, Bourgis F, Buchet A, Kleber HP & Mandrand-Berthelot MA (1994) Molecular characterization of the cai operon necessary for carnitine metabolism in Escherichia coli. *Molecular Microbiology* **13:** 775–786

Eichler K, Buchet A, Bourgis F, Kleber HP & Mandrand-Berthelot MA (1995) The fix Escherichia coli region contains four genes related to carnitine metabolism. *J. Basic Microbiol.* **35:** 217–227

Engel A & Gaub HE (2008) Structure and mechanics of membrane proteins. *Annu. Rev. Biochem.* **77:** 127–148

Eswar N, Eramian D, Webb B, Shen M-Y & Sali A (2008) Protein Structure Modeling with MODELLER. In *Structural Proteomics* pp 145–159. Totowa, NJ: Humana Press

Faham S, Watanabe A, Besserer GM & Cascio D (2008) The Crystal Structure of a Sodium Galactose Transporter Reveals Mechanistic Insights into Na+/Sugar Symport. *Science*

Farwick M, Siewe RM & Krämer R (1995) Glycine betaine uptake after hyperosmotic shift in Corynebacterium glutamicum. *J. Bacteriol.* **177:** 4690–4695

Fehr M, Takanaga H, Ehrhardt DW & Frommer WB (2005) Evidence for high-cavacity bidirectional glucose transport across the endoplasmic reticulum membrane by genetically encoded fluorescence resonance energy transfer nanosensors. *Mol. Cell. Biol.* **25:** 11102–11112

Ferguson AD, McKeever BM, Xu S, Wisniewski D, Miller DK, Yamin T-T, Spencer RH, Chu L, Ujjainwalla F, Cunningham BR, Evans JF & Becker JW (2007) Crystal structure of inhibitor-bound human 5-lipoxygenase-activating protein. *Science* **317:** 510–512

Fieni F, Lee SB, Jan YN & Kirichok Y (2012) Activity of the mitochondrial calcium uniporter varies greatly between tissues. *Nat Commun* **3:** 1317

Forrest LR & Rudnick G (2009) The Rocking Bundle: A Mechanism for Ion-Coupled Solute Flux by Symmetrical Transporters. *Physiology* **24:** 377–386

Gadsby DC, Takeuchi A, Artigas P & Reyes N (2009) Review. Peering into an ATPase ion pump with single-channel recordings. *Philos. Trans. R. Soc. Lond., B, Biol. Sci.* **364:** 229–238

Gao X, Zhou L, Jiao X, Lu F, Yan C, Zeng X, Wang J & Shi Y (2010) Mechanism of substrate recognition and transport by an amino acid antiporter. *Nature* **463:** 828–832

Gong S, Richard H & Foster JW (2003) YjdE (AdiC) Is the Arginine:Agmatine Antiporter Essential for Arginine-Dependent Acid Resistance in Escherichia coli. *J. Bacteriol.*

Gorzelle BM, Nagy JK, Oxenoid K, Lonzer WL, Cafiso DS & Sanders CR (1999) Reconstitutive refolding of diacylglycerol kinase, an integral membrane protein. *Biochemistry* **38:** 16373–16382

H F DeLuca GWE (1961) CALCIUM UPTAKE BY RAT KIDNEY MITOCHONDRIA. *Proc. Natl. Acad. Sci. U.S.A.* **47:** 1744

Hajnóczky G, Robb-Gaspers LD, Seitz MB & Thomas AP (1995) Decoding of cytosolic calcium oscillations in the mitochondria. *Cell* **82:** 415–424

He Y, Wang K & Yan N (2014) The recombinant expression systems for structure determination of eukaryotic membrane proteins. *Protein Cell* **5:** 658–672

Henderson R & Unwin PN (1975) Three-dimensional model of purple membrane obtained by electron microscopy. *Nature* **257:** 28–32

Hoffman NE, Chandramoorthy HC, Shamugapriya S, Zhang X, Rajan S, Mallilankaraman K, Gandhirajan RK, Vagnozzi RJ, Ferrer LM, Sreekrishnanilayam K, Natarajaseenivasan K, Vallem S, Force T, Choi ET, Cheung JY & Madesh M (2013) MICU1 motifs define mitochondrial calcium uniporter binding and activity. *Cell Rep* **5:** 1576–1588

Holm L & Rosenström P (2010) Dali server: conservation mapping in 3D. *Nucleic Acids Res.*

Huang Y, Lemieux MJ, Song J, Auer M & Wang DN (2003) Structure and Mechanism of the Glycerol-3-Phosphate Transporter from Escherichia coli. *Science*

Hwang PM, Choy W-Y, Lo EI, Chen L, Forman-Kay JD, Raetz CRH, Privé GG, Bishop RE & Kay LE (2002) Solution structure and dynamics of the outer membrane enzyme PagP by NMR. *Proc. Natl. Acad. Sci. U.S.A.* **99:** 13560–13565

Iyer R, Iverson TM, Accardi A & Miller C (2002) A biological role for prokaryotic ClC chloride channels. *Nature* **419:** 715–718

Jardetzky O (1966) Simple allosteric model for membrane pumps. *Nature* **211:** 969–970

Jouaville LS, Pinton P, Bastianutto C, Rutter GA & RIZZUTO R (1999) Regulation of mitochondrial ATP synthesis by calcium: evidence for a long-term metabolic priming. *Proc. Natl. Acad. Sci. U.S.A.* **96:** 13807–13812

Jung H (2002) CaiT of Escherichia coli, a New Transporter Catalyzing L-Carnitine/gamma -Butyrobetaine Exchange. *Journal of Biological Chemistry* **277:** 39251–39258

Jung H, Jung K & Kleber HP (1990) L-carnitine metabolization and osmotic stress response in Escherichia coli. *J. Basic Microbiol.* **30:** 409–413

Kabsch W (2010) XDS. *Acta Crystallogr D Biol Crystallogr* **66:** 125–132

Kalayil S, Schulze S & Kühlbrandt W (2013) Arginine oscillation explains Na+ independence in the substrate/product antiporter CaiT. *Proceedings of the National Academy of Sciences* **110:** 17296–17301

Kamer KJ & Mootha VK (2014) MICU1 and MICU2 play nonredundant roles in the regulation of the mitochondrial calcium uniporter. *EMBO Rep* **15:** 299–307

Kantcheva AK, Quick M, Shi L, Winther A-ML, Stolzenberg S, Weinstein H, Javitch JA & Nissen P (2013) Chloride binding site of neurotransmitter sodium symporters. *Proceedings of the National Academy of Sciences*

Kefala G, Ahn C, Krupa M, Esquivies L, Maslennikov I, Kwiatkowski W & Choe S (2010) Structures of the OmpF porin crystallized in the presence of foscholine-12. *Protein Sci.* **19:** 1117–1125

Khafizov K, Perez C, Koshy C, Quick M, Fendler K, Ziegler C & Forrest LR (2012) Investigation of the sodium-binding sites in the sodium-coupled betaine transporter BetP

. *PNAS***:** 1–10

Kirichok Y, Krapivinsky G & Clapham DE (2004) The mitochondrial calcium uniporter is a highly selective ion channel. *Nature* **427:** 360–364

Klingenberg M & Martonosi AN (1976) Klingenberg: The Enzymes of Biological Membranes:... - Google Scholar. *Vol 3Plenum*

Kovács-Bogdán E, Sancak Y, Kamer KJ, Plovanich M, Jambhekar A, Huber RJ, Myre MA, Blower MD & Mootha VK (2014) Reconstitution of the mitochondrial calcium uniporter in yeast. *Proceedings of the National Academy of Sciences* **111:** 8985–8990

Kowalczyk L, Ratera M, Paladino A, Bartoccioni P, Errasti-Murugarren E, Valencia E, Portella G, Bial S, Zorzano A, Fita I, Orozco M, Carpena X, Vazquez-Ibar JL & Palacin M (2011) Molecular basis of substrate-induced permeation by an amino acid antiporter. *Proceedings of the National Academy of Sciences* **108:** 3935–3940

Krishnamurthy H & Gouaux E (2012) X-ray structures of LeuT in substrate-free outward-open and apo inward-open states. *Nature***:** 1–8

Krishnamurthy H, Piscitelli CL & Gouaux E (2009) Unlocking the molecular secrets of sodium-coupled transporters. *Nature* **459:** 347–355

Krissinel E & Henrick K (2004) Secondary-structure matching (SSM), a new tool for fast protein structure alignment in three dimensions. *Acta Crystallogr D Biol Crystallogr* **60:** 2256–2268

Krogh A, Larsson B, Heijne von G & Sonnhammer E (2001) Predicting transmembrane protein topology with a hidden Markov model: Application to complete genomes. *Journal of Molecular Biology* **305:** 567–580

Kühlbrandt W (2014a) Cryo-EM enters a new era. *Elife* **3:** e03678

Kühlbrandt W (2014b) Biochemistry. The resolution revolution. *Science* **343:** 1443–1444

Kühlbrandt W, Auer M & Scarborough GA (1998) Three-dimensional map of the plasma membrane H: +: -ATPase in the open conformation : Abstract : Nature. *Nature* **392:** 840–843

Li H, Robertson AD & Jensen JH (2005) Very fast empirical prediction and rationalization of protein pKa values. *Proteins* **61:** 704–721

Li J & Tajkhorshid E (2009) Ion-releasing state of a secondary membrane transporter. *Biophysical Journal* **97:** L29–31

Long SB, Campbell EB & MacKinnon R (2005) Crystal structure of a mammalian voltage-dependent Shaker family K+ channel. *Science* **309:** 897–903

Lu P, Bai X-C, Ma D, Xie T, Yan C, Sun L, Yang G, Zhao Y, Zhou R, Scheres SHW & Shi Y (2014) Three-dimensional structure of human γ-secretase. *Nature* **512:** 166–170

Luecke H, Schobert B, Richter HT, Cartailler JP & Lanyi JK (1999) Structure of bacteriorhodopsin at 1.55 A resolution. *Journal of Molecular Biology* **291:** 899–911

Mallilankaraman K, Doonan P, Cárdenas C, Chandramoorthy HC, Müller M, Miller R, Hoffman NE, Gandhirajan RK, Molgó J, Birnbaum MJ, Rothberg BS, Mak D-OD, Foskett JK & Madesh M (2012) MICU1 is an essential gatekeeper for MCU-mediated mitochondrial Ca(2+) uptake that regulates cell survival. *Cell* **151:** 630–644

Martell JD, Deerinck TJ, Sancak Y, Poulos TL, Mootha VK, Sosinsky GE, Ellisman MH & Ting AY (2012) Engineered ascorbate peroxidase as a genetically encoded reporter for electron microscopy. *Nat. Biotechnol.* **30:** 1143–1148

McCormack JG, Halestrap AP & Denton RM (1990) Role of calcium ions in regulation of mammalian intramitochondrial metabolism. *Physiol. Rev.* **70:** 391–425

MITCHELL P (1966) CHEMIOSMOTIC COUPLING IN OXIDATIVE AND PHOTOSYNTHETIC PHOSPHORYLATION. *Biological Reviews* **41:** 445–501

Murata K, Mitsuoka K, Hirai T, Walz T, Agre P, Heymann JB, Engel A & Fujiyoshi Y (2000) Structural determinants of water permeation through aquaporin-1. *Nature* **407:** 599–605

Osman C, Voelker DR & Langer T (2011) Making heads or tails of phospholipids in mitochondria. *J. Cell Biol.* **192:** 7–16

Ota T, Suzuki Y, Nishikawa T, Otsuki T, Sugiyama T, Irie R, Wakamatsu A, Hayashi K, Sato H, Nagai K, Kimura K, Makita H, Sekine M, Obayashi M, Nishi T, Shibahara T, Tanaka T, Ishii S, Yamamoto J-I, Saito K, et al (2004) Complete sequencing and characterization of 21,243 full-length human cDNAs. *Nat. Genet.* **36:** 40–45

Overington JP, Al-Lazikani B & Hopkins AL (2006) Opinion - How many drug targets are there? *Nat Rev Drug Discov* **5:** 993–996

Oxenoid K & Chou JJ (2005) The structure of phospholamban pentamer reveals a channel-like architecture in membranes. *Proc. Natl. Acad. Sci. U.S.A.* **102:** 10870–10875

Palczewski K, Kumasaka T, Hori T, Behnke CA, Motoshima H, Fox BA, Le Trong I, Teller DC, Okada T, Stenkamp RE, Yamamoto M & Miyano M (2000) Crystal structure of rhodopsin: A G protein-coupled receptor. *Science* **289:** 739–745

Patron M, Checchetto V, Raffaello A, Teardo E, Vecellio Reane D, Mantoan M, Granatiero V, Szabò I, De Stefani D & Rizzuto R (2014) MICU1 and MICU2 Finely Tune the Mitochondrial Ca2+ Uniporter by Exerting Opposite Effects on MCU Activity. *Molecular Cell* **53:** 726–737

Perez C, Faust B, Mehdipour AR, Francesconi KA, Forrest LR & Ziegler C (2014) Substrate-bound outward-open state of the betaine transporter BetP provides insights into Na+ coupling. *Nat Commun* **5:**

Perez C, Koshy C, Ressl S, Nicklisch S, mer RKA & Ziegler C (2011) Substrate specificity and ion coupling in the Na+/betaine symporter BetP. *The EMBO Journal***:** 1–9

Perez C, Koshy C, Yildiz Ö & Ziegler C (2012) Alternating-access mechanism in conformationally asymmetric trimers of the betaine transporter BetP. *Nature* **490:** 126–130

Perocchi F, Gohil VM, Girgis HS, Bao XR, McCombs JE, Palmer AE & Mootha VK (2010) MICU1 encodes a mitochondrial EF hand protein required for Ca2+ uptake. *Nature* **467:** 291–296

Petersen OH, Michalak M & Verkhratsky A (2005) Calcium signalling: Past, present and future. *Cell Calcium*

Pietrobon D, Di Virgilio F & POZZAN T (1990) Structural and functional aspects of calcium homeostasis in eukaryotic cells. *Eur. J. Biochem.* **193:** 599–622

Piscitelli CL, Krishnamurthy H & Gouaux E (2010) Neurotransmitter/sodium symporter orthologue LeuT has a single high-affinity substrate site. *Nature* **468:** 1129–1132

Plovanich M, Bogorad RL, Sancak Y, Kamer KJ, Strittmatter L, Li AA, Girgis HS, Kuchimanchi S, De Groot J, Speciner L, Taneja N, Oshea J, Koteliansky V & Mootha VK (2013) MICU2, a paralog of MICU1, resides within the mitochondrial uniporter complex to regulate calcium handling. *PLoS ONE* **8:** e55785

Quick M, Shi L, Zehnpfennig B, Weinstein H & Javitch JA (2012) Experimental conditions can obscure the second high-affinity site in LeuT. *Nature Publishing Group* **19:** 207–211

Racher KI, Voegele RT, Marshall EV, Culham DE, Wood JM, Jung H, Bacon M, Cairns MT, Ferguson SM, Liang WJ, Henderson PJ, White G & Hallett FR (1999) Purification and reconstitution of an osmosensor: transporter ProP of Escherichia coli senses and responds to osmotic shifts. *Biochemistry* **38:** 1676–1684

Raffaello A, De Stefani D, Sabbadin D, Teardo E, Merli G, Picard A, Checchetto V, Moro S, Szabò I & Rizzuto R (2013) The mitochondrial calcium uniporter is a multimer that can include a dominant-negative pore-forming subunit. *The EMBO Journal* **32:** 2362–2376

Reddy VS, Shlykov MA, Castillo R, Sun EI & Saier MH (2012) The major facilitator superfamily (MFS) revisited. *FEBS J.* **279:** 2022–2035

Reig N, del Rio C, Casagrande F, Ratera M, Gelpi JL, Torrents D, Henderson PJF, Xie H, Baldwin SA, Zorzano A, Fotiadis D & Palacin M (2007) Functional and Structural Characterization of the First Prokaryotic Member of the L-Amino Acid Transporter (LAT) Family: A MODEL FOR APC TRANSPORTERS. *Journal of Biological Chemistry* **282:** 13270–13281

Ressl S, van Scheltinga ACT, Vonrhein C, Ott V & Ziegler C (2009) Molecular basis of transport and regulation in the Na+/betaine symporter BetP. *Nature* **457:** 47–52

Reyes N, Ginter C & Boudker O (2009) Transport mechanism of a bacterial homologue of glutamate transporters. *Nature* **462:** 880–885

Ridilla M, Narayanan A, Bolin JT & Yernool DA (2012) Identification of the dimer interface of a bacterial Ca(2+)/H(+) antiporter. *Biochemistry* **51:** 9603–9611

Ringer S (1882a) Regarding the action of hydrate of soda, hydrate of ammonia, and hydrate of potash on the ventricle of the frog's heart. *The Journal of physiology*

Ringer S (1882b) Concerning the influence exerted by each of the constituents of the blood on the contraction of the ventricle. *The Journal of physiology*

Ringer S (1883a) A third contribution regarding the influence of the inorganic constituents of the blood on the ventricular contraction. *The Journal of physiology*

Ringer S (1883b) A further contribution regarding the influence of the different constituents of the blood on the contraction of the heart. *The Journal of physiology*

RIZZUTO R, BRINI M, MURGIA M & POZZAN T (1993) Microdomains with High Ca2+ Close to Ip(3)-Sensitive Channels That Are Sensed by Neighboring Mitochondria. *Science* **262:** 744–747

Rizzuto R, De Stefani D, Raffaello A & Mammucari C (2012) Mitochondria as sensors and regulators of calcium signalling. *Nat. Rev. Mol. Cell Biol.* **13:** 566–578

RIZZUTO R, SIMPSON A, BRINI M & POZZAN T (1992) Rapid Changes of Mitochondrial Ca2+ Revealed by Specifically Targeted Recombinant Aequorin (Nature, Vol 358, Pg 325, 1992). *Nature* **360:** 768–768

Rübenhagen R (2001) The osmoreactive betaine carrier BetP from Corynebacterium glutamicum is a sensor for cytoplasmic K. *The EMBO Journal* **20:** 5412–5420

Rübenhagen R, Rönsch H, Jung H, Krämer R & Morbach S (2000) Osmosensor and osmoregulator properties of the betaine carrier BetP from Corynebacterium glutamicum in proteoliposomes.

Saier MH (2000) A Functional-Phylogenetic Classification System for Transmembrane Solute Transporters. *Microbiology and Molecular Biology Reviews* **64:** 354–411

Saier MH, Reddy VS, Tamang DG & Västermark A (2014) The transporter classification database. *Nucleic Acids Res.* **42:** D251–8

Sancak Y, Markhard AL, Kitami T, Kovács-Bogdán E, Kamer KJ, Udeshi ND, Carr SA, Chaudhuri D, Clapham DE, Li AA, Calvo SE, Goldberger O & Mootha VK (2013) EMRE is an essential component of the mitochondrial calcium uniporter complex. *Science* **342:** 1379–1382

Sanders CR & Myers JK (2004) Disease-related misassembly of membrane proteins. *Annu Rev Biophys Biomol Struct* **33:** 25–51

Sasaki J, Brown LS, Chon YS, Kandori H, Maeda A, Needleman R & Lanyi JK (1995)

Conversion of bacteriorhodopsin into a chloride ion pump. *Science* **269:** 73–75

SCARPA A & Azzone GF (1970) The mechanism of ion translocation in mitochondria. 4. Coupling of K+ efflux with Ca2+ uptake. *Eur. J. Biochem.* **12:** 328–335

SCARPA A & P G (1973) Mechanisms for Intracellular Calcium Regulation in Heart .1. Stopped-Flow Measurements of Ca++ Uptake by Cardiac Mitochondria. *J. Gen. Physiol.* **62:** 756–772

Schulze S (2011) Structural basis of Na. *Dissertation- PhD***:** 1–251

Schulze S, Köster S, Geldmacher U, van Scheltinga ACT & Kühlbrandt W (2010) Structural basis of Na+-independent and cooperative substrate/product antiport in CaiT. *Nature* **467:** 233–236

Selwyn MJ, Dawson AP & Dunnett SJ (1970) Calcium transport in mitochondria. *FEBS Letters*

Severs NJ (2007) Freeze-fracture electron microscopy. *Nat Protoc* **2:** 547–576

Shaffer PL, Goehring A, Shankaranarayanan A & Gouaux E (2009) Structure and Mechanism of a Na+-Independent Amino Acid Transporter. *Science* **325:** 1010–1014

Shi L, Quick M, Zhao Y, Weinstein H & Javitch JA (2008) The Mechanism of a Neurotransmitter:Sodium Symporter—Inward Release of Na+ and Substrate Is Triggered by Substrate in a Second Binding Site. *Molecular Cell* **30:** 667–677

Shimamura T, Weyand S, Beckstein O, Rutherford NG, Hadden JM, Sharples D, Sansom MSP, Iwata S, Henderson PJF & Cameron AD (2010) Molecular Basis of Alternating Access Membrane Transport by the Sodium-Hydantoin Transporter Mhp1. *Science* **328:** 470–473

SLATER EC & CLELAND KW (1953) The effect of calcium on the respiratory and phosphorylative activities of heart-muscle sarcosomes. *Biochem. J.* **55:** 566–590

Söding J, Biegert A & Lupas AN (2005) The HHpred interactive server for protein homology detection and structure prediction. *Nucleic Acids Res.* **33:** W244–8

Stock D, Leslie AG & Walker JE (1999) Molecular architecture of the rotary motor in ATP synthase. *Science* **286:** 1700–1705

Tang L, Bai L, Wang W-H & Jiang T (2010) Crystal structure of the carnitine transporter and insights into the antiport mechanism. *Nature Publishing Group* **17:** 492–496

Tate CG (2001) Overexpression of mammalian integral membrane proteins for structural studies. *FEBS Letters* **504:** 94–98

Toyoshima C, Nakasako M, Nomura H & Ogawa H (2000) Crystal structure of the

calcium pump of sarcoplasmic reticulum at 2.6 A resolution. *Nature* **405:** 647–655

Turk E (2000) Molecular Characterization of Vibrio parahaemolyticus vSGLT. A MODEL FOR SODIUM-COUPLED SUGAR COTRANSPORTERS. *Journal of Biological Chemistry* **275:** 25711–25716

Vasington FD & Murphy JV (1961) Vasington: Active binding of calcium by mitochondria - Google Scholar. *Fed Proc*

Vinothkumar KR (2005) Oligomeric Structure of the Carnitine Transporter CaiT from Escherichia coli. *Journal of Biological Chemistry* **281:** 4795–4801

Wang L, Yang X, Li S, Wang Z, Liu Y, Feng J, Zhu Y & Shen Y (2014) Structural and mechanistic insights into MICU1 regulation of mitochondrial calcium uptake. *The EMBO Journal* **33:** 594–604

Wang W, Black SS, Edwards MD, Miller S, Morrison EL, Bartlett W, Dong C, Naismith JH & Booth IR (2008) The structure of an open form of an E. coli mechanosensitive channel at 3.45 A resolution. *Science* **321:** 1179–1183

Watanabe A, Choe S, Chaptal V, Rosenberg JM, Wright EM, Grabe M & Abramson J (2010) The mechanism of sodium and substrate release from the binding pocket of vSGLT. *Nature* **468:** 988–991

Weyand S, Shimamura T, Yajima S, Suzuki S, Mirza O, Krusong K, Carpenter EP, Rutherford NG, Hadden JM, O'Reilly J, Ma P, Saidijam M, Patching SG, Hope RJ, Norbertczak HT, Roach PCJ, Iwata S, Henderson PJF & Cameron AD (2008) Structure and Molecular Mechanism of a Nucleobase-Cation-Symport-1 Family Transporter. *Science* **322:** 709–713

Wong FH, Chen JS, Reddy V, Day JL, Shlykov MA, Wakabayashi ST & Saier MH Jr (2012) The Amino Acid-Polyamine-Organocation Superfamily. *J Mol Microbiol Biotechnol* **22:** 105–113

Wöhlert D, Kühlbrandt W & Yildiz Ö (2013) Structure and substrate ion binding in the sodium/proton antiporter PaNhaP. *Elife* **3:** e03579–e03579

Yamashita A, Singh SK, Kawate T, Jin Y & Gouaux E (2005) Crystal structure of a bacterial homologue of Na+/Cl--dependent neurotransmitter transporters. *Nature* **437:** 215–223

Yildirim MA, Goh K-I, Cusick ME, Barabási A-L & Vidal M (2007) Drug-target network. *Nat. Biotechnol.* **25:** 1119–1126

Zhao Y, Quick M, Shi L, Mehler EL, Weinstein H & Javitch JA (2009) Substrate-dependent proton antiport in neurotransmitter:sodium symporters. *Nature Chemical Biology* **6:** 109–116

Zhao Y, Terry DS, Shi L, Quick M, Weinstein H, Blanchard SC & Javitch JA (2011)

Substrate-modulated gating dynamics in a Na+-coupled neurotransmitter transporter homologue. *Nature* **474:** 109–113

Zhou M, Morais-Cabral JH, Mann S & MacKinnon R (2001) Potassium channel receptor site for the inactivation gate and quaternary amine inhibitors. *Nature* **411:** 657–661

Zhou Y, Bennett ER & Kanner BI (2004) The aqueous accessibility in the external half of transmembrane domain I of the GABA transporter GAT-1 Is modulated by its ligands. *JBC* **279:** 13800–13808

Ziegler C, Bremer E & Krämer R (2010) The BCCT family of carriers: from physiology to crystal structure. *Molecular Microbiology***:** no–no

Ziegler C, Morbach S, Schiller D, Krämer R, Tziatzios C, Schubert D & Kühlbrandt W (2004) Projection structure and oligomeric state of the osmoregulated sodium/glycine betaine symporter BetP of Corynebacterium glutamicum. *Journal of Molecular Biology* **337:** 1137–1147

Zomot E, Bendahan A, Quick M, Zhao Y, Javitch JA & Kanner BI (2007) Mechanism of chloride interaction with neurotransmitter:sodium symporters. *Nature* **449:** 726–730